Integrative and coupled model based on hydrodynamics, biogeochemistry and physiology for the prediction of biomass and biogeochemical dynamics, projections under future oceanic conditions and marine spatial planning

Project acronym:	ATLAS
Grant Agreement:	678760
Deliverable number:	D2.5
Deliverable title:	Integrative and coupled model based on hydrodynamics, biogeochemistry and physiology for the prediction of biomass and biogeochemical dynamics, projections under future oceanic conditions and marine spatial planning
Work Package:	2
Date of completion:	31/10/2019
Author:	Dick van Oevelen, Evert de Froe, Christian Mohn, Karline Soetaert

This project has received funding from the European Union's Horizon 2020 research and innovation programme under grant agreement No 678760 (ATLAS). This output reflects only the author's view and the European Union cannot be held responsible for any use that may be made of the information contained therein.

Contents

1 (illustrated) Executive summary

[1] An important goal of WP2 was to develop mechanistic and predictive models for the distribution and metabolic activity of cold-water corals (CWCs) and deep-water sponges (DWS) and use these models to understand how their distribution is affected by the Atlantic Meridional Overturning Circulation (AMOC).

[2] Output from hydrodynamic models (VIKING20 or ROMS-Agrif) was used to simulate transport of reactive organic matter in the water column around CWC reefs of DWS grounds. The approach is inspired by Soetaert *et al*. (2016), in which suspended organic matter dynamics above coral mounds was simulated. Here, we extend this methodology by having CWCs and DWS feeding on the suspended organic matter in the bottom layer using simple formulations for passive (CWC) and active (DWS) suspension feeding and metabolic activity. Physiological model formulation was based on data collected within ATLAS (Deliverables 2.1 and 2.2).

[3] We focus on three ATLAS Study regions: 1) large CWC mounds, dominated and formed by the scleractinians *Lophelia pertusa* and *Madrepora oculata*, in the Logachev mound province in the south-eastern section of Rockall Bank, 2) coral gardens, dominated by the soft-coral *Viminella flagellum*, on Condor seamount, and 3) extensive sponge grounds, dominated by *Geodia barretti* along the east Canadian shelf break in Davis Strait.

[4] We faced considerable computational challenges when developing the coupled models. CWC and DWS growth is slow, which implies that long simulation periods are needed to reach a (dynamic) steady state. Long simulation periods are not feasible given the high spatial and temporal (i.e. with tidal dynamics) resolution of the models. A 3-step solution procedure is proposed to tackle this issue, in which in step 1 initial suspended organic matter (OM) concentrations in the water column are calculated. In step 2, the bottom layer concentrations from step 1 are used to calculate initial concentrations for CWCs or DWS. In step 3, the coupled model is run with suspended organic matter (step 1) and CWC or DWS (step 2) as starting conditions. This approach sufficed for most of the model applications, but we acknowledge that some regions in the different model domains have not yet reached a (dynamic) steady state.

[5] The coupled models, based on hydrodynamics, organic matter biogeochemistry and physiology of reef-forming organisms, successfully predicted the coral and sponge distribution and biomass in the three case study areas and thereby provide a new mechanistic tool to understand

the distribution (see figure below) and metabolic (not shown) activity of hotspot ecosystems.

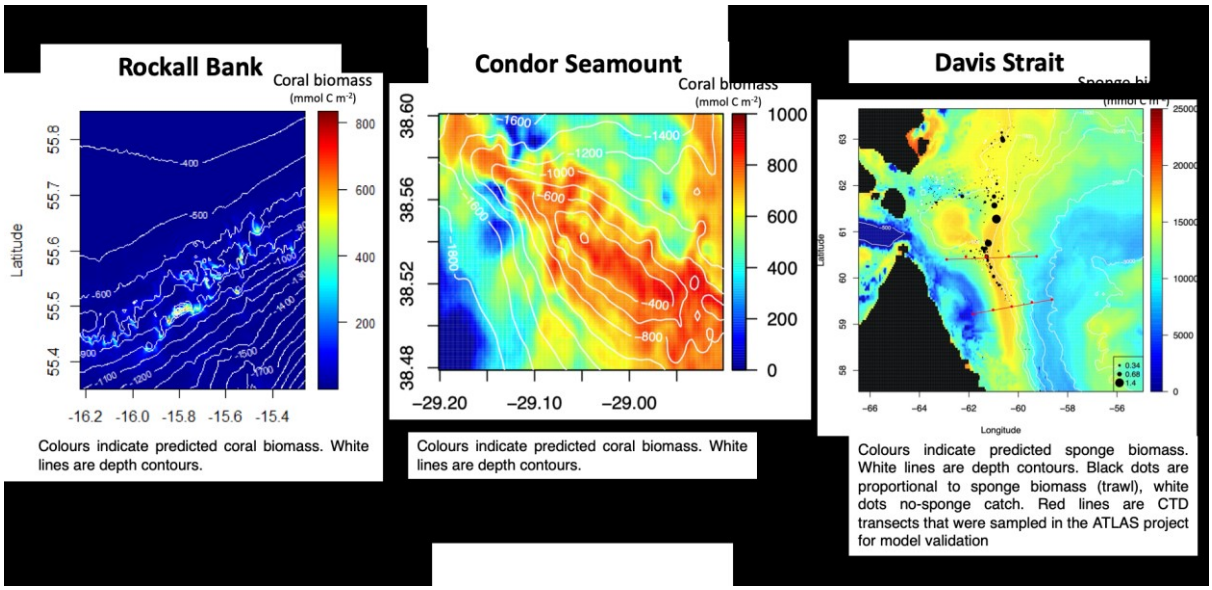

[6] A striking result for Rockall Bank and Condor Seamount was that the suspended organic matter concentration in the bottom layer of the model domain was heavily modified by the passive suspension feeding CWCs. The initial PSF biomass (step 2) immediately depleted the organic matter concentration in the bottom layer to near zero across the whole model domain (see figure of Condor seamount below). As a result, the remaining organic matter concentration was insufficient to meet demands, which invoked a slow but steady reduction in PSF biomass over time. We conclude that the impact of PSF on bottom layer suspended OM concentration extends over large areas of the seafloor, including regions where the natural biomass is low.

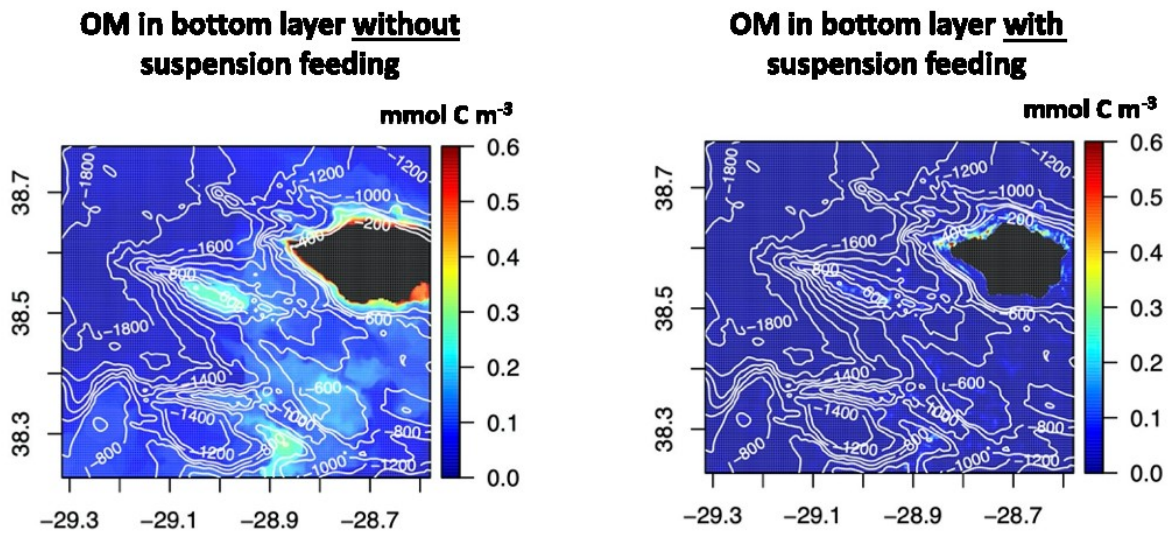

[7] The distribution of CWC at Rockall Bank and Condor seamount could be accurately modelled with suspended organic matter being parameterized as labile, fast-sinking organic matter, e.g. labile marine snow and zooplankton faecal pellets. The relatively fast sinking rate of this organic matter, gives a relatively low concentration in the water column, but the high current velocities around coral mounds ensure sufficient interception by the passive suspension feeding CWCs.

[8] In contrast, the concentration of labile, fast-sinking organic matter OM proved grossly insufficient to meet the carbon demands of the active suspension feeding DWS. Only when we parameterized the suspended organic matter as slow sinking, relatively refractory organic matter the ambient concentration was sufficient to allow growth of DWS. This organic matter is likely characterised by smaller particles (microbial and [colloidal] DOM). The modelled DWS distribution matched field observations substantially better with slow-sinking organic matter as opposed to predictions based on fast-sinking organic matter. Experimental work (Deliverable 2.2) already hinted at these different feeding preferences between active and passive suspension feeders. We hypothesize that CWC (i.e. passive suspension feeders) and DWS (i.e. active suspension feeders) distribution on shelf breaks and slopes can be explained by a niche separation based on organic-matter type.

[9] Model simulations for different AMOC states were run for each of the three case study areas. We cannot conclude from the results to what extent AMOC influences the biomass of CWC and DWS. As mentioned in [4], it proved challenging to reach a (dynamic) steady state for the models. As a result, it remained unclear whether the small differences in hydrodynamics between AMOC states truly governed differences in biomass development. In addition, tidal dynamics proved important for the transport of organic matter to the CWCs and the tidal forcing is not influenced by AMOC. We do however believe that the models are well suited for the exploration of mechanistic relations between distributions of CWCs and DWS and for example reductions in export of organic matter or changes in the type of exported organic matter.

2 Introduction

Deep-water reef-forming ecosystems contribute substantially to biogeochemical cycling on continental shelves and slopes, as a substantial fraction of the surface production is mediated by deep-water sponge and coral grounds (Cathalot *et al*. 2015; de Froe *et al*. 2019, see also Deliverable 2.3). Our current capacity to predict the biomass of reef-forming organisms that form hotspots on the seafloor is presently limited to statistical approaches, including habitat suitability models (Davies & Guinotte 2011; Knudby *et al*. 2013; Rengstorf *et al*. 2014; Tittensor *et al*. 2010; Yesson *et al*. 2012). While these models are successful in predicting the distribution of cold-water corals and sponge grounds, the lack of an underlying mechanistic description renders these models less suitable for understanding distribution patterns, carbon and nutrient budget modelling and understanding how their distribution may be altered by changes in food supply and climate. In Deliverable 2.5 we develop a new mechanistic modelling approach to predict the distribution, biomass and biogeochemical activity of deep-water sponges and CWCs.

Food supply and hydrodynamics are two well-known variables from literature that explain the distribution of deep-water sponges and CWCs (Duineveld *et al*. 2007; Guinotte *et al*. 2006; Mienis *et al*. 2007; Mohn *et al*. 2014; Soetaert *et al*. 2016). In work package 1, Dierk Hebbeln confirmed from a geological analysis of cold-water coral mound growth and demise, that two factors consistently play a key role: 1) surface productivity and/or food supply and 2) vigorous hydrodynamic forcing. Hence, these factors were taken as a starting point for the mechanistic modelling approach. In this deliverable, we describe how hydrodynamic forcing obtained from models (VIKING20 or ROMS-Agrif) and validated by observations (Deliverable 2.3 and 2.4) determines the organic matter concentration in the water column (Soetaert *et al*. 2016) and how this can be used to predict the distribution and biomass of CWCs and deep-water sponges in the three case study areas: Rockall Bank, Condor Seamount and Davis Strait.

Apart from our goal to develop a mechanistic understanding of the growth of reef-forming organisms, we aim to use these models to address how changes in the Atlantic Meridional Overturning Circulation (AMOC) may affect the distribution and biomass of CWCs (CWCs) and deep-water sponges (DWS). The relevant time scale for AMOC changes to affect CWCs and DWS is likely in the decades to centuries. This timescale is particularly difficult to address, as the resolved time steps from paleo reconstructions are too large, while time series from *in*

situ observations are not existing or are too short. Hence, a modelling approach may be suited to tackle this intermediate time scale. To devise a sensible approach to tackle this question, a workshop with several ATLAS participants from work packages 1-4 was organised at Edinburgh University in January 2018. In short, it was decided that we would run the mechanistic models with hydrodynamic forcing for a period of a weak and a strong AMOC state and these periods were identified as 1979 (weak AMOC) and 1993 (strong AMOC; see Deliverable 2.4).

Below we describe the general approach that was taken in this Deliverable, but the approach was tailored to each study area as we detail below.

3 General approach

This Deliverable focusses on three cases study areas: 1) Rockall Bank, 2) Condor Seamount and 3) Davis Strait, which are respectively Case Study areas 3, 8 and 10 in the ATLAS project. The Logachev Mound province in the south-eastern region of the case study area Rockall Bank, approximately 400 km west of Ireland, hosts many smaller and larger coral mounds that are largely formed by the scleractinian CWCs (CWCs) *Lophelia pertusa* and *Madrepora oculata*. Condor seamount lies to the west of the Island Faial (Azores) and is known to host extensive coral gardens on the summit that are dominated by *Viminella flagellum*. Finally, the case study area Davis Strait lies in the western Atlantic on the Canadian continental shelf between Greenland and Canada of which the shelf edge and slope hosts extensive deep-water sponge (DWS) grounds.

Periods of contrasting AMOC states were identified from a 53-year hindcast VIKING20 model (see also Deliverable 2.4). The VIKING20 model has been developed by GEOMAR in Kiel, Germany, in the EU-FP7 project THOR (2007-2013, grant no 212643) (Böning *et al*. 2016). The VIKING20 model is a nest of the polar and sub-polar North Atlantic embedded in the global ocean general circulation model ORCA025 (1/4° resolution). The VIKING20 model is eddy-resolving with a spatial resolution of 1/20° with prescribed atmosphere covering the North Atlantic in the latitudinal range 30 °N - 80 °N. The model output includes a large set of prognostic and diagnostic 2D and 3D variables, including temperature, salinity, sea surface height, mixed layer depth, 3D currents, and atmosphere and ocean fluxes. All model output parameters are made available as 5-day averages, i.e. 73 records per parameter and year. VIKING20 data were extracted for the three ATLAS case study areas and showed a period of

weak AMOC state at the end of the 1970s and a strong AMOC state in the middles of the 1990s (Figure 1). Subsequent analysis in Deliverable 2.4 showed that these AMOC states correspond to slightly reduced water-column and bottom velocities in the weak AMOC state as opposed to the strong AMOC state for all three case studies. Hence, on the premise that if variation in the AMOC state on a decadal time scale influences CWC and DWS ecosystems, we chose these 'end member' states to investigate the influence on reef-forming ecosystems.

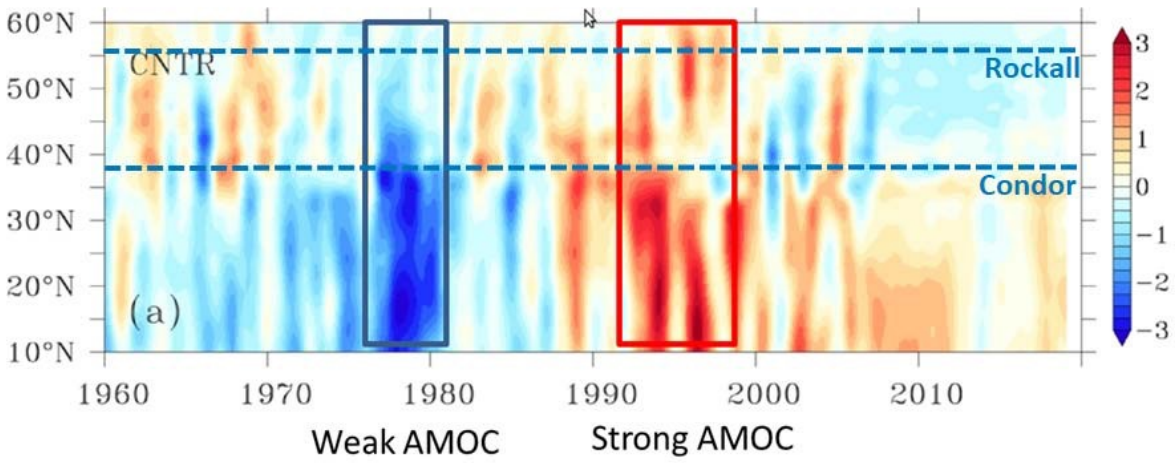

Figure 1: VIKING20 basin wide AMOC anomalies. This figure was reproduced from Böning *et al* (2016) from their supplementary information (Figure 4c). Examples for periods/years of low (weak) AMOC state: 1978- 1981 across a range of subpolar/subtropical latitudes.

For the case study areas Rockall Bank and Condor Seamount, high resolution ROMS-Agrif models (250x250 m spatial resolution and 3-hour temporal resolution) were developed with the VIKING20 and OSU inverse tidal forcing as boundary condition (Deliverable 2.4). As model runs proved to be very long and produce large output files, we decided to focus the comparison March and July in 1979 versus March and July 1993, in which the March vs. July comparison allows estimating effects of seasonality (including e.g. stratification) and the 1979 vs. 1993 for contrasting AMOC states. The hydrodynamic exchanges in the water column at both case studies were used to drive suspended organic matter transport at each case study (*sensu* Soetaert *et al*. 2016 and see below).

A different approach was taken for the case study area Davis Strait. The spatial scale over which the biomass of DWS varies at Davis Strait is several 100s of kms and thereby much larger than the spatial scale over which CWC biomass varies at Rockall Bank and Condor seamount (±10s of km scale). The large spatial scale made it not feasible to develop a high-resolution ROMS-Agrif model for Davis Strait. Instead the VIKING20 model output was

averaged on a rectangular model grid (see details below) and subsequently used for modeling suspended organic matter transport. For this case study, we used the VIKING20 output from 1979 and 1993 as contrasting AMOC states.

Growth of CWCs and DWS is very slow and therefore it appeared that the model initialization and time to reach a dynamic equilibrium was very time consuming. To make this process manageable we took a three-step approach that was comparable between cases studies but was tailored to each case study (see details below). The three steps we designed are as follows. In step 1, we calculated appropriate initial conditions for the suspended organic matter concentration. The organic matter concentration was first initialized by a simple exponential decay function (i.e. assuming no hydrodynamic transport) and was then run with the hydrodynamic forcing for several loops of the respective period (e.g. 3 subsequent runs with hydrodynamic forcing of March 1979). The final suspended organic matter concentration of these subsequent loops was stored as initial condition for the suspended organic matter for the final coupled model (see step 3). In step 2, we calculated appropriate initial conditions for the biomass of CWCs or DWS and sediment organic matter throughout the model domain. For this, the suspended organic matter concentration (output of step 1) in the bottom layer was used to calculate the equilibrium biomass and sediment organic matter concentration. In step 3, we ran the final coupled model by taking the initial suspended organic matter concentration (step 1), initial biomass of CWCs or DWS (step 2) and sediment organic matter concentration (step 2) and running several consecutive loops of the respective period (e.g. March 1979) to arrive at a (dynamic) equilibrium state of the organic matter concentration in the water column, biomass of CWCs or DWS and sediment organic matter.

4 Rockall Bank

4.1 Site description

4.1.1 Bathymetry

Rockall bank is a large shallow bank in the North-East Atlantic Ocean, approximately 500 km north-west of Ireland (N 55.55, W 15.80; Figure 1A). On the south-eastern flank of the Rockall Bank, numerous coral-capped mounds and ridges can be found between 500 – 1000 m depth (Kenyon *et al*. 2003; Mienis *et al*. 2006; Soetaert *et al*. 2016). Our study area consists of a 60 x 90 km area located on the SE flank of the Rockall Bank (Figure 2A-B), with a depth between 320 and 2500 metres. In the north-eastern part of the study area, coral ridges are found

between 400 – 500-metre depth. The Logachev mound province, containing several large coral mounds, is in the southwestern part of the model domain. The largest and most characteristic coral mound in the area is the Haas mound. This mound is 5 km wide, 2 km long and its depth ranges from 900 metre (base) to 550 metre (summit). South west of the Haas mound, two smaller mounds occur, of which one is the Oreo mound. At this mound, a mooring was placed between April 2017 – May 2018 (Deliverable 2.4). We divided the model domain into four regions: shallow sediment, coral mound, off-mound, and deep sediment (Figure 3). “Shallow sediment” is the area located on the Rockall Bank that is shallower than 500 meters, “deep sediment” is the area deeper than 1500 meters, “coral” is the coral region predicted by a coral habitat suitability model (Rengstorf *et al*., 2014), “off-mound” is the area between the coral mounds.

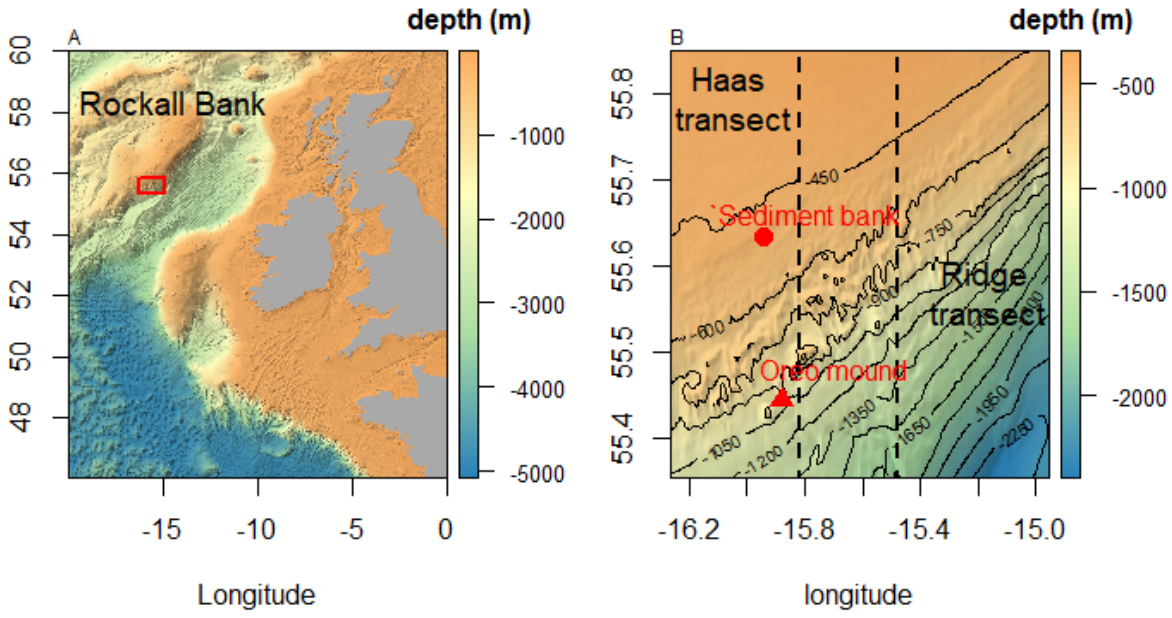

Figure 2: A) Location of the Rockall bank and the model domain. B) bathymetry of the model domain, with the two transect lines (Haas transect and Ridge transect) and two lander locations (Oreo mound and Sediment bank).

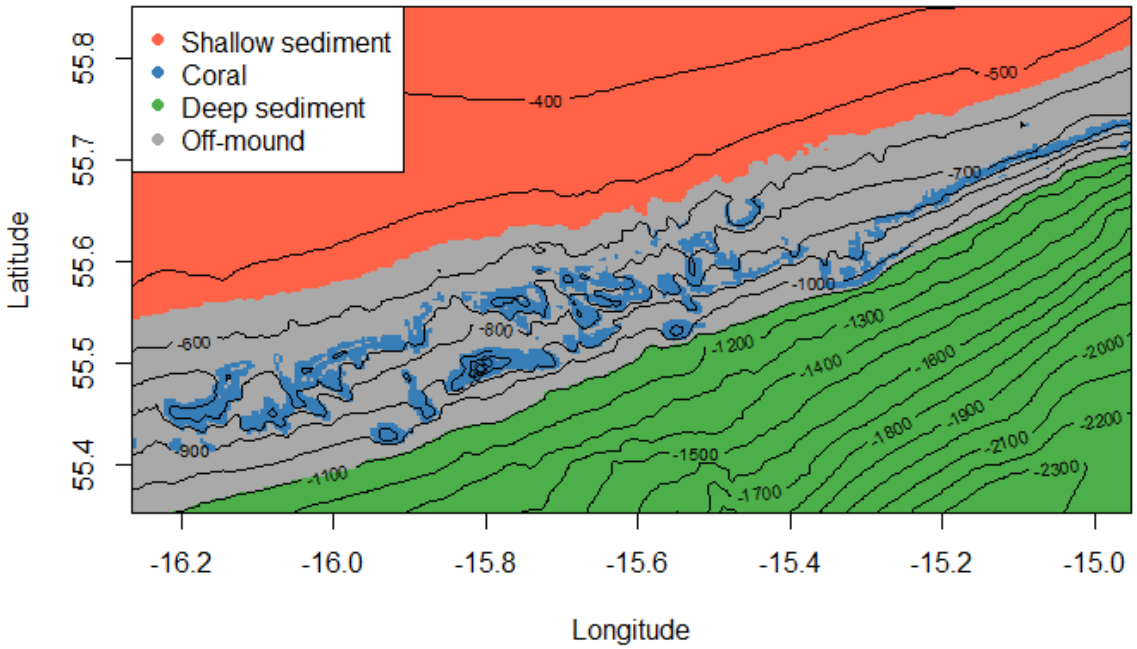

Figure 3: Rockall Bank model domain divided in four regions.

4.1.2 Hydrography

The Rockall trough is the basin between the Rockall Bank and the Irish continental shelf and is considered an exchange pathway for water coming from the Eastern North Atlantic and the Nordic seas. From the south, Eastern North Atlantic Water enters Rockall trough at the surface layer with the North Atlantic Current (NAC). At around 700-metre water depth, North Atlantic Water is transported northwards along the eastern slope of the trough and between 1600- and 1900-meters Labrador Sea Water enters the Rockall trough basin and recirculates in an anticyclonic fashion in the southern part of the basin (see Deliverable 2.4). In the north, Wyville Thomson Ridge Overflow Water (WTOV) enters the basin at intermediate depth (500 – 1000 meters) and flows in SE direction (Johnson *et al*. 2010, Deliverable 2.3). On the south-eastern flank of the Rockall Bank, hydrodynamic features as internal tidal waves and hydraulic jumps are known to occur (Cyr *et al*. 2016; Mohn *et al*. 2014).

4.1.3 Biology

The carbonate mounds and ridges along the SE slope of the Rockall Bank (Figure 2B) contain thriving coral reefs consisting of the framework building CWC *Lophelia pertusa* and *Madrepora oculata* with associated macrofauna such as polychaetes (e.g. *Eunice norvegica*),

sponges (e.g. *Hexadella dedritifera*), and crinoids (Van Soest & Lavaleye 2005; van Weering *et al*. 2003). On the summit of the Haas mound, a patchy distribution of living corals alternating with bare sediments and coral rubble was observed. On the southern flank of the Haas mound and Oreo mound a dense cold-water coral reef (van Bleijswijk *et al*. 2015) was observed. The southern flank of the Haas mound contained up to 30 times more dead coral framework than the summit (Mienis *et al*. 2009). Benthic metabolic activity, measured as community oxygen consumption, was between two and twenty times higher on Oreo and Haas mound as compared to bare sediments on the Rockall Bank. In addition, the sediment underneath the cold-water coral framework had a finer composition and contained more organic matter than Rockall Bank sediment (see Deliverable 2.3, de Froe *et al*. 2019).

4.2 Coupled model development

4.2.1 Hydrodynamic model

A detailed description of the ROMS-Agrif hydrodynamical model can be found in deliverable 2.4. The model domain comprises of a three-dimensional grid, containing 329 x 221 x 29 grid cells, resembling 83 km in longitude and 56 km in latitude and the water depth ranges from 337 to 2417 metre (Figure 2B). The model is built as a sigma grid (Shchepetkin and McWilliams, 2005), in which the water column is divided into 32 sigma layers. Two latitudinal sections of the model, one over Haas mound and one over a coral ridge, are shown in Figure 4. For each cell the model calculated the zonal (*u*), meridional (*v*), and vertical velocities (w), along with salinity and the water temperature.

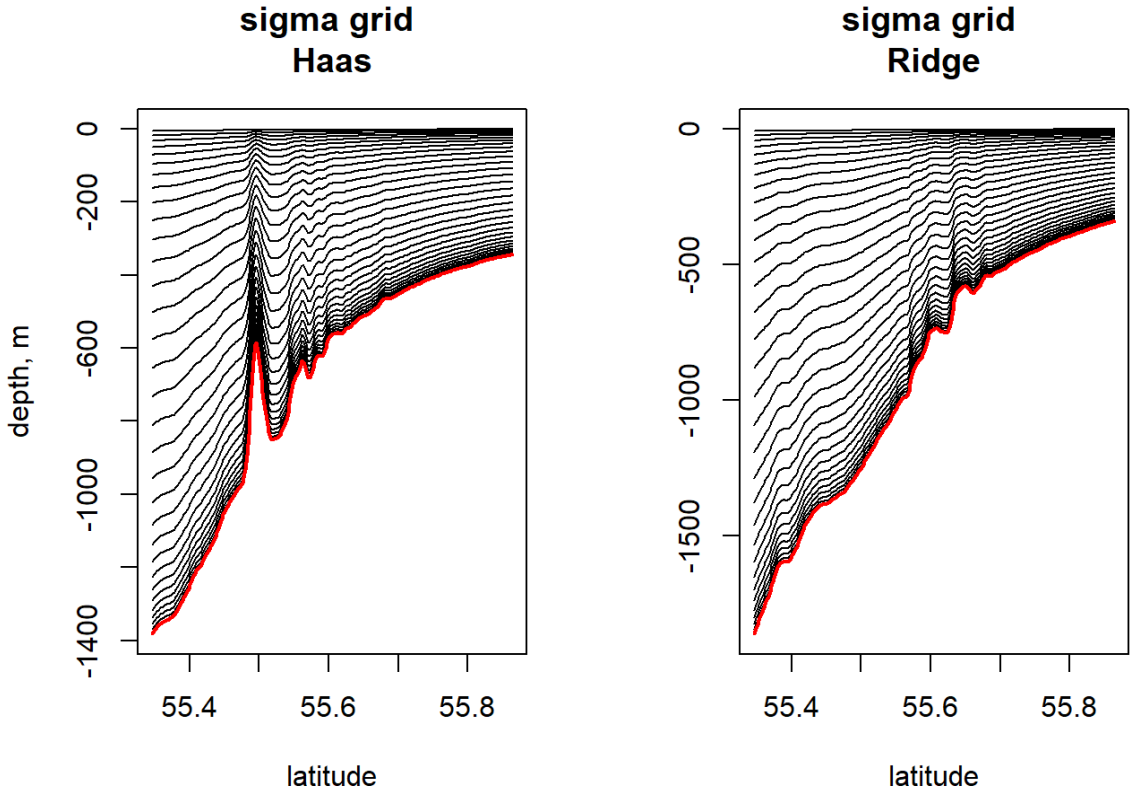

Figure 4: Latitudinal sections of the sigma grid over Haas mound and a coral ridge.

4.2.2 OM suspended matter

The output of the hydrodynamical model is used as input for the three dimensional biogeochemical particulate organic matter (POM) transport model. Soetaert *et al*. (2016) shows a simple reactive transport formulation for suspended POM (mmol C m^{-3}):

$$\frac{dH_zC}{dt} = -\frac{d(H_zuC)}{dx} - \frac{d(H_zvC)}{dy} - \frac{d(H_zwC)}{dz} - \frac{d(H_zw_sC)}{dz} - kH_zC$$

where C is the concentration POM in mmol C m^{-3}, H_z is the grid cell thickness (m), w_s is the passive sinking velocity (m d^{-1}) and k is the first-order decay rate (d^{-1}).

The study of Henson *et al*. (2015) provides a model analysis of the carbon export and export efficiency in the ocean. In this study, the annual primary production and export efficiency for the Rockall Bank area corresponds to 200 g C m^{-2} and 25 % respectively, which gives an annual export production of 50 g C m^{-2} yr^{-1}, or 12 mmol C m^{-2} d^{-1}. This value is similar to the export production used in the modelling study by Soetaert *et al*. (2016).

The degradation rate of sinking POM is based on the formulation used in the MEDUSA20 model framework, which is defined as $k = 0.016 \times 1.066^{T}$ (Henson *et al*., 2015; Yool *et al*., 2011), in which T is temperature in °C. Temperature ranges from 4 °C at 2000-metre depth, to 15 °C in the summer periods at the surface layer. We used an intermediate temperature of 10°C to calculate the degradation rate, which gives a *k* of 0.03 d^{-1}.

Previous work showed that POM sinking velocity is characterized by a large range of 2 to 820 m d^{-1} (McDonnell & Buesseler 2010; Trull *et al*. 2008) and can be divided into three categories: slow sinking, fast sinking and suspended particles (Riley *et al*. 2012). In this model, we set the sinking velocity to 10 m d^{-1}, which we consider as relatively labile fast sinking fraction of POM.

4.2.3 Seafloor activity

At the bottom boundary of the three-dimensional biogeochemical model a two-dimensional benthic biomass model is imposed, containing two state variables: passive suspension feeder biomass (PSF_b) and organic matter content of the sediment (OM_{sed}), which are both expressed in mmol C m^{-2}. The passive suspension feeder biomass is regulated by the following equation:

$$\frac{dPSF}{dt} = UE_{\mathrm{PSF}} \cdot AE_{PSF} \cdot NGE_{PSF} \cdot A_{PSF} \cdot v_{bbl} \cdot OM_{bbl} \cdot \left(1 - \frac{{v_{bbl}}^{p}}{{v_{bbl}}^{p} + {k_v}^{p}}\right) \cdot PSF \cdot \left(1 - \frac{PSF}{CC_{PSF}}\right) - m_{PSF} \cdot PSF$$

in which UE_{PSF} is the uptake efficiency of a *L. pertusa* colony (-), AE_{psf} is the assimilation efficiency (-), NGE_{PSF} is the net-growth efficiency (-), A_{PSF} is the surface to biomass ratio for *L. pertusa* given in m^2 mmol C^{-1}, v_{bbl} is the current speed of the benthic boundary layer (in m s^{-1}), FP_{max} is the maximum fraction of open polyps for a colony (-), k_v is the current speed at which a colony has half of its polyps expanded (m s^{-1}), *p* is a fitting parameter for the fraction of expanded polyps per colony (-), OM_{bbl} is the organic matter concentration in the benthic boundary layer (mmol C m^{-3}), CC_{PSF} is the carrying capacity of passive suspension feeders (mmol C m^{-2}), m_{PSF} is the basal respiration of *L. pertusa* (d^{-1}).

Passive suspension feeders use their polyps and tentacles to feed on particles in the benthic boundary layer. The concentration of food particles is expressed in mmol C m^{-3}, current speed is expressed in m s^{-1} and CWC biomass in mmol C m^{-2}. To calculate the maximum rate a CWC can capture food particles from the water column, we used a surface-to-biomass parameter

expressed in m^2 mmol C^{-1}. For this parameter, we used the literature database collected in D2.1. The study of Gori *et al*. (2014) reported dry weight (g), surface area (cm^2) and number of polyps (-) of fifteen *Lophelia pertusa* branches used in experiments. The % of organic carbon in *Lophelia pertusa* was ~1.3% (Larsson *et al*. 2013; Maier *et al*. 2019). From these values, we estimate *L. pertusa* to have 2.12 ± 0.9 polyps mmol C^{-1}. Coral polyps have an estimated diameter of 35.3 ± 2.0 mm^2 $polyp^{-1}$ (Purser *et al*. 2010), and therefore a feeding surface to biomass conversion factor of $7.48x10^{-5}$ m^2 mmol C^{-1}. However, only a fraction of the polyps in a colony actually captures food particles. Experimental work on the capturing efficiency in passive suspension feeders, such as octocorals, showed values as low as 0.15 feeding polyps $(\text{available polyps})^{-1}$ and the UE_{psf} is therefore set to 0.15 (Hunter 1989).

The assimilated food uptake is the amount of captured food particles times the assimilation efficiency. Direct measurements of the assimilation efficiency for CWCs are not available as experimental measurements are often difficult because the non-assimilated part of the food is often mixed with particulate mucus (Wild *et al*. 2008). However, the relative release of particulate organic matter (i.e. non-assimilated matter and mucus) is comparatively small (Maier *et al*. 2019) and the AE_{PSF} is therefore set at 0.8, consistent with values reported for tropical corals (Anthony 1999).

The ingested food particles are used for growth of the organism, but also to maintain its metabolism. The fraction of carbon incorporated into the tissue compared to the assimilated carbon is known as the net growth efficiency (*NGE*). Although data on NGE for CWCs is scarce, two studies estimate the *NGE* for *L. pertusa* to be between 0.05 and 0.3 (Maier *et al*. 2019; van Oevelen *et al*. 2016). Therefore, the NGE_{PSF} is set to 0.1, which is a relatively low number compared to NGEs reported for zooplankton (>0.5) and shallow-water anemones (0.3 – 0.6) (Anderson *et al*. 2005; Zamer 1986). However, low *NGE*s and slow growth are typical for a long-lived species as *L. pertusa* (Roberts *et al*. 2009).

Flow speed has an effect on polyp behaviour of passive suspension feeders. At high flow speed, suspension feeders retract their polyps to reduce the drag on their tissue. A flow experiment on polyp behaviour and flow speeds in *L. pertusa* showed that for a velocity of 0.4 m s^{-1}, 50% of the polyps are retracted (Orejas *et al*. 2016). This phenomenon is integrated in the benthic model with the following equation: $FP_{max} \cdot \left(1 - \frac{{v_{\mathrm{bbl}}}^p}{{v_{\mathrm{bbl}}}^p + {k_v}^p}\right)$, and fitted to the data of Orejas *et al*. (2016) (Figure 5).

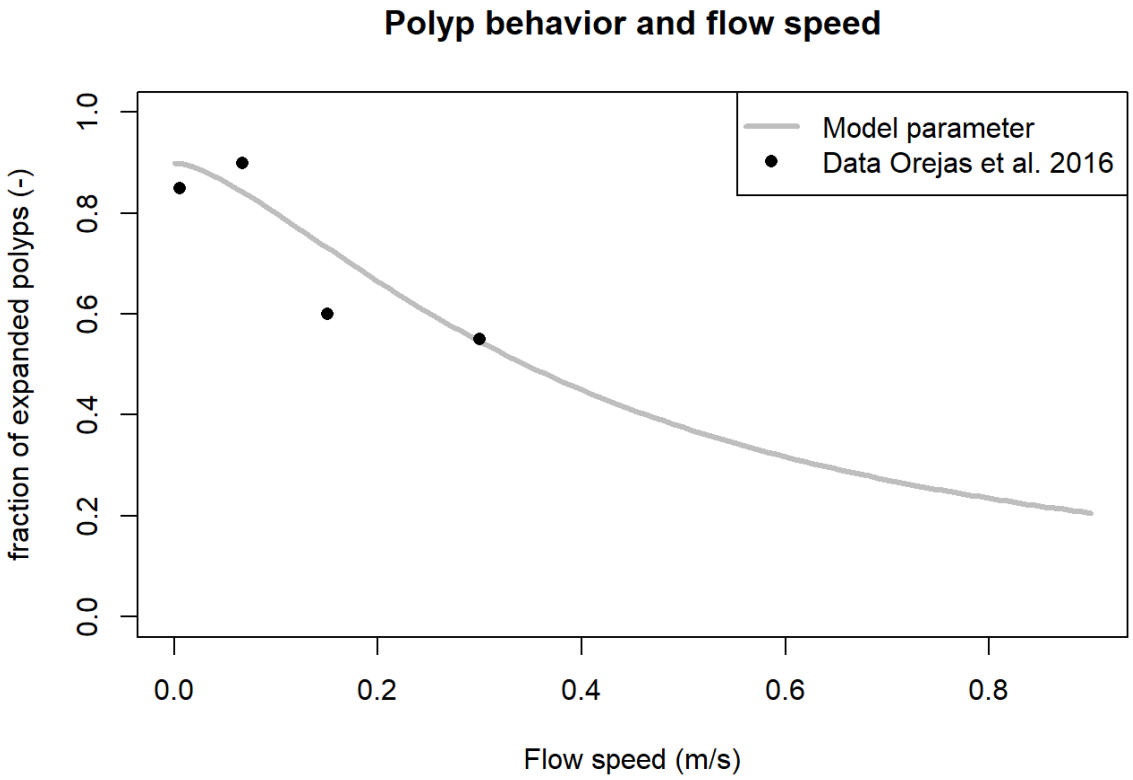

Figure 5: Fitted effect of flow speed on polyp behaviour in a *Lophelia pertusa* colony.

The maximum population size of CWCs is restricted by the carrying capacity. During a sampling campaign to Rockall bank in 2017, the maximum biomass encountered in a boxcore was 1800 mmol C m^{-2} (de Froe *et al*. 2019). The coral colony covered ~20% of the surface area in the boxcore. In a qualitative video analysis done on ROV images from Haas mound, Rockall bank, CWCs covered a maximum of 60% of the seafloor (S. Maier & F. Mienis, unpub. data). Based on these data, we set the carrying capacity of CWCs to 6,000 mmol C m^{-2}.

The basal respiration of CWCs is retrieved from Larsson *et al*. (2013), who performed a long-term starvation experiment on *L. pertusa*. In this study, they starved *L. pertusa* fragments for 28 weeks, and measured the oxygen consumption rate. We took the respiration rate measured at week 28 as the basal respiration rate (0.0035 d^{-1}).

The organic matter in the sediment follows the equation:

$$\frac{dOM_{sed}}{dt} = w_s \cdot OM_{sus} + (1 - AE_{PSF}) \cdot PSFingestion - k_{sed} \cdot OM_{sed}$$

In which $PSFingestion$ is the ingestion of organic matter by passive suspension feeders (mmol C m^{-2} d^{-1}, see equation above), k_{sed} is the sedimentary organic matter respiration (d^{-1}), OM_{sed} is the organic matter concentration of the sediment (mmol C m^{-2}).

4.3 Three-step solution to solve the coupled model

The biogeochemical POM transport model was numerically solved on a staggered Arakawa C-grid, with POM concentration in the centre of each box and the flows on the grid cell interfaces. The flow velocity data from the hydrodynamic model were linearly interpolated in time to obtain flow velocities at every model integration step. The model was numerically integrated using a variable-order Adams-Moulton predictor-corrector scheme, as implemented in the R-package deSolve (Soetaert & Petzoldt 2010) running in the open-source software R (R Development Core Team 2015). Advection was implemented using simple first-order upwind differencing; due to the numerical dispersion that this generates, no horizontal or vertical dispersion was used. In step 1, the initial particulate organic matter concentration in the model is determined by exponential decrease in concentration with water depth and is governed by an exponential equation. The organic matter transport model is subsequently run for three loops (equivalent to three months), and the bottom layer POM concentration of the last loop is used as input for initialising benthic biomass. In step 2, we initialized the cold-water coral biomass and organic matter concentration in the sediment, based on the equations for *PSF* and *OMsed* and the bottom velocity and bottom POM concentration from Step 1. The output of step 1 and step 2 was used as the starting point for the fully coupled model, in which POM in the bottom layer can be taken up by the coral biomass. Coupling the benthic model with the POM transport model made clear that step 2 overestimated the initial benthic biomass. As CWCs are slow growing organisms, it takes considerable time to reach a (dynamic) biomass equilibrium in the coupled model. To speed up computation, we first divided the coral biomass from Step 2 by three and used that as initial benthic biomass. Also, we ran the coupled model for a total of seven consecutive runs (equivalent to seven months), in which the coral growth/decline was artificially increased by a factor of 12, to speed up coral biomass dynamics. The last two runs were done without the growth/decline enhancement factor.

4.4 Results and Discussion

We first explore the hydrographical differences between the two seasons (March vs July) and AMOC states (1979 vs 1993). Note that an additional analysis can be found in Deliverable 2.4. Then, we describe the results of the three modelling steps and the suspended particulate

organic matter, coral biomass, sediment organic matter content and the benthic respiration from the coupled model.

4.4.1 AMOC differences on hydrography

The averaged sea surface temperature showed clear higher temperatures in summer than in spring. Sea surface temperature ranged from 8.8 to 9.2 °C in March and was slightly higher in 1979 than in 1993 (Figure 6A-D). In summer, surface temperature ranged from 12.5 to 14.5 °C and was also slightly warmer in July 1979 than in July 1993. Interestingly, average surface temperature was lower in the Logachev mound province than the surrounding area, indicating upwelling of colder water in this area (Figure 6C-D). The bottom temperature shows a different pattern than surface temperatures, and the four modelled periods align quite well. The deeper parts of the model domain are characterized by cold water (<4 °C), while on the bank bottom temperatures are around 8 °C. In high AMOC year, bottom temperatures on the shallow part of the Rockall bank are warmer and the deeper part (>1500-metre depth) were colder in March (Figure 7A). In the summer month, bottom water temperature is colder over almost the whole model domain in high AMOC compared to low AMOC (Figure 7B). Monthly averaged surface salinities ranged from 35.2 to 35.4 PSU and showed little difference between the four periods. Surface salinity was slightly higher in March compared to July, and only in July 1993 a distinct salinity difference between bank and deeper water was observed (Figure 8A-D).

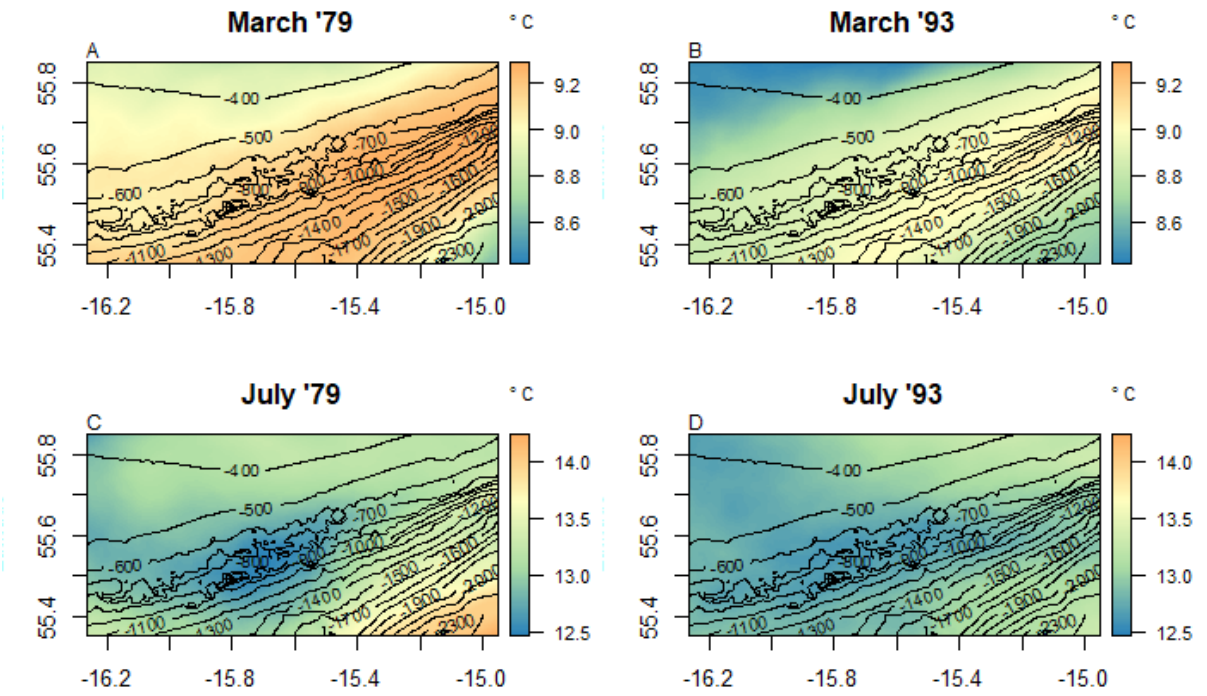

Figure 6: ROMS derived monthly averaged surface temperature of A) March 1979, B) March 1993, C) July 1979, D) July 1993. Note the different scales for March and July.

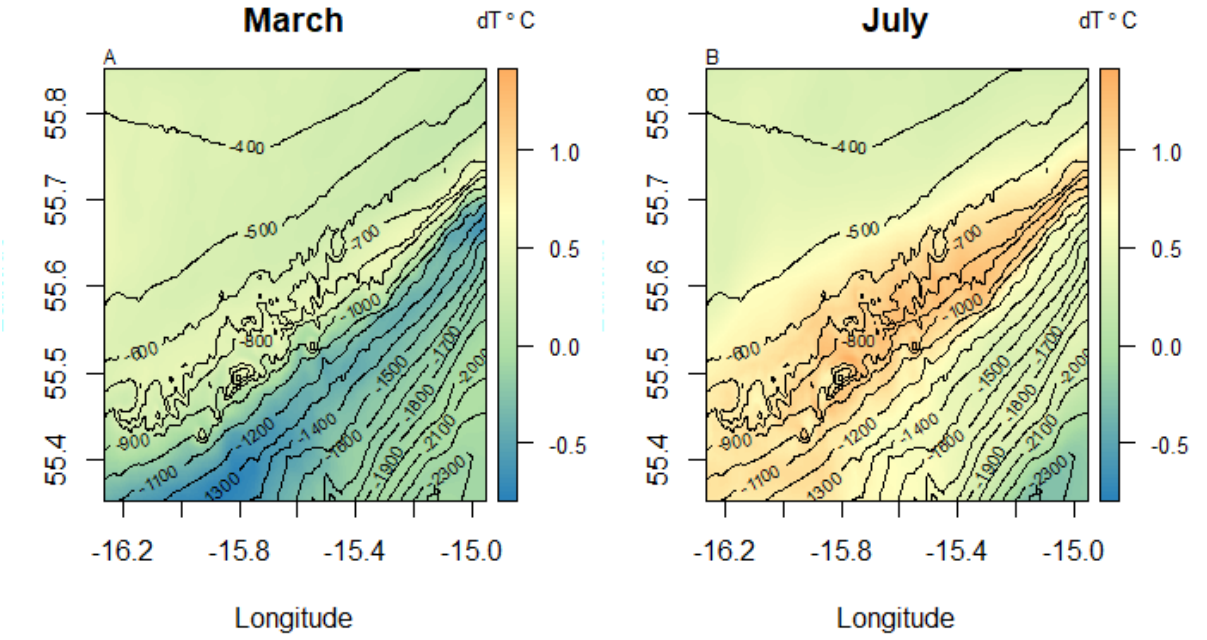

Figure 7: Difference in ROMS derived averaged bottom temperature between A) March 1979 – March 1993, B) July 1979 – July 1993.

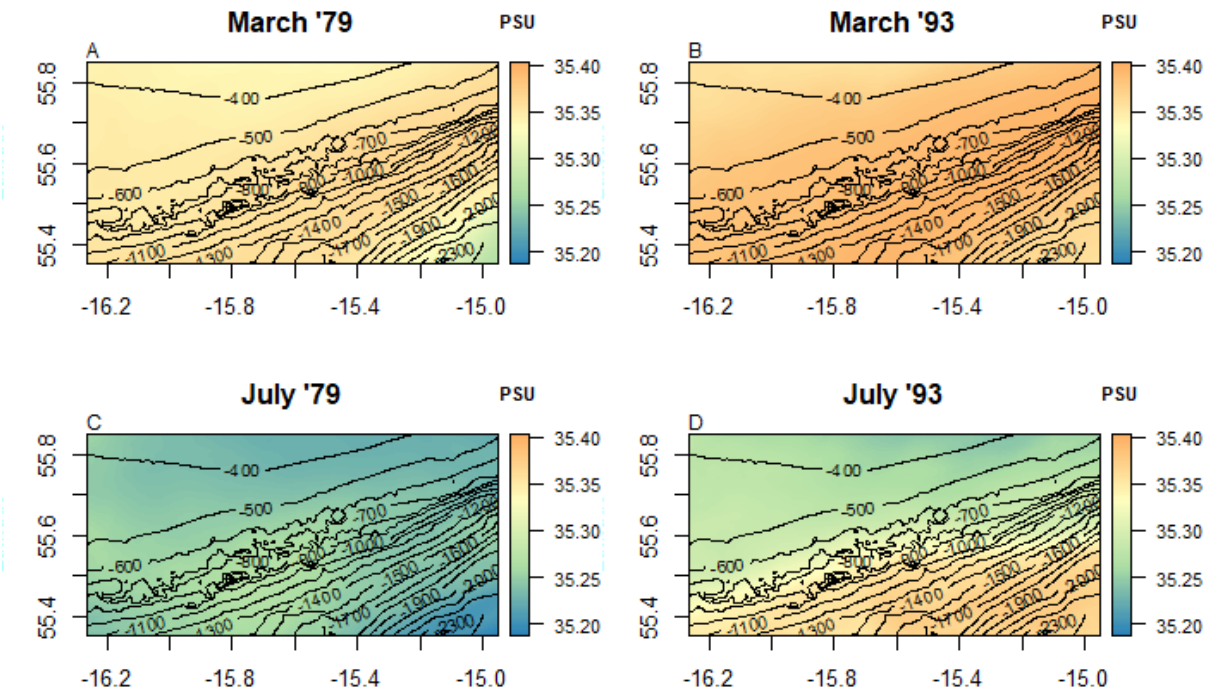

Figure 8: ROMS derived surface salinity (PSU) averaged for each month (A-D). Black lines indicate contours.

The monthly averaged flow velocities ranged from 0.0002 to 0.73 m s^{-1} and displayed a clear pattern for the periods March 1979, March 1993, and July 1993 (Figure 9). Surface water above the deeper parts of the model (>1500 m) showed a strong SW current, while water on the shallow Rockall bank was more stagnant with a low average flow velocity (Figure 9A-C). This pattern was absent in July 1993, where monthly averaged surface flow velocities were much lower and had reversed flow direction (Figure 9D). The depth averaged flow is in the SW direction for all periods, where water is entering the model domain in the NE corner, flowing across the flank of the Rockall Bank and leaving the model domain in the SW corner (Figure 10A-D). The depth averaged flow is higher in March 1993 compared to the other periods. Vertical velocities at approximately 100-metre depth were higher in March 1993 than the other periods, and concentrated around the coral mound area (Figure 11 & Figure 12). The bottom vertical velocities are, for all modelled periods, highest in the coral mound area but also here March 1993 showed increased current velocities compared to the other periods (Figure 13).

A time series of the vertical velocity at the sediment bank mooring (Figure 14) and the Oreo mound (Figure 15) show a clear tidal signal. Vertical velocities are much higher at Oreo mound and there is slightly more downward transport in the high AMOC year, especially in July at the Oreo mound (Figure 15D). Note the different y-axis scale between Figure 14 and Figure 15.

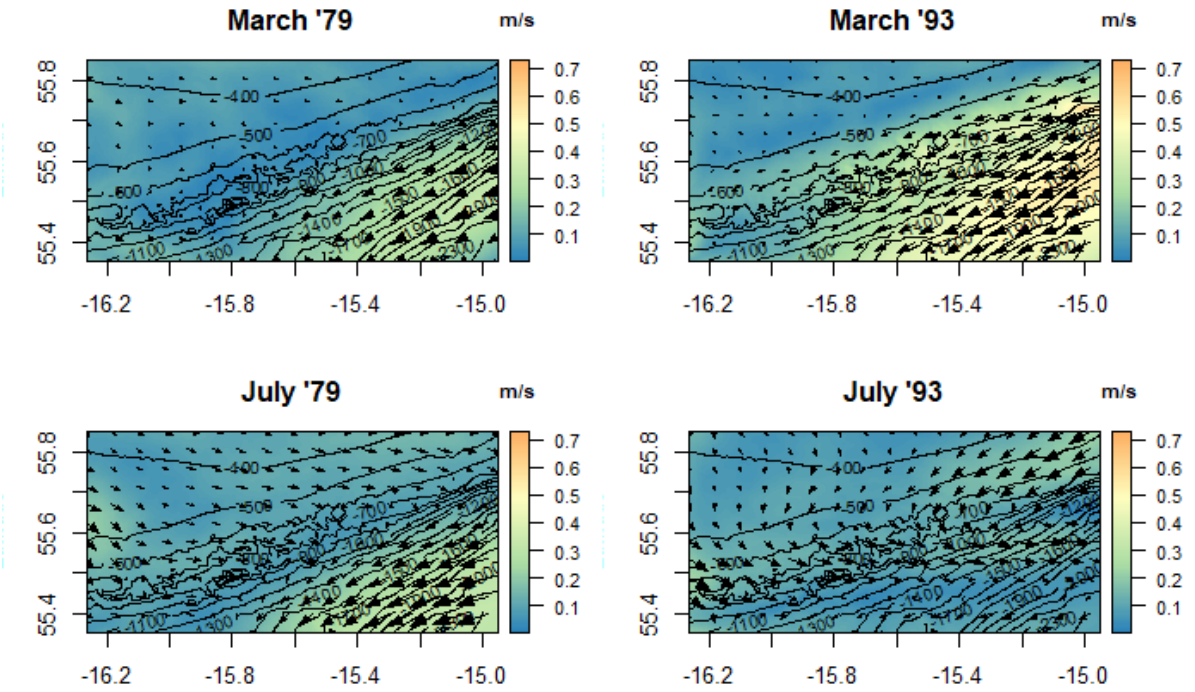

Figure 9: ROMS derived monthly averaged surface flow velocities for the four periods.

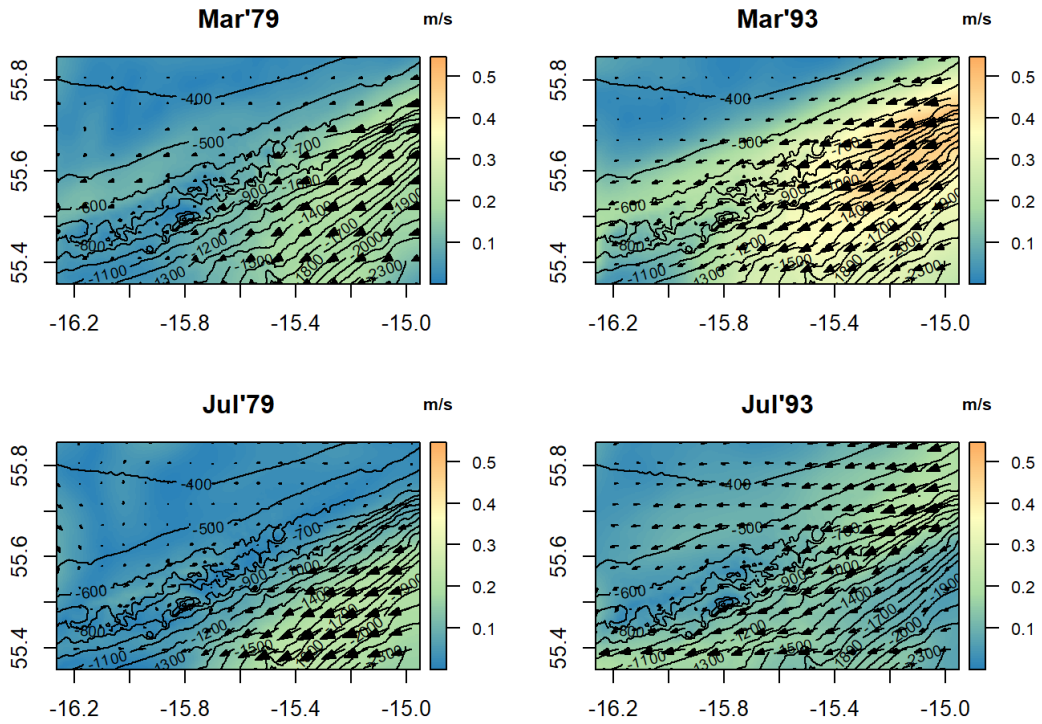

Figure 10: Depth averaged horizontal flow speed for March and July in 1979 and 1993.

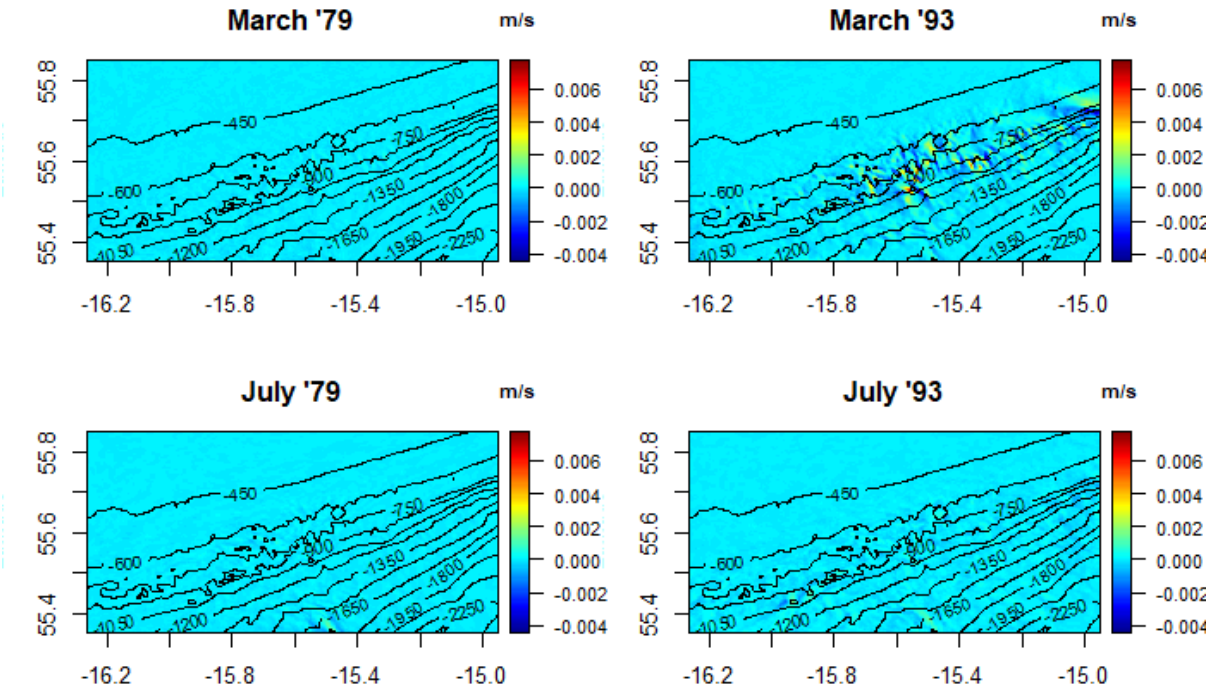

Figure 11: ROMS derived monthly averaged vertical velocity at the surface layer for the four modelled periods.

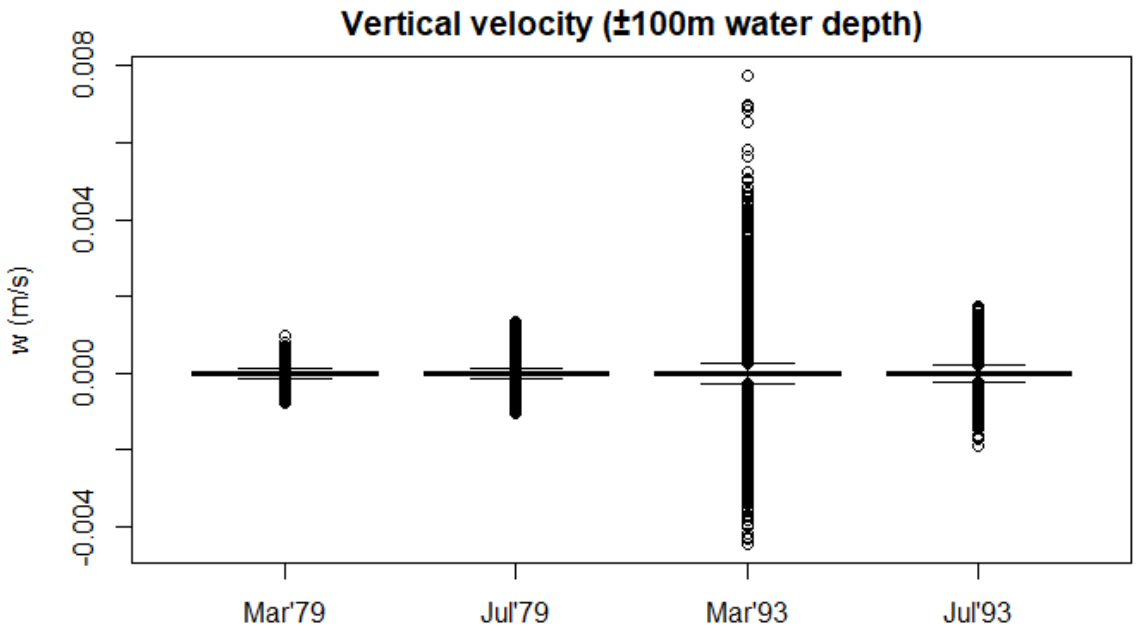

Figure 12: Boxplot of monthly averaged vertical velocities in the top layer for the four modelled periods.

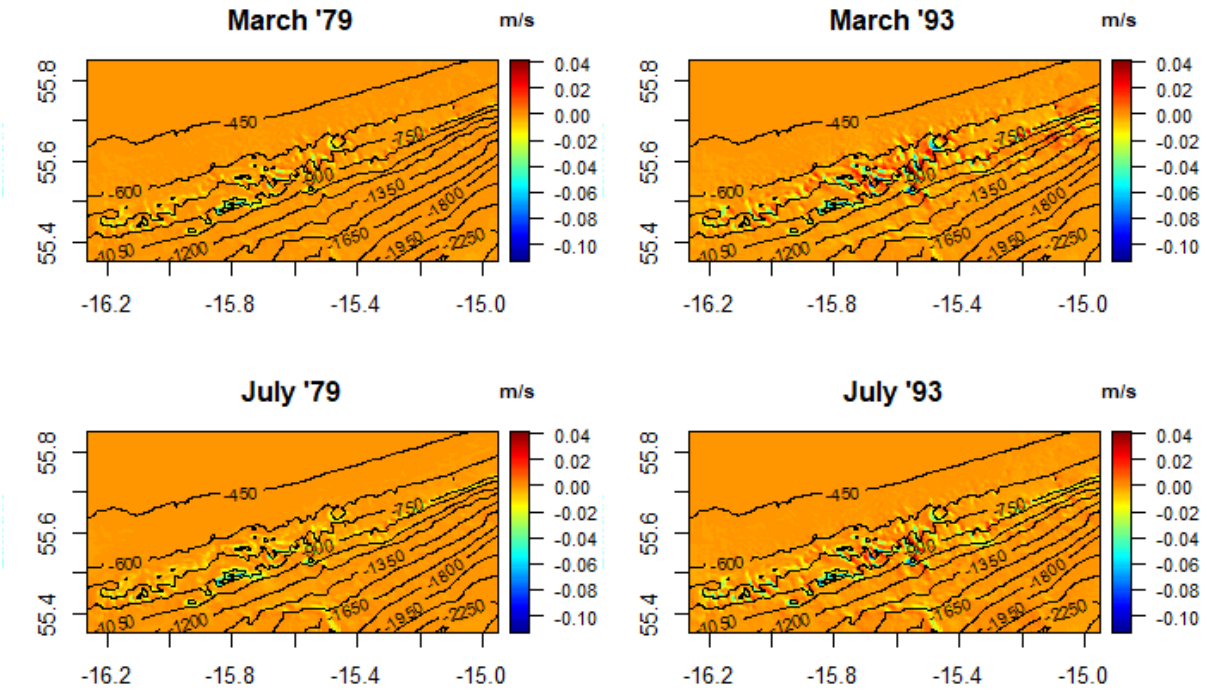

Figure 13: ROMS derived monthly averaged bottom layer vertical velocities for the four modelled periods.

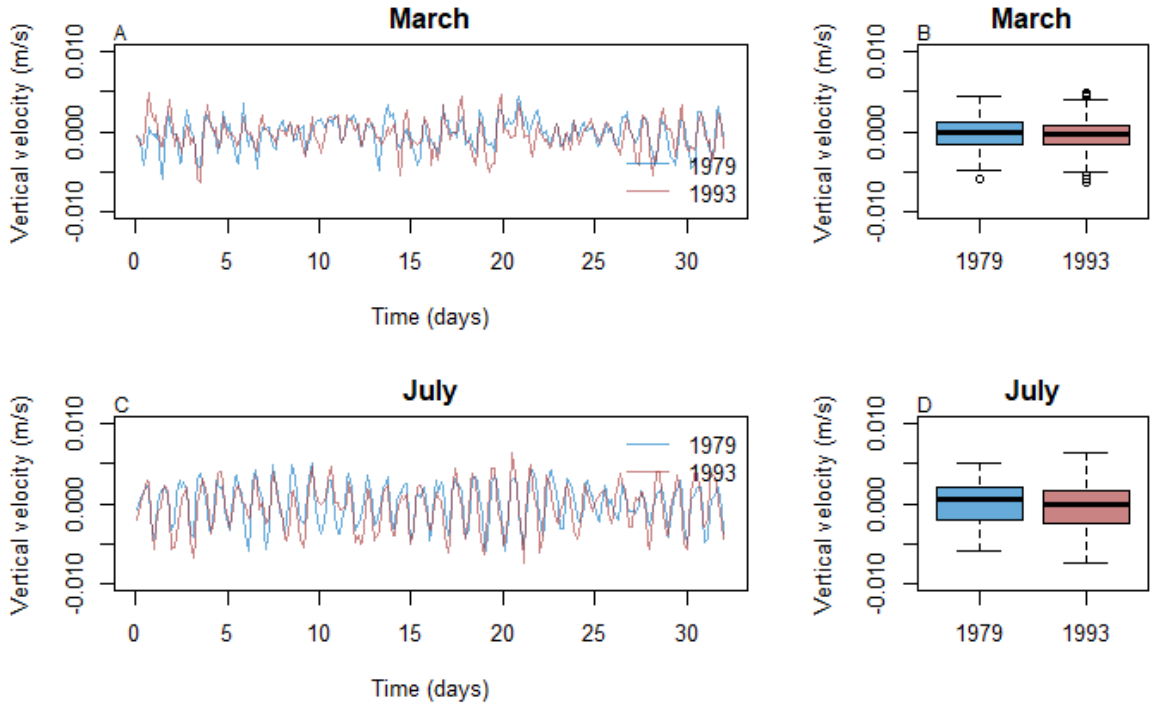

Figure 14: Time series of the ROMS derived vertical velocity (w) in m s^{-1} at the bottom layer of the Sediment Bank lander location. A-B) Compares March 1979 and 1993, C-D) Compares July 1979-1993. Note the different scale from Figure 15.

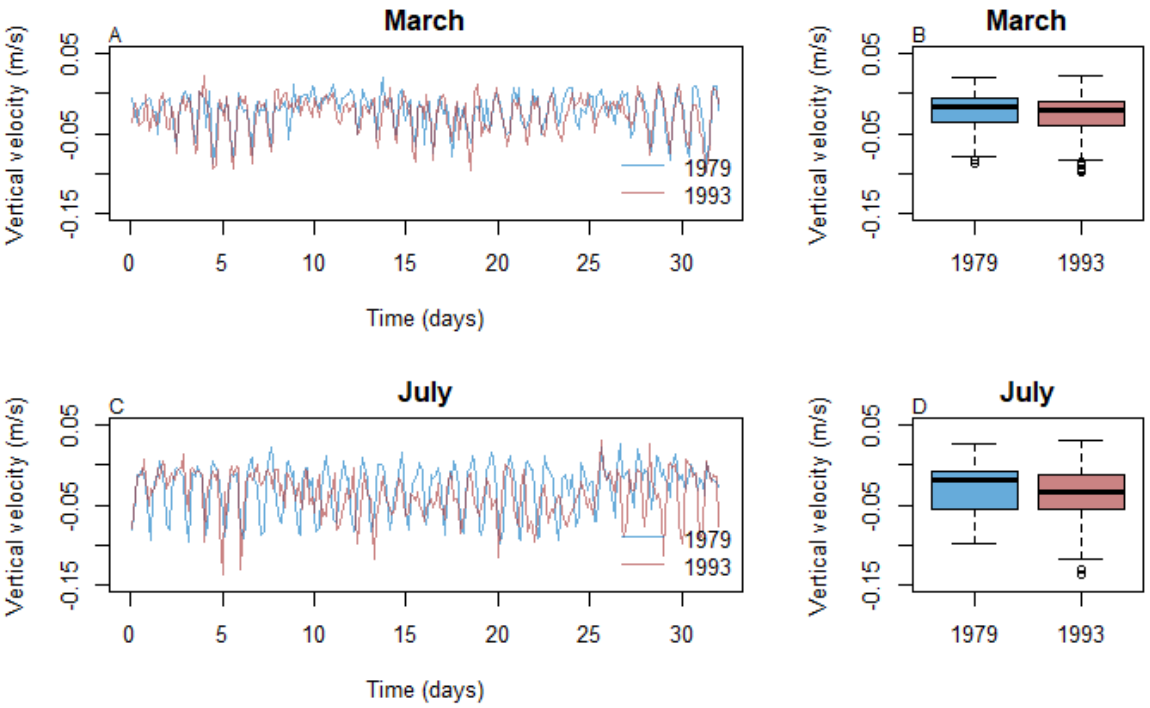

Figure 15: Time series of the ROMS derived vertical velocity (w) in m s^{-1} at the bottom layer of the Oreo mound lander location. A-B) Compares March 1979 and 1993, C-D) Compares July 1979-1993. Note the different scale from Figure 14.

4.4.2 Predicted suspended and sediment OM, coral biomass and benthic respiration

In step 1, during the spin-up phase, the model quickly converged to a (dynamic) equilibrium for the suspended organic matter concentration in three consecutive loops of each specific period. Initial results of POM transport model show the average POM concentration in the bottom water layer is higher in the low AMOC (1979) than in the high AMOC (1993) periods (Figure 16). After step 2, initial coral biomass and sedimentary organic matter show a similar distribution and as highest concentrations are found along the flank of Rockall bank, between 500 – 1000 metre depth (Figure 17 & Figure 18).

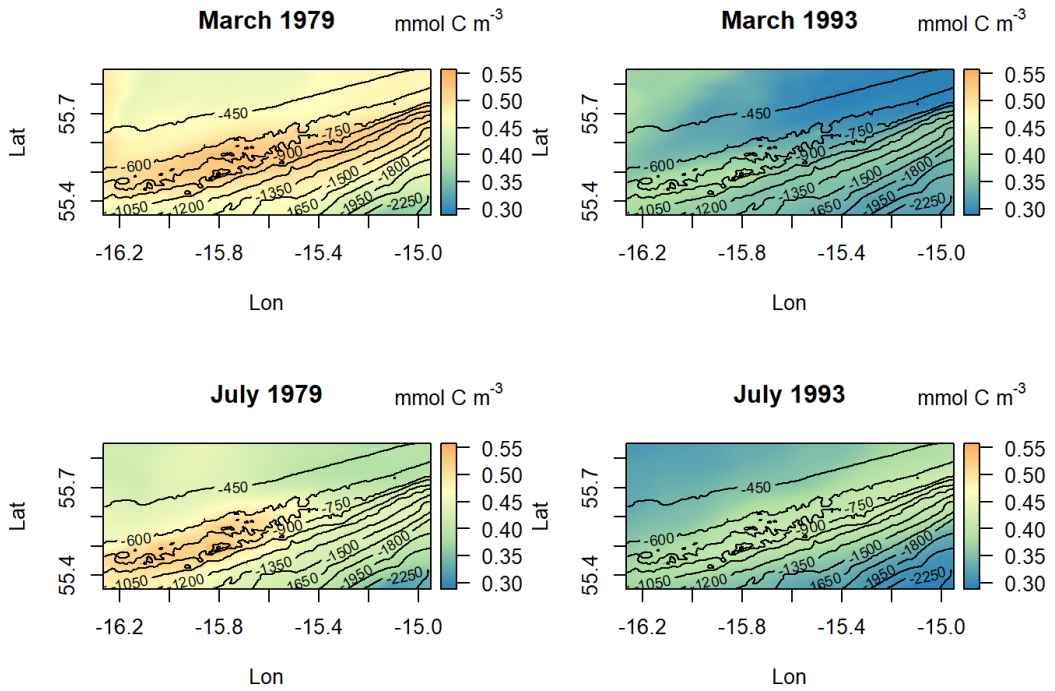

Figure 16: Average particulate organic matter (POM) concentration in mmol C m^{-3} in the bottom layer for the four modelled periods. Depth contour lines are indicated for reference.

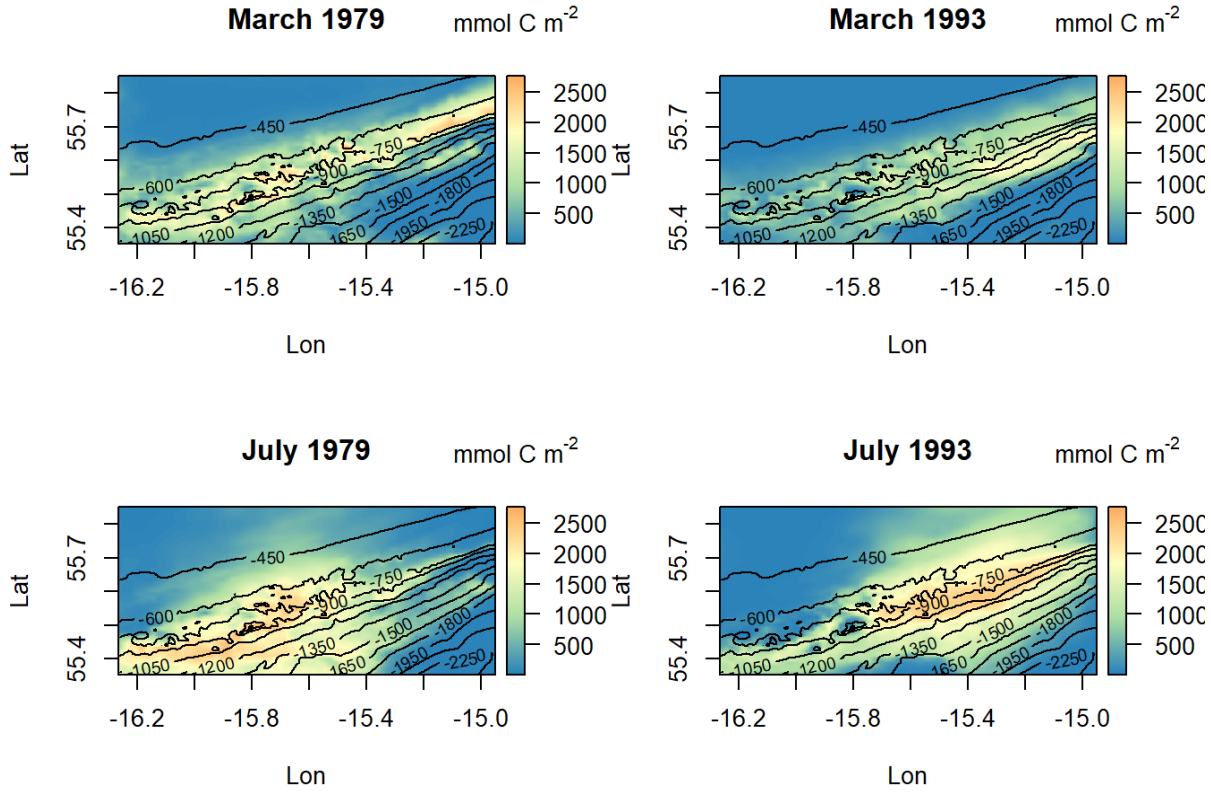

Figure 17: Initial cold-water coral biomass for March 1979, July 1979, March 1993 and July 1993.

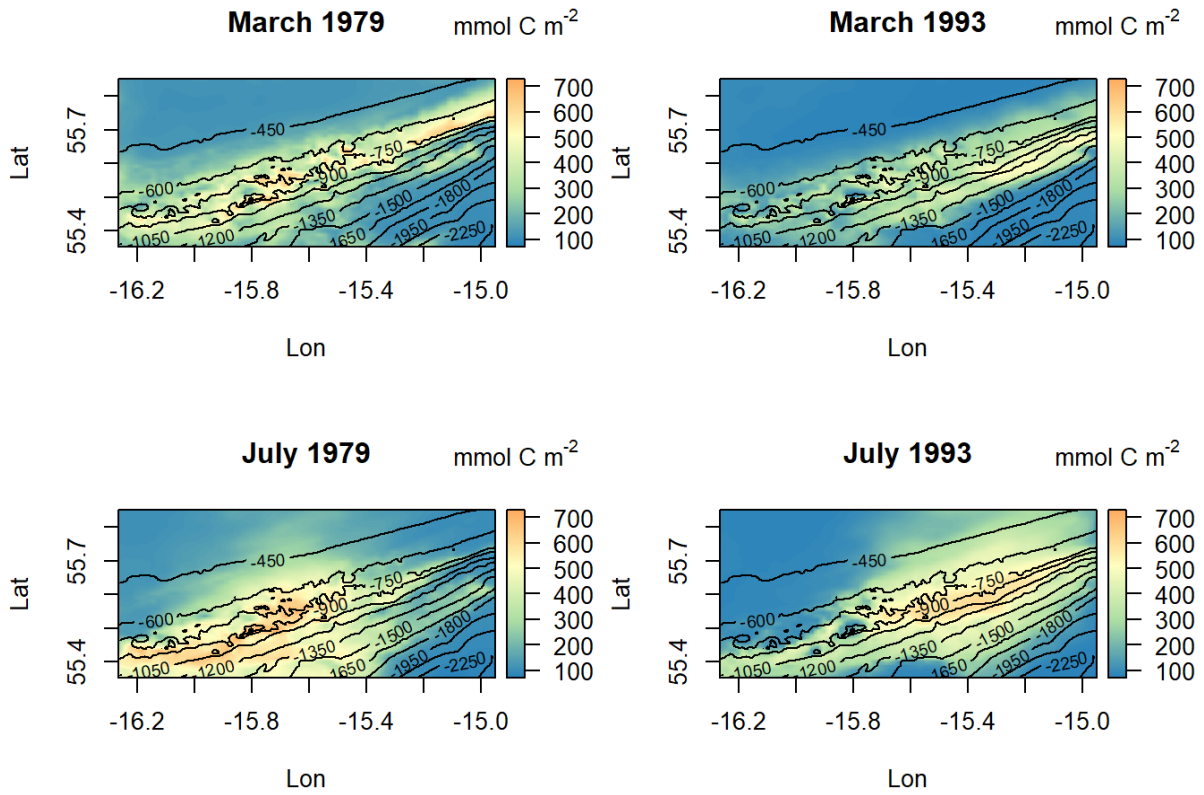

Figure 18: Initial sedimentary organic matter content for March 1979, July 1979, March 1993 and July 1993.

Running the model with the coupling between coral biomass and bottom layer POM concentration had a large effect on the bottom layer POM concentration. The POM uptake by corals was large enough to deplete bottom layer POM in areas with high coral biomass and comparatively low POM supply (Figure 19A and B). Taking July 1979 as an example, the POM around the coral mounds is largely depleted (Figure 17C). Due to the lower organic matter concentration in the bottom layer, coral biomass starts to decrease throughout the model domain, which implies that the initial biomass is an over-estimate of the biomass that can be sustained in the coupled model.

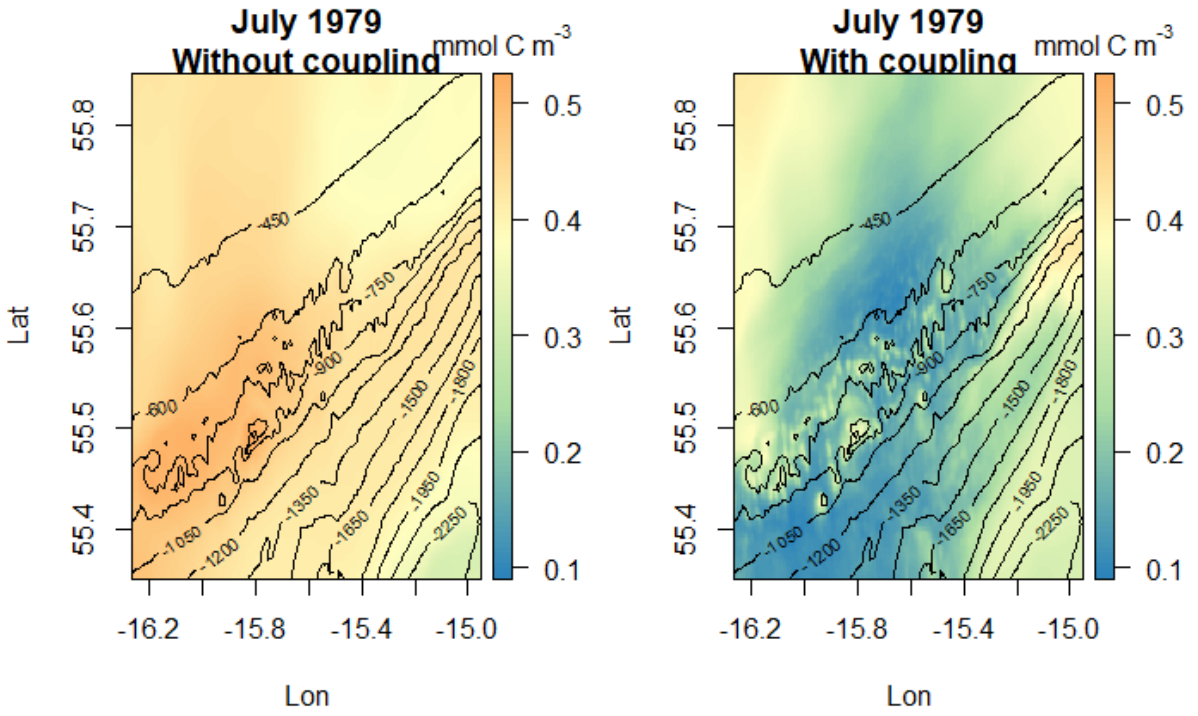

Figure 19: Average bottom layer particulate organic matter concentration for the first eight days without benthic-pelagic coupling (A) and with benthic-pelagic coupling (B).

The elevated downward vertical velocities in the high AMOC year (Figure 13) would intuitively give a higher POM concentration in the bottom layer. However, as earlier observed in the initial POM transport in step 1, we found a higher POM concentration in the bottom layer during low AMOC (Figure 20). This seems counterintuitive; yet, the POM concentration in the whole water column is lower in high AMOC versus low AMOC year, indicating a reduced POM flux from the surface layer (Figure 21). Hence, the increased downward transport of POM is compensated by a lower overall POM concentration in the model in March and July 1993. Note that the modelled bottom layer POM concentrations (0.2 – 0.5 mmol C m^{-3}) are only a fraction of the *in situ* recorded POM concentration of 3.7 mmol C m^{-3} (Kiriakoulakis *et al*. 2008). However, these measurements include non-refractory matter, while the modelled organic matter is characteristic of reactive, freshly produced organic matter (see Soetaert *et al*. 2016).

The resulting coral biomass estimates (Figure 22) show our mechanistic modelling approach can successfully model cold-water coral biomass based on hydrodynamics and particulate organic matter. The model results from the low AMOC year (1979) align well with the coral

distribution predicted by the habitat suitability model of Rengstorf *et al*. (2014), showing high coral biomass estimated on the coral mounds and decreasing to zero in the sediment areas. Overall, the sediment organic matter concentration followed the spatial distribution of the coral biomass (Figure 23).

When looking specifically at the different regions in the model domain (see Figure 3), the "coral" region shows the highest coral biomass in all four modelled periods. The coral biomass is 1.4 to 2.2 times higher in the weak AMOC state as opposed to the high AMOC state (Table 1). The model predicts consistently low coral biomass in the "shallow sediment" region, where the average coral biomass does not exceed 5.0 mmol C m^{-2} for all four modelled periods. We found also slightly elevated coral biomass values for the "deep sediment" region in each modelled time period. For example, in March 1979 shows coral biomass values up to 50 mmol C m^{-2} in an area deeper than 2000 metre (Figure 22 & Figure 24). However, coral biomass has not reached steady state yet. Producing output for these 3D coupled models proved to be computationally heavy and since the rate of change in coral biomass is directly proportional to the biomass, reaching steady state in areas with low biomass takes longer (Figure 25).

The maximum coral biomass found in each period (ranging from 836 to 1254 mmol C m^{-2}) was much lower than the assumed carrying capacity (6000 mmol m^{-2}) and also lower than coral biomass found in boxcores taken in the Logachev mound province (Deliverable 2.3 and de Froe *et al*., 2019). Although these are realistic values, our coupled model could underestimate CWC biomass. Due to overestimating the coral biomass during step 2, we set the net growth efficiency to a low value (NGE = 10%), while a NGE of 30% is more realistic for CWCs (Maier *et al*. 2019). Running consecutive model simulations with an NGE of 30% was, given the computationally heavy and time-consuming work, not feasible. It would be interesting to run future simulations with the NGE set to 30%, especially since coupling of the benthic and POM transport model turned out to so important for predicting coral biomass.

Benthic respiration, calculated with a DIC:O_2 ratio of 1:1 (Glud 2008), ranged from 2.3 to 53.3 mmol O_2 m^{-2} d^{-1} for all model simulations. In the shallow sediment region, averaged benthic respiration ranged from 3.2 to 4.8 mmol O_2 m^{-2} d^{-1}, which aligns well with SCOC values of marine sediments from comparable depths (Glud 2008). Zooming in on March and July 1979, we found a benthic respiration rate on coral mounds (e.g. Haas mound) of 20 – 50 mmol O_2 m^{-2} d^{-1}, which is consistent with *in situ* and *ex situ* measurements (Deliverable 2.3, de Froe *et al*. 2019). Averaged benthic respiration in the deep sediment area (3.8 – 5.1 mmol O_2 m^{-2} $d^{-1)}$

appear to be slightly overestimated, which is likely because coral biomass did not yet reach steady state equilibrium in this area.

Here, we show that the CWC biomass at Rockall Bank can be predicted based on suspended organic matter concentration and coral physiology. Only in areas of the model domain with sufficient organic matter supply, such as on coral mounds and coral ridges, coral biomass could develop and be sustained. We could not find a clear effect of season or AMOC state on the predictions of coral biomass. However, model predictions suggested that a weak AMOC state may be beneficial for coral development and that this was due to higher concentrations of suspended organic matter throughout the whole water column. It remained unclear if the high AMOC hydrodynamic forcing decreased downward export of suspended organic matter. In all, the coupled model seems suited for investigating changes in organic matter surface export, particle sinking velocity, physiological parameters of corals and hydrodynamics on cold-water coral biomass.

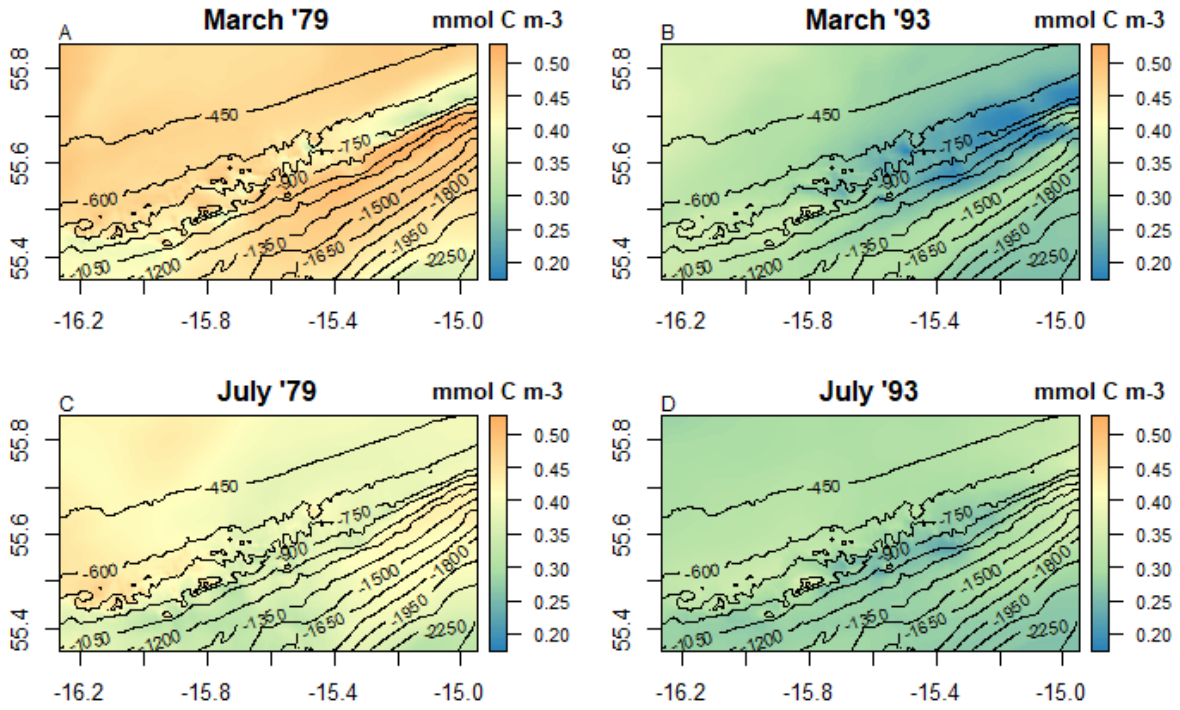

Figure 20: Averaged POM concentration in the bottom layer for the four modelled periods.

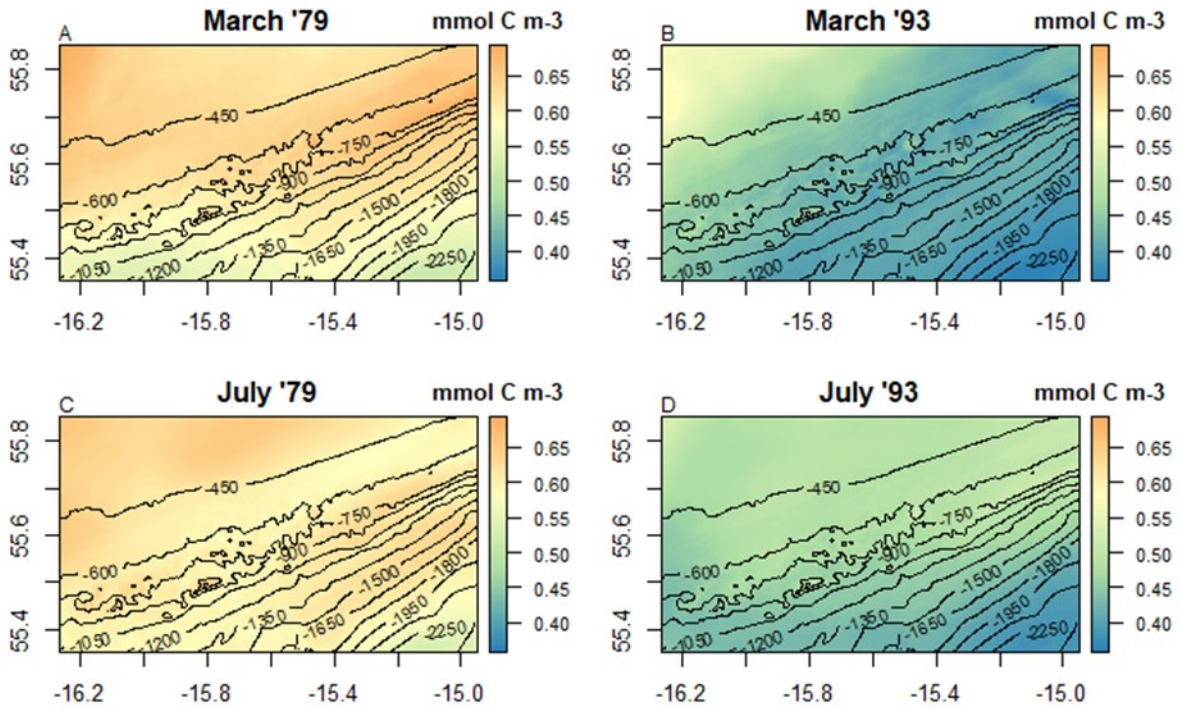

Figure 21: Averaged POM concentration for the whole water column and each modelled period.

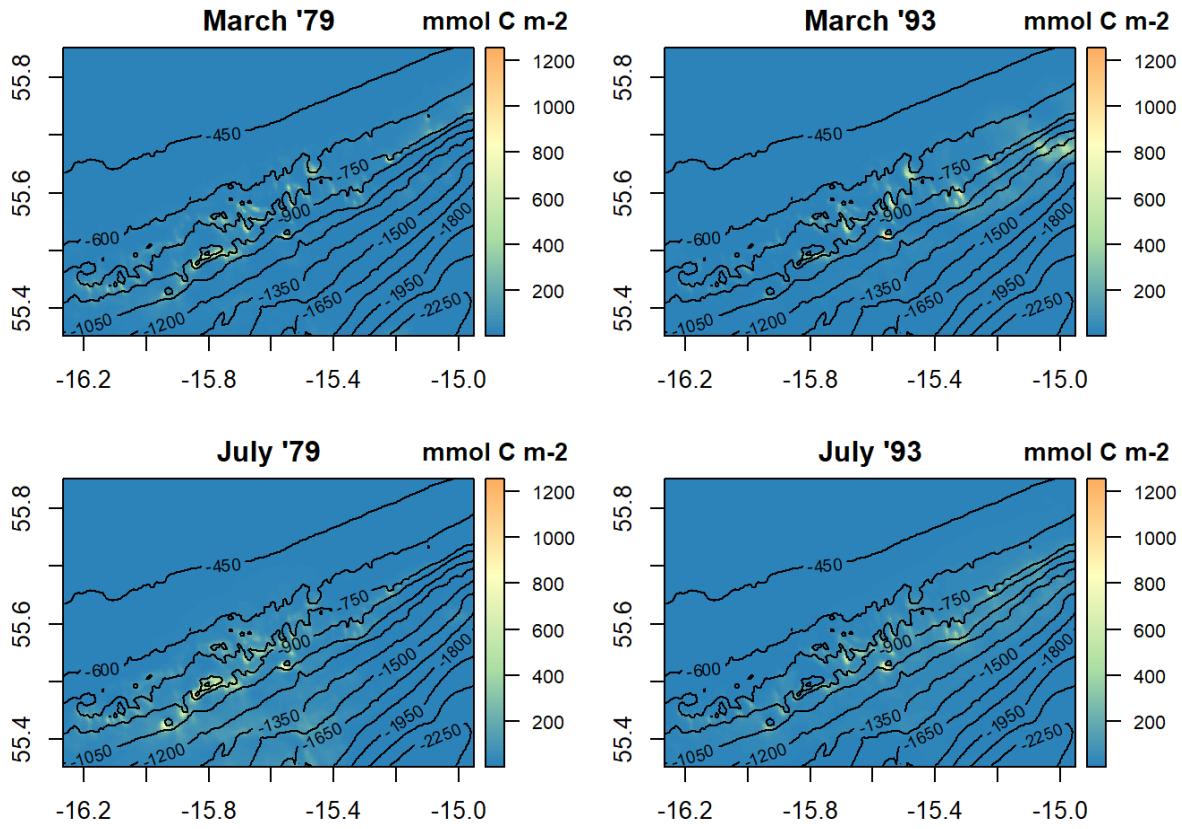

Figure 22: Predicted cold-water coral biomass by the coupled model (mmol C m^{-2}) for the periods: March 1979, March 1993, July 1979, March 1993.

Table 1: Cold-water coral biomass (mean ± SD) in mmol C m^{-2} for the four modelled time periods and regions.

Region	March ’79	July ’79	March ’93	July ’93
Sediment bank	2.5 (± 3.7)	4.6 (± 4.5)	1.3 (± 3.2)	3.7 (± 4.6)
Coral mound	87.7 (± 103.9)	119.8 (± 126.6)	53.5 (± 90)	62.9 (± 80.2)
Deep sediment	8.3 (± 10.8)	28.6 (± 31.7)	16 (± 40.3)	21.7 (± 22)
Off-mound	33.8 (± 57.3)	40 (± 57.3)	32.8 (± 54.8)	41.1 (± 50.4)

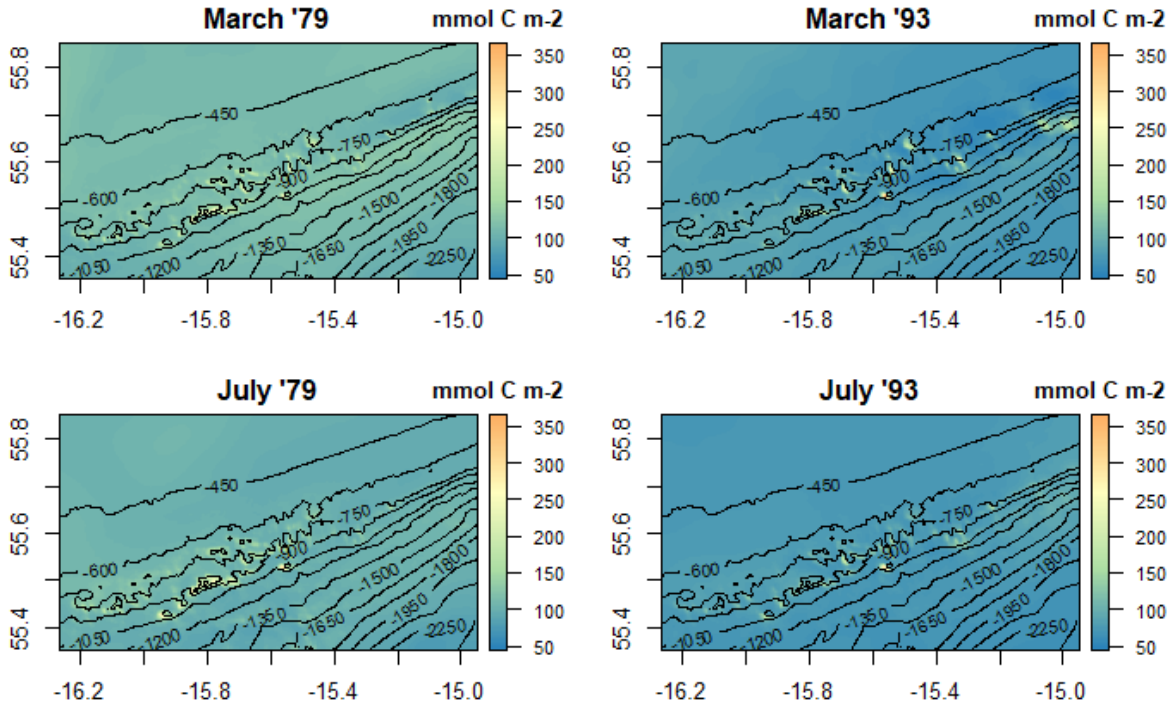

Figure 23: Final sediment organic matter concentration in mmol C m^{-2} for the four modelled periods.

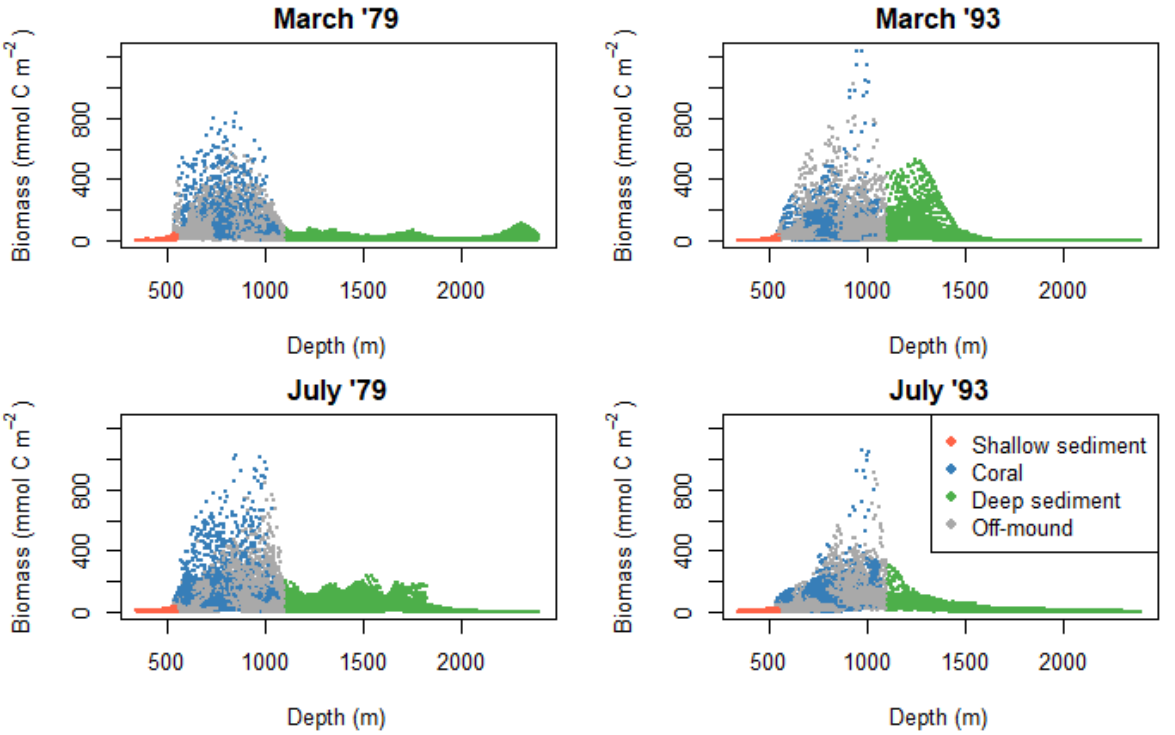

Figure 24: Cold-water coral biomass (mmol C m^{-2}) versus depth and coloured by region for the four time periods.

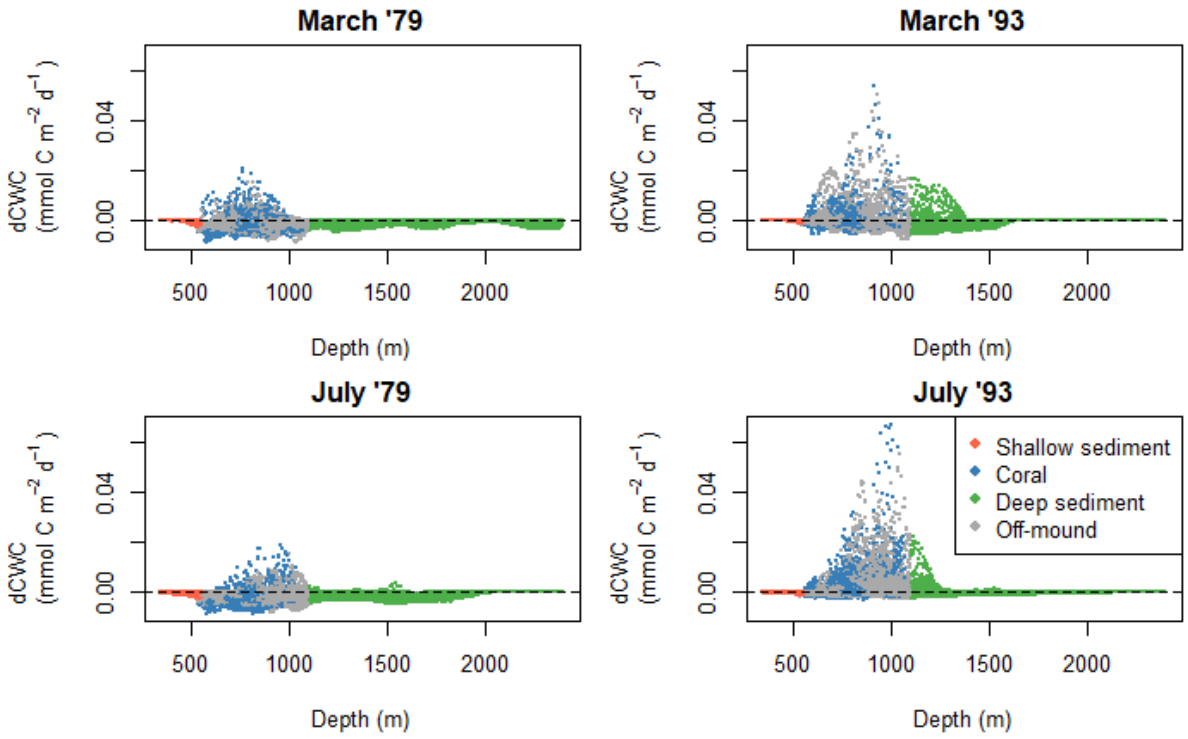

Figure 25: averaged change in cold-water coral biomass (in mmol C m-2 d-1) versus depth and colored by region. The dashed line indicates zero.

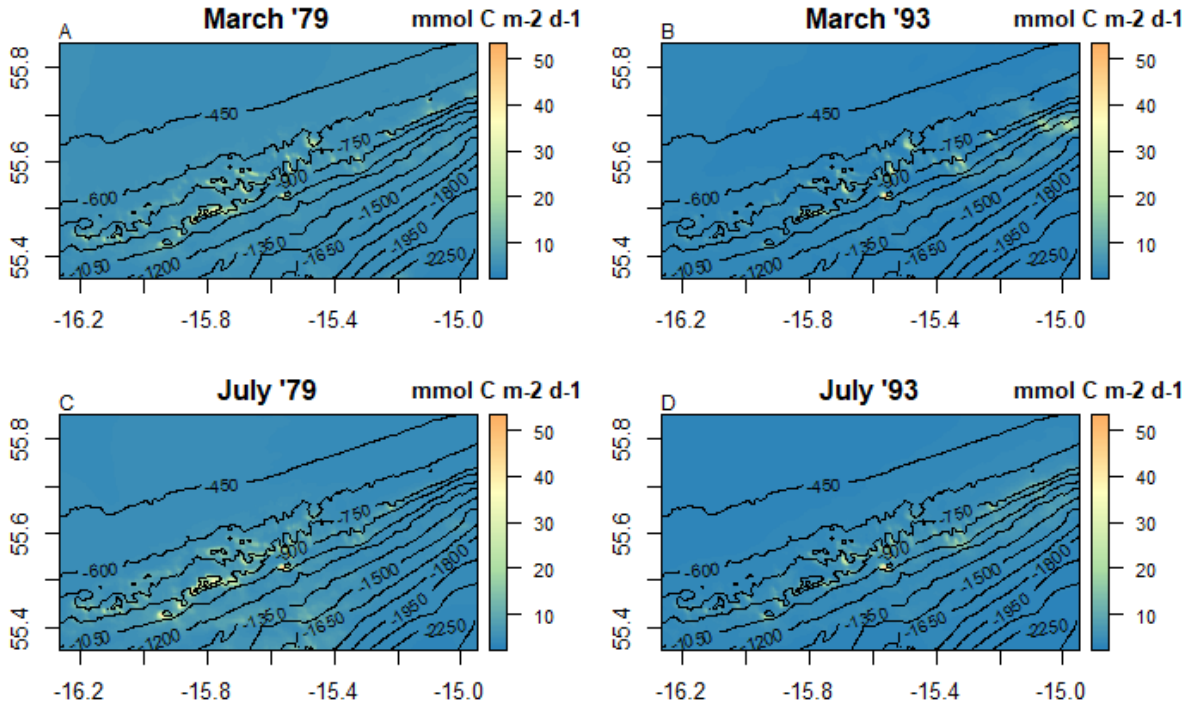

Figure 26: Benthic respiration (mmol C m^{-2} d^{-1}) for the four modelled periods.

5 Condor Seamount

5.1 Site description

5.1.1 Bathymetry

The Condor seamount is an elongated (35 km in length, 2 to 6 km wide) and relatively shallow volcano with its summit at ±200 m water depth, which lies 17 km SW off Faial Island in the Azores archipelago and is surrounded by abyssal depths (38°52'N; 29^{0}00'W, Figure 27). For decades, the seamount was targeted by local artisanal fisheries, mostly using hand- and longlines, but the lack of bottom trawling has maintained the coral gardens and deep-sea sponge aggregations of Condor in a relatively good state (Giacomello *et al*. 2013; Tempera *et al*. 2012). The absence of trawling pressure and the complete fishing moratorium that was effectuated in 2008 has made the seamount attractive to set up a long-term observatory, which resulted in extensive research activities between 2008 and 2012 (Giacomello *et al*. 2013). Based on detailed bathymetry, obtained prior to the instalment of the Condor observatory, Tempera *et al*. (2012) estimated that the seamount has a planar area of 432 km^2 and an estimated surface area of 447 km^2 (i.e. a surface to area ratio of 1.04). The following geomorphological, hydrographical and biological description is based on Tempera *et al*. (2012), except when indicated otherwise.

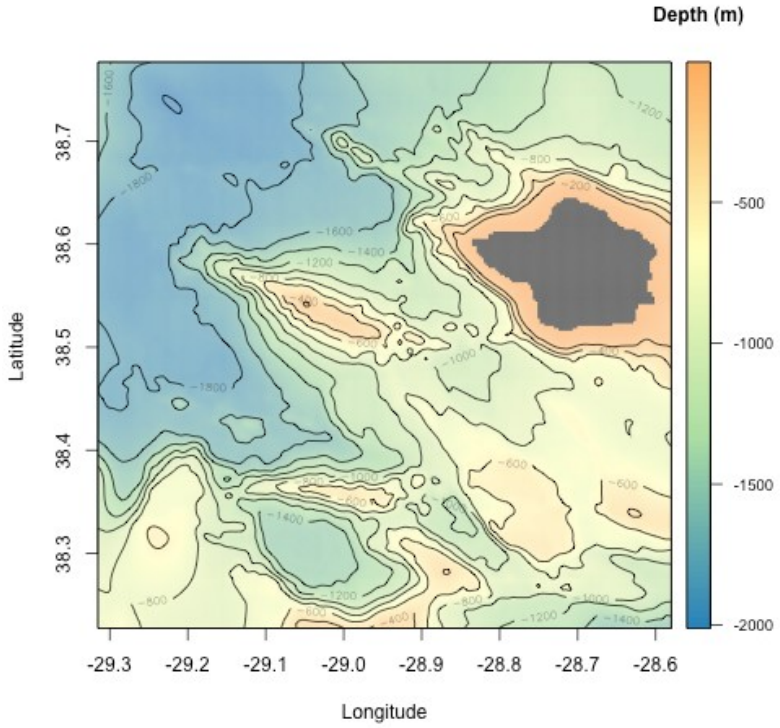

Figure 27: Model domain of the high-resolution ROMS model of the Condor seamount. Condor seamount is in the centre and Faial Island in the eastern part of the model domain.

5.1.2 Geomorphology

The seamount has a flat, broad summit area in the west and an elongated, relatively flat but narrower area of deeper elevation in the central and eastern sectors. Acoustic backscatter data indicates that the summit region is dominated by large rocky seafloor outcrops, boulders, and gravels. The flanks of the seamount are generally smooth, and seabed imagery here has revealed both unconsolidated sediments and areas where the sediment surface has been cemented into 10- to 15-cm thick plates. Sediment composition on the northern slope of the seamount was predominantly bioclastic down to a depth of 965 m, where it shifted into a predominantly volcaniclastic black sand.

5.1.3 Hydrography

The upper 100 m layer, i.e., close to the level of the summit, is a checkered pattern of temperature and salinity fields that consists of two upwelling centres (with higher turbidity levels) entwined with two downwelling centres. The centres of the anomalies were situated 5–7 km away from the seamount summit and collectively rotate around the seamount in an anticyclonic direction following a tidal period. Such structures typically originate when a part of the energy associated with the barotropic tide is trapped at topographic rises in the form

of internal tidal waves (Codiga & Eriksen 1997). Information provided by the two moorings deployed north and south of the summit confirmed a mean anti-cyclonical flow pattern around the seamount. Such quasi-closed circulation patterns (Taylor caps) form when the seamount is subject to a mean flow of moderate intensity but may also be produced by nonlinearity of a periodic tidal flow (Codiga & Eriksen 1997).

Tidal forcing is also responsible for periodic changes in thermocline depth over the seamount. Temperature anomalies, combined with data from the tide gauge on the Faial tidal station (http://oceano.horta.uac.pt/azodc/tidegauge.php), suggest that the thermocline was rising when water level was falling and vice versa. CTD profiles have further revealed that the upper mixed layer may extend down to 200 m depth during the cold season, therefore intersecting the seamount summit and possibly influencing its biological assemblages.

5.1.4 Biology

Video surveys have been made to a depth of 1,097 m, on which a preliminary vertical zonation of the benthic assemblages on Condor seamount has been made. Two habitats of conservation importance are found: coral gardens and deep-water sponge aggregations. The densest coral gardens were recorded on the seamount summit down to 287 m depth and were dominated by gorgonians (*Viminella flagellum*} and *Dentomuricea* sp. in association with tall hydroid (cf. *Polyplumaria flabellata*). *Viminella flagellum* and cf. *Polyplumaria flabellata* were predominantly found on hard grounds and occurred down to 480 m depth, *Dentomuricea* sp. seemed to be more abundant when the seafloor was covered with a thin sediment veneer. Sponge aggregations prevailed deeper and were found between 720 and 860 m depth. The deepest coral gardens were found between 968 and 1,001 m depth and were dominated by the gorgonian *Candidella* cf. imbricata and small yellow *Caryophyllidae*. In the present modelling approach, we focus on the *Viminella* dominated sponge gardens on the summit of Condor seamount.

5.2 Coupled model development

5.2.1 OM suspended matter

The output of the ROMS-Agrif model, stored at 3-hour intervals, was used offline to drive organic matter dynamics in the water column, including export of organic matter at the upper boundary, advective horizontal and vertical transport, constant decay and passive sinking.

ROMS-Agrif includes the effects of waves on the ocean currents by a moving surface boundary (Deliverable 2.4). This temporal stretching of the grid was ignored in the simulation of the organic matter dynamics to shorten simulation time. Conservation of momentum was imposed at each time step by calculating the upward flow rate *w* from the flux divergence of the horizontal flows and assuming that the free-surface elevation (η) is constant and that the vertical velocity at the bottom is zero $w_{z=0} = 0$.

$$\frac{\partial \eta}{\partial t} = 0 = \frac{\partial (H_z u)}{\partial x} + \frac{\partial (H_z v)}{\partial y} + \frac{\partial (H_z w)}{\partial z}$$

in which H_z is the grid-cell thickness.

The organic matter in the model is expressed in carbon equivalent (*C*). Following the conservation of momentum, the organic matter reaction model is given by:

$$\frac{\partial H_z C}{\partial t} = \frac{\partial (H_z u C)}{\partial x} + \frac{\partial (H_z v C)}{\partial y} + \frac{\partial (H_z w C)}{\partial z} - w_s \frac{\partial (H_z C)}{\partial z} - k H_z C$$

in which w_s is the sinking velocity, and *k* is the first-order decay rate.

Input into the model domain is represented by the carbon export at the base of the mixed layer depth. Henson *et al*. (2015) provides a model analysis of the carbon export and export efficiency in the ocean. For the Azores region, this modelling study finds an annual primary production of ±100 g C m^{-2} and a corresponding export efficiency of ±25%, which gives an annual export production of 25 g C m^{-2} or 5.7 mmol C m^{-2} d^{-1}. In a study on DOM concentrations and dynamics in the Azores front region, the authors report a spring/summer export flux (at 100 m water depth) of 0.1 - 0.15 g C m^{-2} d^{-1} (Doval *et al*. 2001), which is equivalent to 8.3 - 12.5 mmol C m^{-2} d^{-1}. Huskin *et al*. (2004) deployed sediment traps during summer (i.e. August 1998) at the base of the photic zone and found organic carbon export fluxes of 80 mg C m^{-2} d^{-1} (equivalent to 6.7 mmol C m^{-2} d^{-1}). The organic matter export across these studies align reasonably well and therefore we used an export flux of 8 mmol C m^{-2} d^{-1} for *F0* in the model.

The degradation rate of sinking organic matter is based on the formulation used in the MEDUSA model framework, which is defined as $k = 0.016 \times 1.066^T$ (Henson *et al*. 2015; Yool *et al*. 2011), in which *T* is temperature in ^oC. Temperature is seasonally variable with sea

surface temperature in the March of ±15 °C and November of 20 °C (Santos *et al*. 2013). The water temperatures however decreases with depth, with a temperature of ±12 °C at 500 m (Bashmachnikov *et al*. 2013). The present study therefore used a temperature of 15 °C, which gives a degradation rate *k* of 0.042 d^{-1}.

The attenuation of POC flux with depth is a product of both the degradation rate (*k*) of organic material and the sinking speed of the POC-containing particles (Marsay *et al*. 2015). *In situ* measurements of sinking velocities made in the Pacific Ocean, show that the sinking rate of organic matter can range from >820 to <2 m d^{-1} (Trull *et al*. 2008). Faster remineralisation and slower sinking both result in shallower POC remineralisation in tropical and subtropical areas, as observed in both modelling (Henson *et al*. 2015) and observational (Marsay *et al*. 2015) studies. To be consistent with the latter findings, we set sinking rate (w_s) to be relatively low at 5 m d^{-1}, largely consistent with the parameterisation of smaller sinking particles in the MEDUSA model (Henson *et al*. 2015).

5.2.2 Passive suspension feeders

The top of Condor seamount is a mixture of sediment patches and coral gardens, formed by the CWCs *Viminella flagellum*, *Dentomuricea* sp. and large primnoid gorgonians (Tempera *et al*. 2012). As *V. flagellum* dominates the biomass at Condor seamount, we base the physiological model largely on parameters representative for this species. The physiological model for this passive suspension feeders (PSF) has been described in detail in Deliverable 2.2 and is briefly summarised here:

$$\frac{dPSF}{dt} = AE_{PSF} \cdot NGE_{PSF} \cdot v_{bbl} \cdot OM_{bbl} \cdot A_{PSF} \cdot PSF \cdot \left(1 - \frac{PSF}{CC_{PSF}}\right) - m_{PSF} \cdot PSF$$

in which AE_{PSF} is the assimilation efficiency of PSF (-), NGE_{PSF} the net growth efficiency of PSF (-), v_{bbl} is the current velocity (i.e. $\sqrt{u_{bbl}^2 + v_{bbl}^2}$) in the benthic boundary layer (m d^{-1}), OM_{bbl} is the organic matter concentration in the benthic boundary layer (mmol C m^{-3}), A_{PSF} is the carbon-specific surface area for PSF (m^2 $mmol^{-1}$ C), CC_{PSF} is the carrying capacity of PSF biomass on the seafloor (mmol C m^{-2}) and m_{PSF} is maintenance respiration (d^{-1}). Values for v_{bbl} and OM_{bbl} are calculated by the coupled hydrodynamic-biogeochemical model. The

remaining physiological parameters are largely based on experiments conducted within ATLAS and otherwise on literature as detailed below.

Measurements of the assimilation efficiency of CWCs are not available as these are often difficult to obtain, because the non-assimilated part of the food cannot be distinguished from particulate mucus produced by the coral (Wild *et al*. 2008). However, the relative release of particulate organic matter (i.e. non-assimilated matter and mucus) is comparatively small (Maier *et al*. 2019) and the AE_{PSF} was therefore set to 0.9, consistent with values reported for tropical corals (Anthony *et al*. 2002).

Rakka *et al*. (in prep) conducted feeding experiments, in which the two dominant CWCs *D. meteor* and *V. flagellum* were fed with isotopically enriched ^{13}C-DOM, ^{13}C-diatom and living ^{13}C-rotifers (see Deliverable 2.2 for details). The assimilation of these food sources into the coral tissue and subsequent respiration of the ^{13}C labelled food source allowed calculation of the net growth efficiency. Surprisingly, the net growth efficiency for *V. flagellum* varied largely from 0.01 for diatoms, 0.20 for DOM and 0.82 for rotifers. Part of this range in values is due to the transient nature of stable isotope tracer studies (Maier *et al*. 2019), but this range is nevertheless very broad. As the available food at Condor seamount will be a mixture of these food sources, we set the NGE_{PSF} to the average 0.34. This value is comparable to the net growth efficiency estimated in a detailed physiological study of the cold-water coral *Lophelia pertusa* (Maier *et al*. 2019).

The biomass-specific surface area, i.e. A_{PSF}, is based on surface area measurements of *V. flagellum*, assuming a cylindrical shape and the C-based biomass of that species. Data from *V. flagellum* specimens from the feeding experiments were used for these measurements and gave a A_{PSF} of 1.73x10^{-4} ± 9.6x10^{-5} m^{-2} mmol^{-1} C.

The carrying capacity of PSF is based on the maximum density on the top of Condor seamount observed from Hopper camera images (5.5 m^{-2}, M. Rakka unpub. data), which is converted to biomass using the average biomass of 16 g DW m^{-1} height (estimated from fragments used in feeding experiments, see Deliverable 2.2), an average specimen height of 1.5 m and an organic C content of 8%. These parameters give a maximum biomass of 890 mmol C m^{-2} and we set the carrying capacity slightly higher to 1,000 mmol C m^{-2}.

Biomass-specific respiration has been measured during incubations in the ATLAS experiments (Deliverable 2.2) and amounts to 0.0038 d^{-1}, which was used for the m_{PSF}.

5.2.3 Sediment organic matter

The sediment biogeochemistry is modelled as a single sedimentary organic matter pool, which is fuelled by deposition from the water column and input of non-assimilated food from the passive suspension feeders and is degraded following first-order dynamics:

$$\frac{dOM_{sed}}{dt} = w_s \cdot OM_{sus} + (1 - AE_{PSF}) \cdot PSFingestion - k_{sed} \cdot OM_{sed}$$

in which $PSFingestion = v_{bbl} \cdot OM_{bbl} \cdot A_{PSF} \cdot PSF$. The sedimentary degradation rate (k_{sed}) is set to 0.041 d^{-1} (equivalent to 15 y^{-1}), which is characteristic for degradation of fresh organic matter (Westrich & Berner 1984).

5.3 Three-step solution to solve the coupled model

The biogeochemical transport-reaction equations were numerically solved on a staggered grid (Arakawa C-grid) with the organic matter concentration defined in the centre of each box and the flows on the grid cell interfaces. The 3-hourly velocity data from the hydrodynamic model were linearly interpolated in time to obtain velocity fields at each model integration step. The organic matter model comprised about 1.7×10^6 equations and was numerically integrated using a variable-order Adams-Moulton predictor-corrector scheme, as implemented in the R-package deSolve (Soetaert & Petzoldt 2010) running in the open-source software R (R Development Core Team 2015). Advection was implemented using simple first-order upwind differencing; due to the numerical dispersion that this generates, no horizontal or vertical dispersion was used.

The coupled model was solved for March and July in the weak (1979) and strong AMOC (1993) state. The organic matter flux (*F0*) was assumed to be identical for both months and we assumed no spatial variation in the model domain in order to obtain a faster steady-state and to allow focussing on the impact of location within the model domain and on effect of AMOC state on changes in food availability and predicted PSF biomass. In step 1, the initial conditions for the suspended organic matter concentration were calculated by starting from an suspended organic matter profile based on a simple exponential decay and then subjected a loop of 4 consecutive cycles of hydrodynamic forcing for a specific period (provided by the ROMS-Agrif model, see Deliverable 2.4). The suspended organic matter concentration at the end of these 4 cycles was stored as initial condition for the suspended organic matter. In step 2, the initial biomass of PSF and sediment organic matter throughout the model domain was

calculated based on the suspended organic matter concentration in the bottom layer from Step 1. In step 3, we ran the fully coupled model by taking the initial suspended organic matter concentration (Step 1), initial biomass of PSFs (Step 2) and sediment organic matter concentration (Step 2) and running the model for 2 consecutive loops of the respective period to arrive at a (dynamic) equilibrium state of the organic matter concentration in the water column, biomass of PSFs and sediment organic matter.

5.4 Results and Discussion

5.4.1 AMOC differences on hydrography

Figure 28A shows the model domain with a transect line across the Condor seamount that is used to show some of the model results below and B is the ROMS sigma grid along this transect line.

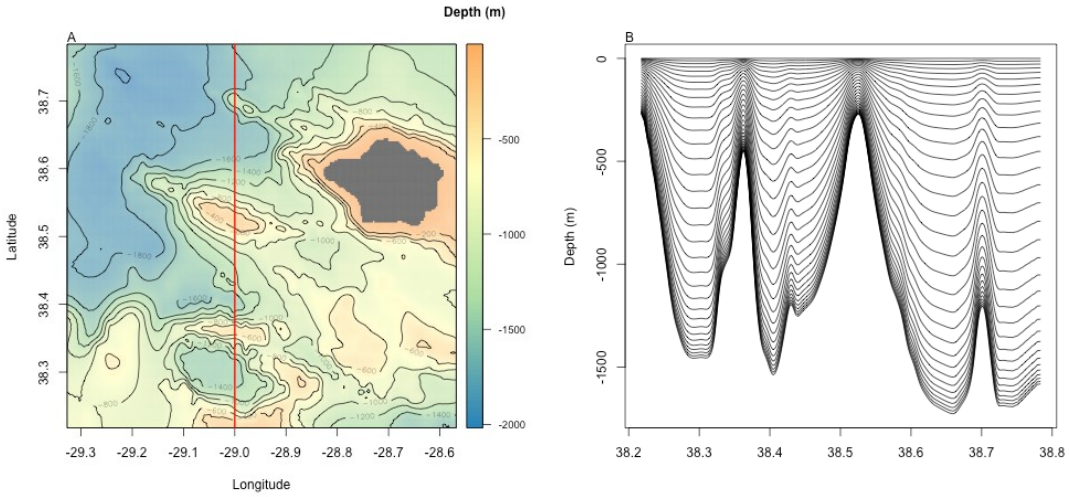

Figure 28: A) Bathymetry of the model domain, with a transect drawn across the Condor seamount (red line) and B) the sigma-grid of the ROMS-Agrif model along this transect.

As described above, the VIKING20 model showed small differences in bottom and depth-averaged current velocities between the two AMOC periods, with reduced velocities in the weak AMOC period and elevated velocities in the strong AMOC period (Figure 1 and Deliverable 2.4). We here investigate whether differences in hydrodynamics are also apparent in the ROMS-Agrif simulations, in which tidal forcing is included.

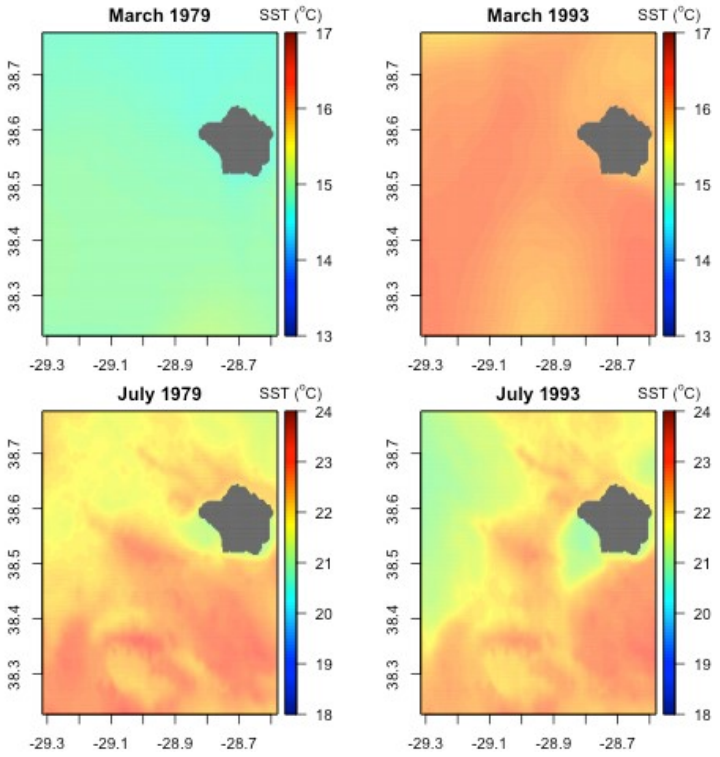

Figure 29: Sea surface temperature in the 4 investigated periods.

Sea surface temperature (Figure 29) and salinity (Figure 30) are evidently lower in March 1979 versus March 1993, but the situation for July 1979 and 1993 is much more comparable.

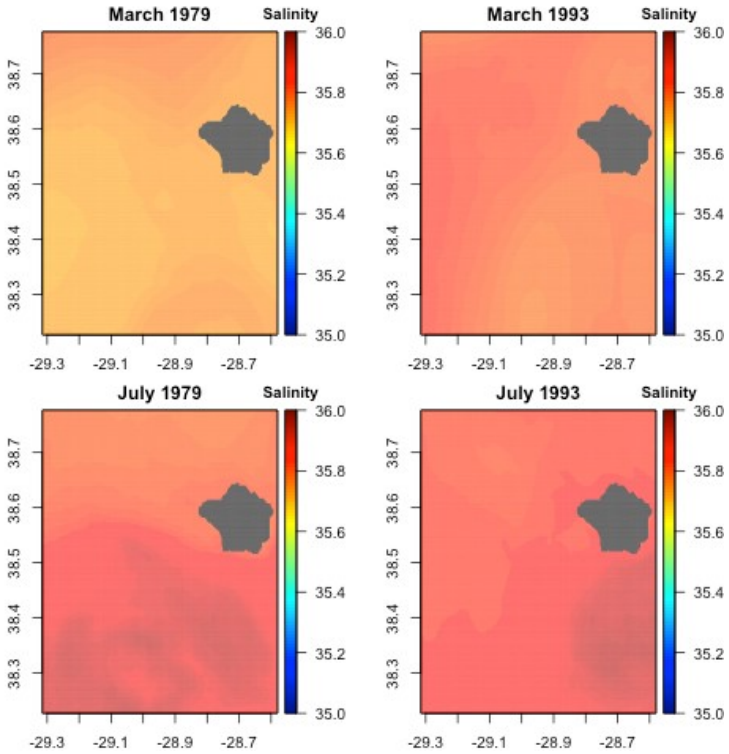

Figure 30: Sea surface salinity in the 4 investigated periods.

Temporal dynamics of the surface currents in the ROMS model domain show frequent passing of eddies through the area (temporal data not shown). Mean surface flow vectors for the four different periods do however show that the magnitude of the current velocities is comparable for the four periods, but that the currents are concentrated in different areas of the model domain (Figure 31).

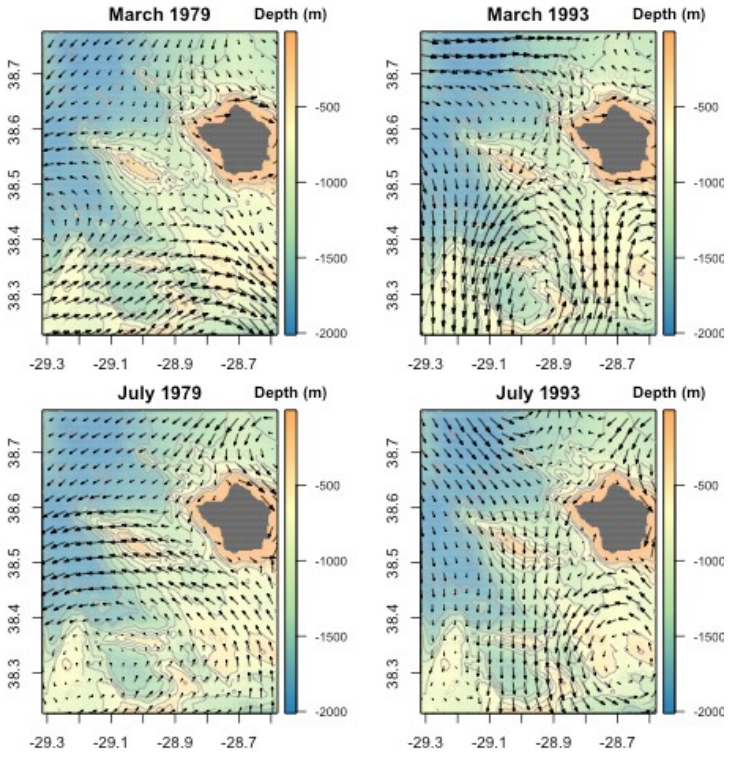

Figure 31: Current velocity vectors in the four periods from ROMS. The largest vector corresponds to a current velocity of 0.30 m s^{-1}.

The temporal dynamics of the bottom currents show a different and much more erratic picture (Figure 32). Maximum currents are of similar magnitude as the surface currents, with no clear differences in the bottom currents between spring/summer of 1993 as compared to 1979. Around the Condor seamount, highest current velocities are concentrated on the south-eastern and north-western ends of the seamount, with a smaller current going across the main axis of the seamount.

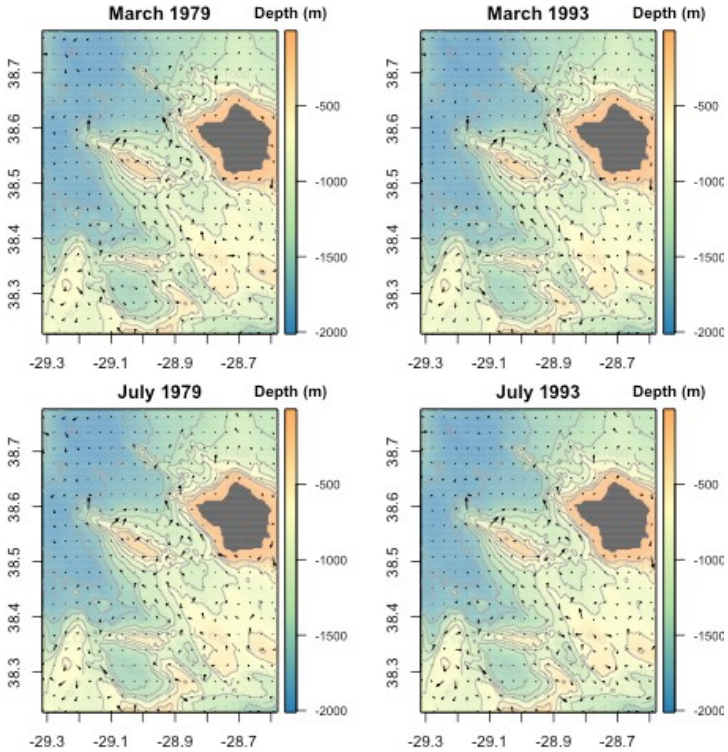

Figure 32: Current velocity vectors in the four periods from ROMS. The largest vector corresponds to a current velocity of 0.26 m s^{-1}.

Important hydrodynamic variables for organic matter availability for the coral community are 1) bottom current velocity, as higher currents increase organic matter uptake from the water column (see section 5.2.2) and 2) vertical current velocity, as the resulting downwelling of surface-derived organic matter increases availability at depth. The bottom velocity (Figure 33) and vertical velocity (Figure 34) show small and local differences between the investigated periods, but the pattern for the whole model domain is broadly comparable.

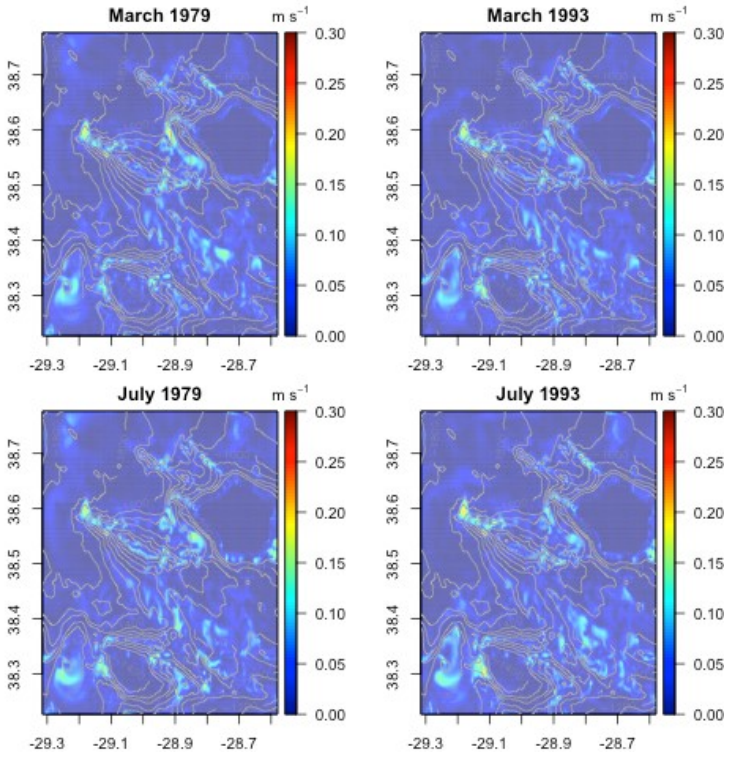

Figure 33: Bottom velocity in the four periods from the ROMS simulations.

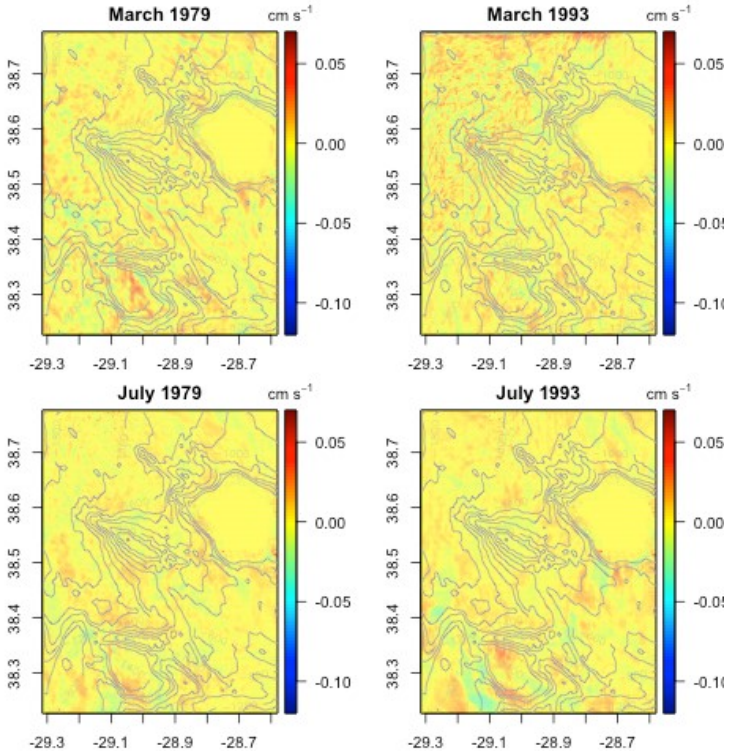

Figure 34: Vertical velocity just below the mixed layer in the four periods from ROMS.

We zoom in further on these hydrodynamic variables between AMOC states and seasons after defining different areas at the seamount. The Condor seamount is defined to be within the 1,700 m depth contour, the summit area is defined as seafloor less than 300 m deep and the northern and southern slopes are defined between the 1,700 and 300 m depth contours (Figure 35).

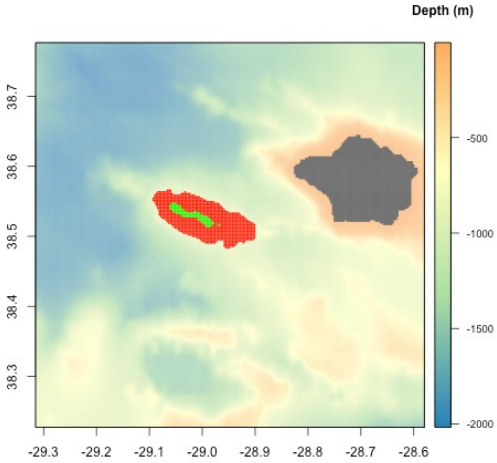

Figure 35: Zonation for the Condor seamount, with summit indicated in green and the flanks in red.

For the different zones in the model domain, also the boxplots show that the bottom and vertical velocities are comparable between seasons (Figure 36). However, this analysis also shows that the bottom velocity on the flanks (median ±0.03 m s^{-1}) and even more so on the summit (median ± 0.05 m s^{-1}) is higher as compared to the full model domain. Likewise, the median vertical velocity is around zero for the full model domain, but negative (i.e. downward direction) above the flanks (median ± -0.01 cm s^{-1}) and summit (median ± -0.03 cm s^{-1}).

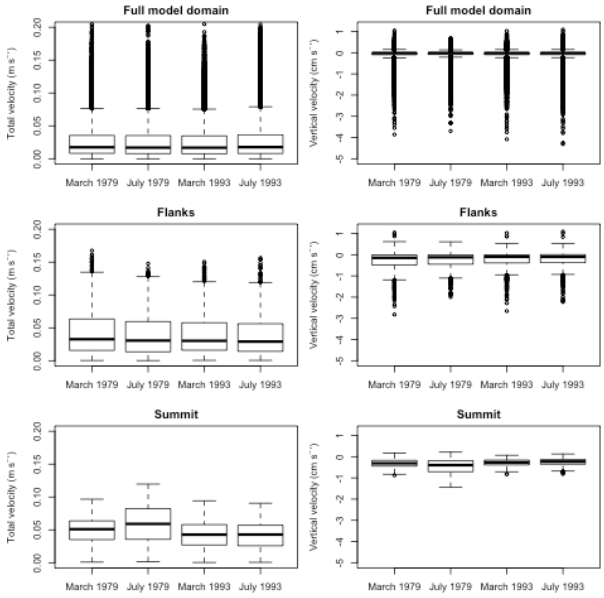

Figure 36: Boxplots of total velocity (m s^{-1}) and vertical velocity (*w*, cm s^{-1}) in the full model domain (top row), flanks of the Condor seamount (middle row) and summit (bottom row) of the Condor seamount for the four investigated periods.

Finally, we selected specific sites along the flanks (sites 1, 3-5) and the summit (site 2) on Condor seamount (Figure 37) for which the time series of total bottom velocity (Figure 38) and vertical velocity (Figure 39) are plotted. The time series clearly show an impact of tides on the bottom velocity at all sites (Figure 38). Differences in the total bottom velocity are small between periods, although March 1979 seems to be associated with higher velocities at the south-eastern tip of Condor seamount. The influence of tides is also apparent in the vertical velocities (Figure 39), but the magnitude is smaller than for bottom velocity.

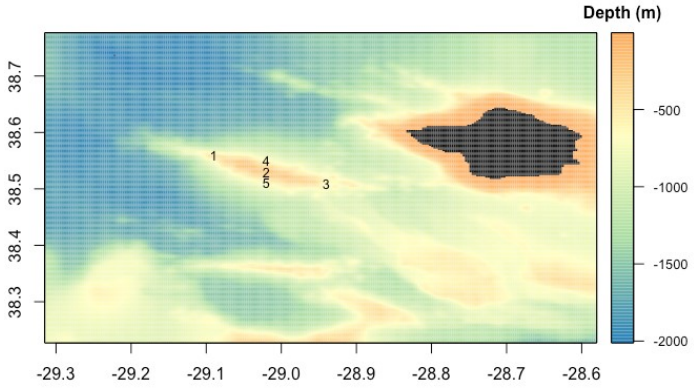

Figure 37: Map of Condor seamount with sites on the flank (1,3-5) and summit (2).

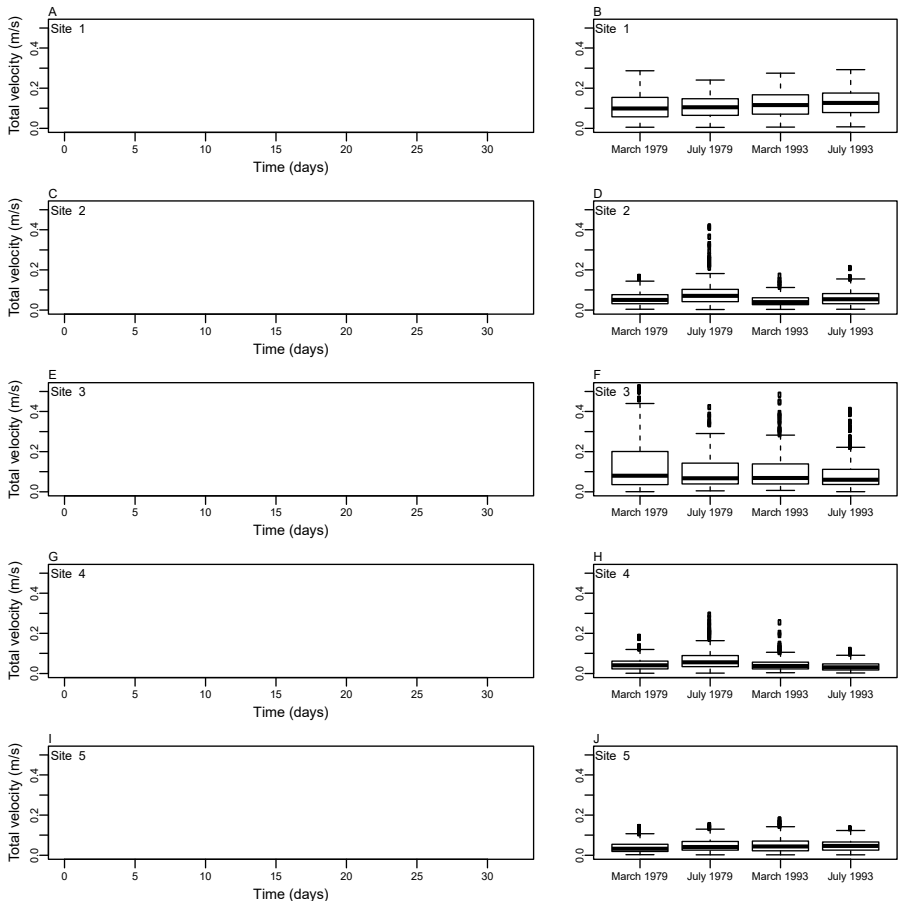

Figure 38: Time series (A,C,E,G,I) and boxplots (B,D,F,H,J) of the bottom velocity of the sites 1-5 on Condor seamount.

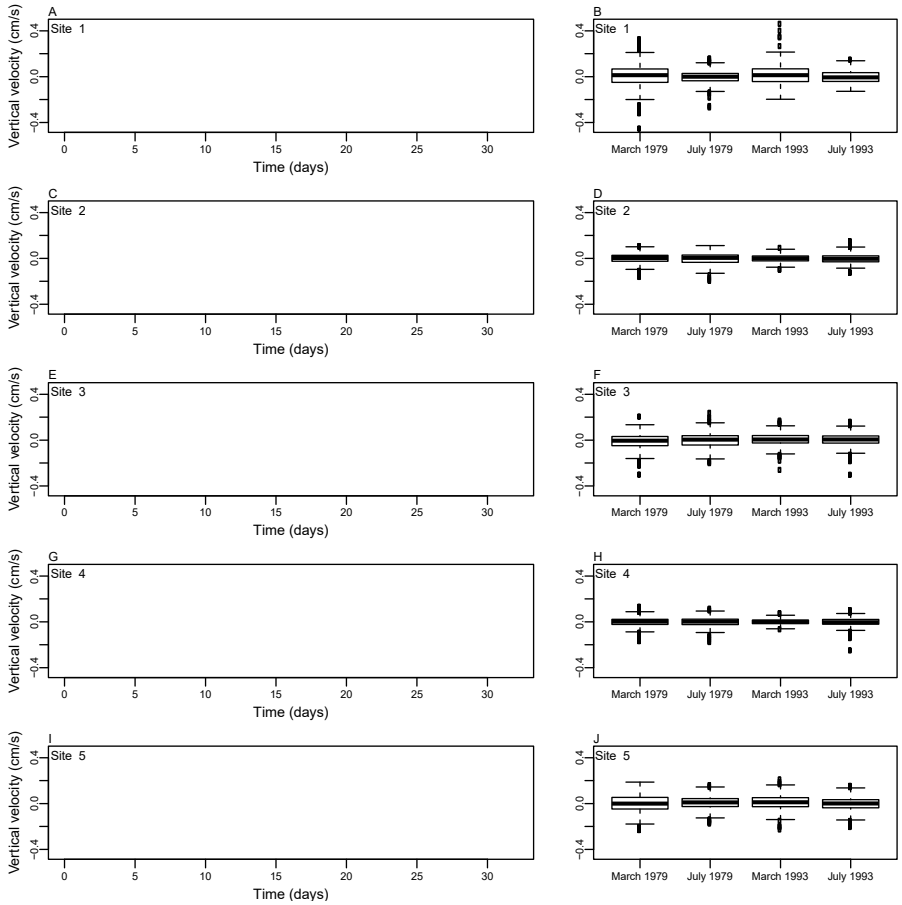

Figure 39: Time series (A,C,E,G,I) and boxplots (B,D,F,H,J) of the vertical velocity of the sites 1-5 on Condor seamount.

In all, the results from the ROMS-Agrif simulations show a congruence in hydrodynamics between the selected simulation periods. What the implications are for the food availability and PSF biomass will be shown and discussed in the next section.

5.4.2 Coupled model results of suspended matter, PSF biomass and benthic respiration

The initial suspended organic matter concentration (output of Step 1) along the north-south transect over Condor Seamount for the different periods is shown in Figure 40. It is clear that there is downward transport of organic matter towards the Condor Seamount in all four periods. Transient dynamics show that these downward pulses are episodic but are focussed towards the seamounts in the region (transient data not shown), similar to the food pulses observed in Soetaert *et al*. (2016). The initial bottom layer suspended OM concentration shows elevated a concentration at the Condor Seamount, but also in deeper parts of the model domain, especially in the south-eastern region (Figure 41). Noteworthy is the high bottom layer concentrations in March 1979, which are higher than in any of the other periods.

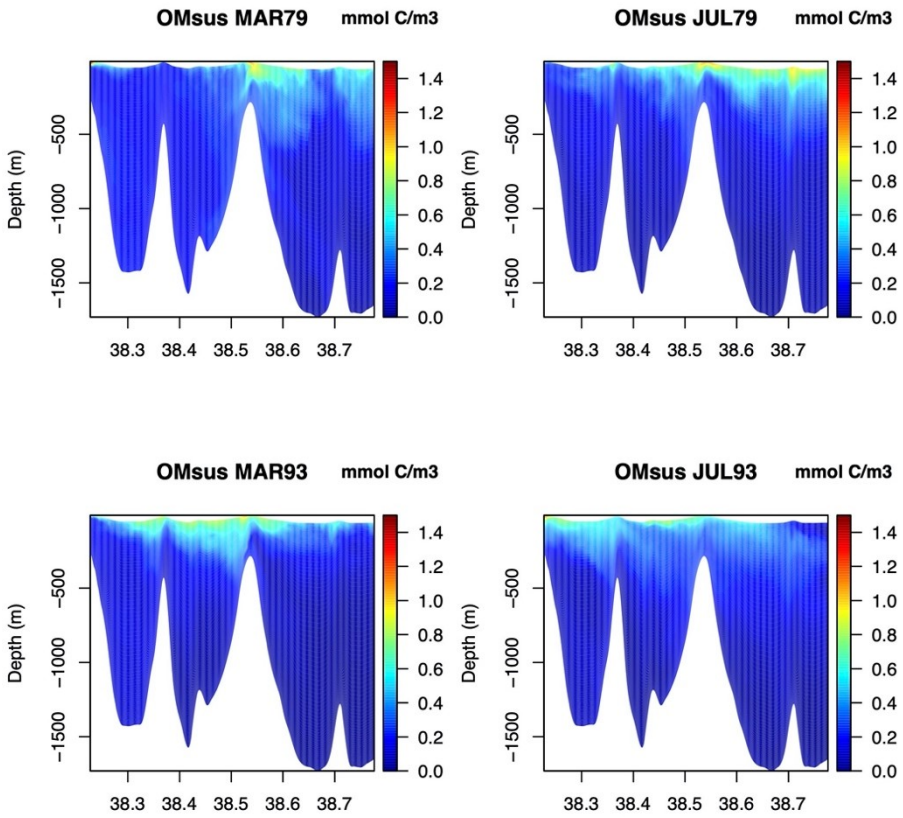

Figure 40: Initial (i.e. Step 1) suspended matter concentrations along the transect over Condor Seamount.

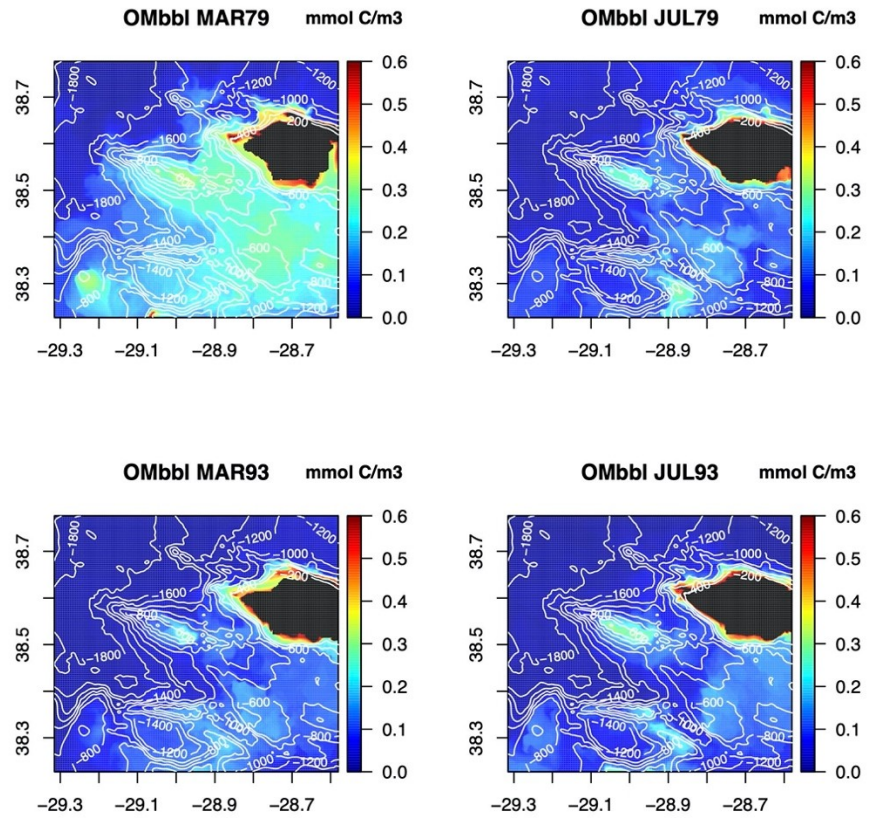

Figure 41: Initial (i.e. Step 1) bottom layer suspended matter concentrations. Contour lines are indicated in white for reference.

The initial suspended OM (median) concentration were used to generate initial conditions for the PSF biomass (Figure 42) and sedimentary OM (not shown for brevity). The carrying capacity of PSF biomass in the model is set to 1,000 mmol C m^{-2}, which means that initial PSF biomass is high throughout the whole model domain, apart from the deepest north-western region. These initial conditions seem to suggest that passive suspension feeders are distributed much more broadly than observations suggest. Below, we show that this situation is considerably different in the output of the fully coupled model.

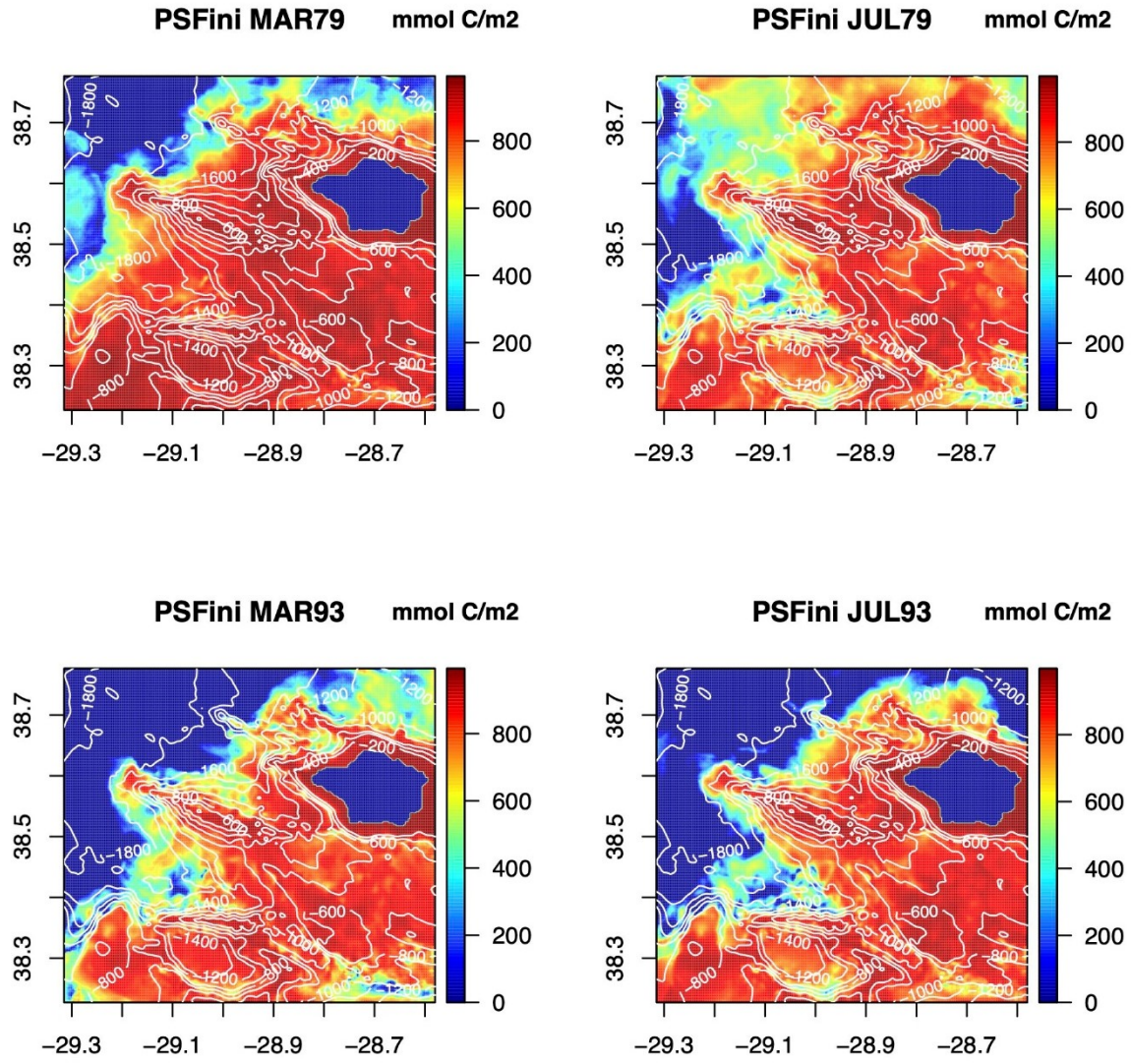

Figure 42: Initial PSF biomass values for the four different periods. White contour lines are indicated for reference.

For the results from the coupled (i.e. step 3) model, we first evaluate the suspended OM matter data in the bottom layer of the model domain (Figure 43). It is striking that the concentrations are substantially lower than the bottom layer concentration from initial (step

1) simulations in which there was no coupling with feeding PSF Figure 41 vs. Figure 43, note also scale differences).

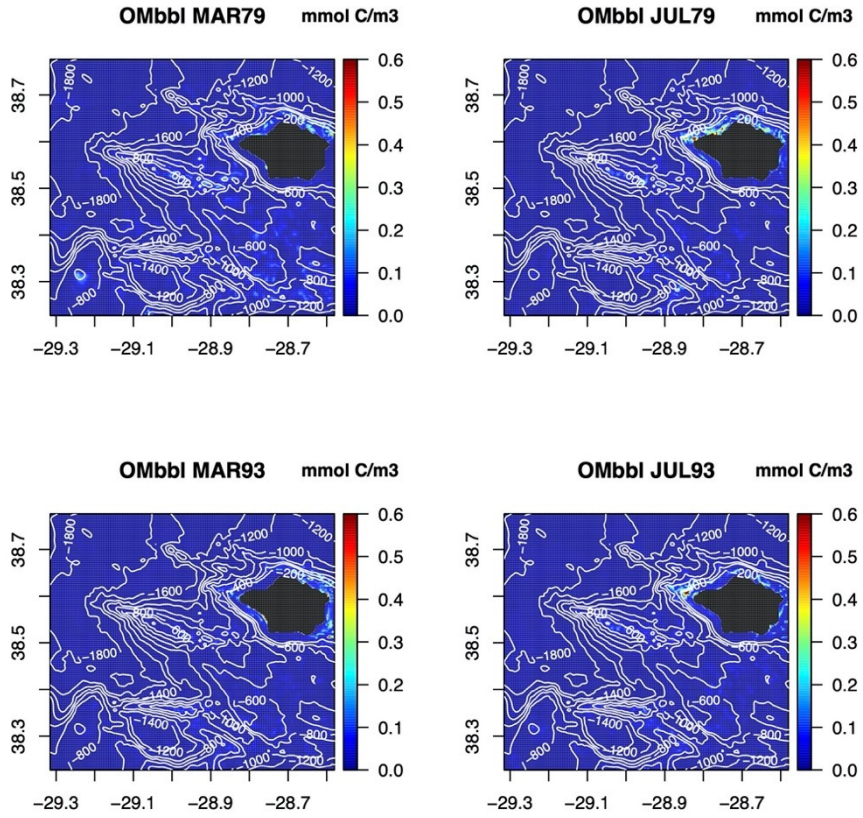

Figure 43: OM concentration in the bottom layer of the coupled model.

The initial PSF biomass is feeding from the suspended OM and depletes the concentration in the bottom layer across the whole model domain close to zero. However, as a result of this depletion, the C uptake by the PSF is insufficient to meet its C demands, which invokes a depletion in PSF biomass over time (compare Figure 42 vs. Figure 44). It was found after that the coupled model simulations ran insufficiently long to reach steady-state, which means that the PSF biomass predictions are over-estimated, especially in the deeper parts of the model domain as this is where the food depletion is strongest. Similar resource depletion in the bottom layer was found for the Rockall Bank case study region (see above) and we conclude that the impact of passive suspension feeders on bottom layer suspended OM concentration extends to large areas of the deep seafloor, even in locations in which natural PSF biomass is low.

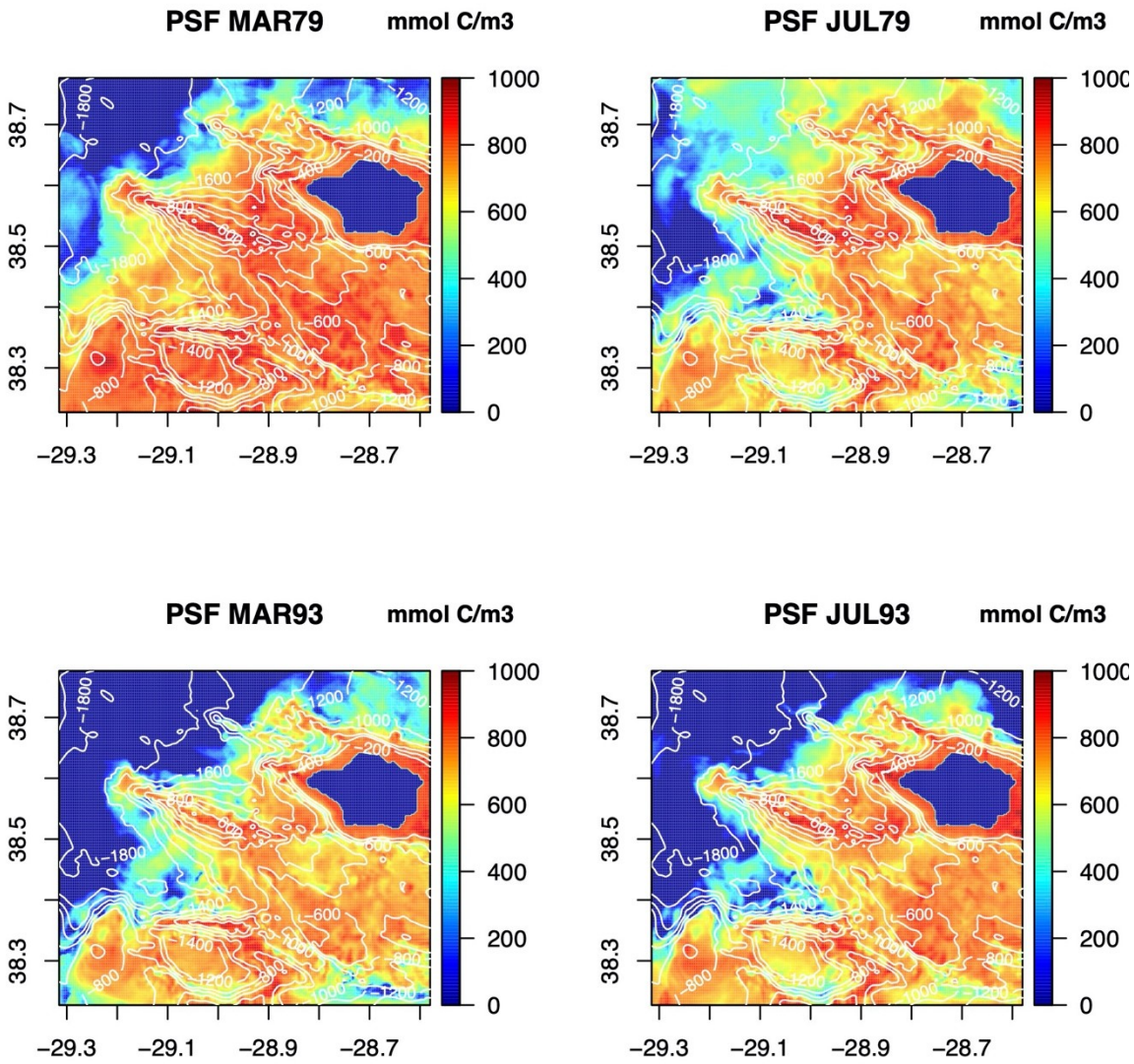

Figure 44: Predicted PSF biomass in the four periods using the coupled model.

As the PSF biomass were not yet in steady state, especially in the deeper parts of the model, we focus on the Condor seamount only, as the inspected time series revealed (data not shown) that the biomass on the summit was approaching steady state and therefore these predictions are can be reasonably evaluated. The PSF biomass is clearly concentrated on the summit of Condor Seamount (Figure 45), which is consistent with camera observations in Tempera (2012) and Deliverable 2.3. While there are differences between periods, the non-steady state situation of the PSF biomass renders it too premature to speculate or conclude on effects of season and/or AMOC state on PSF development.

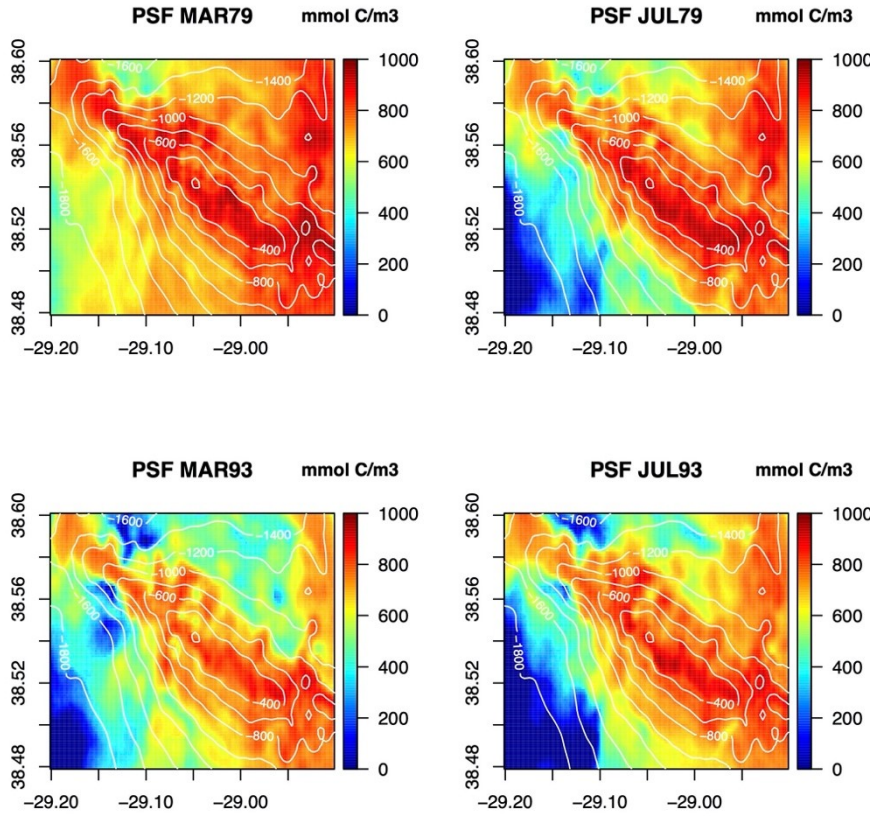

Figure 45: Predicted PSF biomass on the Condor Seamount in the four periods using the coupled model.

Predicted SCOC (Figure 46) and PSF respiration (Figure 47) (both converted from DIC to O_2 using a 1:1 ration between DIC:O_2, Glud (2008)) on the Condor seamount summit are 5-6 mmol O_2 m^{-2} d^{-1} and 3-4 mmol O_2 m^{-2} d^{-1}, respectively. These respiration values are lower but nevertheless surprisingly close to the seafloor respiration measurements that were conducted with the aquatic eddy covariance technique within the ATLAS project (see Deliverable 2.3). During dedicated cruises in the summer of 2018, a total respiration of 8.4 to 15.5 mmol O_2 m^{-2} d^{-1} was measured with a contribution sediment respiration 7.7 mmol O_2 m^{-2} d^{-1}, indicating a "coral garden only" respiration of 1-8 mmol O_2 m^{-2} d^{-1}.

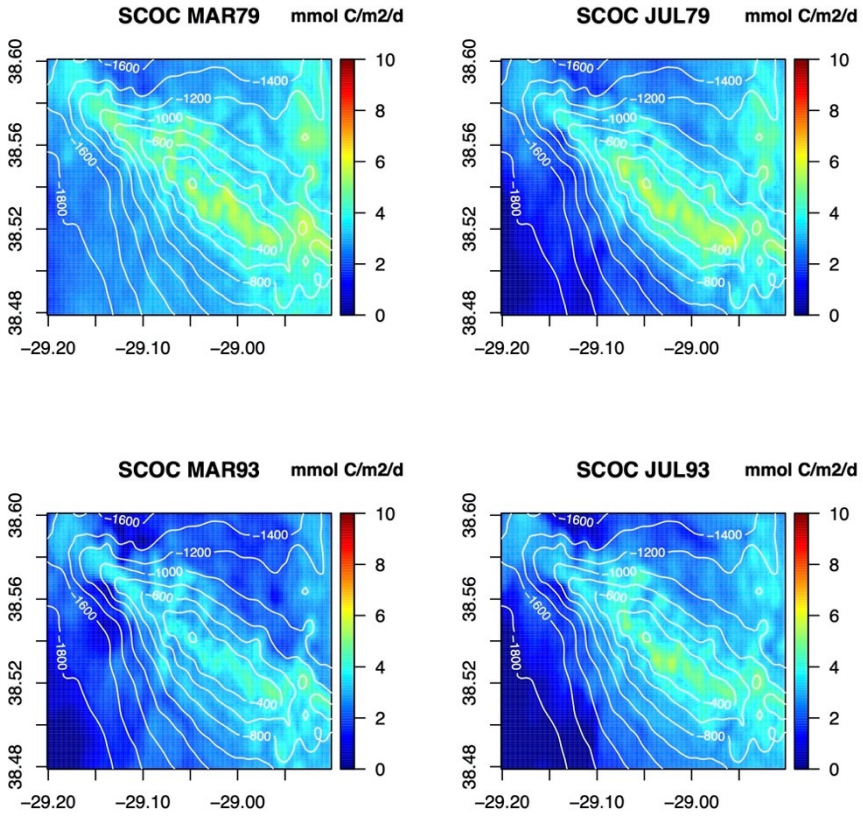

Figure 46: Predicted sediment community oxygen consumption (SCOC) in the four investigated periods with the coupled model.

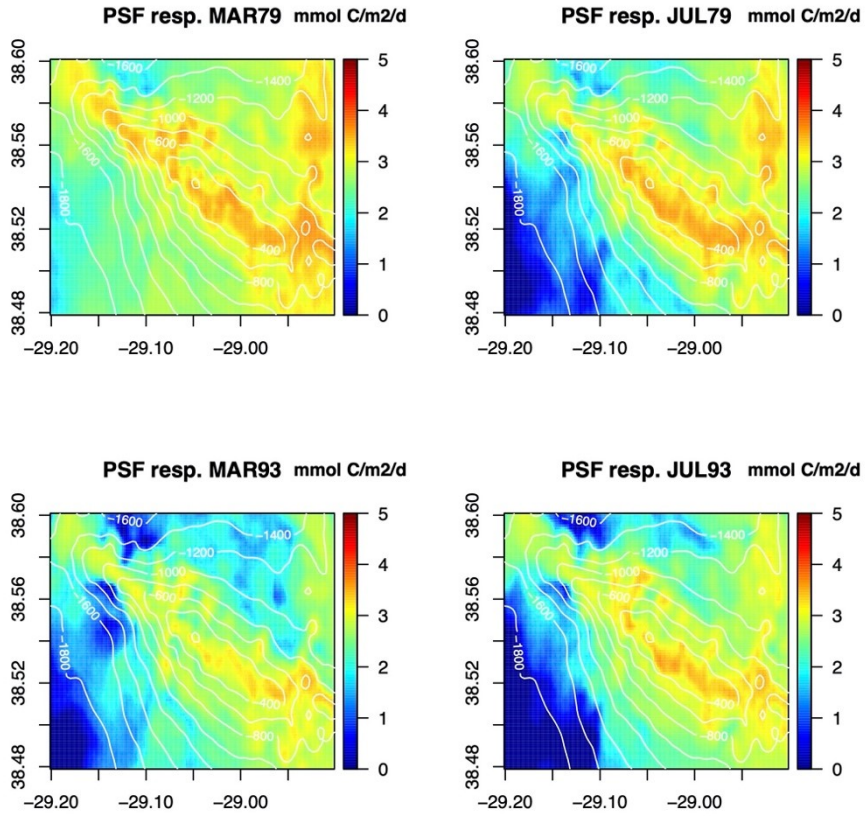

Figure 47: Predicted respiration by PSF in the four investigated periods with the coupled model.

In conclusion, we find that PSF have a substantial impact on the suspended OM concentration in the bottom layer throughout the model domain. This strong feedback between PSF and their resource in the bottom layer poses significant computational challenges, which requires lengthy (several weeks of computation time for a simulated period) simulations. Despite these challenges, the distribution and respiration activity of the passive suspension feeder *Viminella flagellum* was accurately modelled. The coral gardens take advantage of episodic downward pulses of organic matter that are seen above the Condor seamount. The fact that no (dynamic) steady-state was reached does not justify making conclusive statements on effects of season and/or AMOC state on benthic ecosystem dynamics.

6 Davis Strait

6.1 Site description

6.1.1 Bathymetry

The Davis Strait connects the Arctic Ocean in the north via Baffin Bay to the Atlantic Ocean in the south via the Labrador Sea. It is considered the world's largest strait and is renowned for exceptionally strong tides and complex hydrography. The shelves, extending from both Canada and Greenland, include several large shoals or banks typically ranging between 20 and 100 m in depth and traversed by deep troughs. At its narrowest point, a ridge or sill up to approximately 600 m depth extends between Greenland and Baffin Island. The slopes at the Labrador Sea flank of the ridge drop to >2500 m water depth.

The ATLAS case study area is on the Canadian shelf of the Labrador Sea (Figure 48A). The bathymetry shows a shelf of approximately 200-300 m water depth (Figure 48B). The shelf slope is steep, and the water depth rapidly drops to >2,000m. Sponges are found along the shelf break and mostly in the northern sector of the study area, with trawl catches of up to 1.36 kg WW m^{-1} trawl (Figure 48B). Sponge biomass is lower along the southern part of shelf break at ±0.2 kg WW m^{-1} trawl.

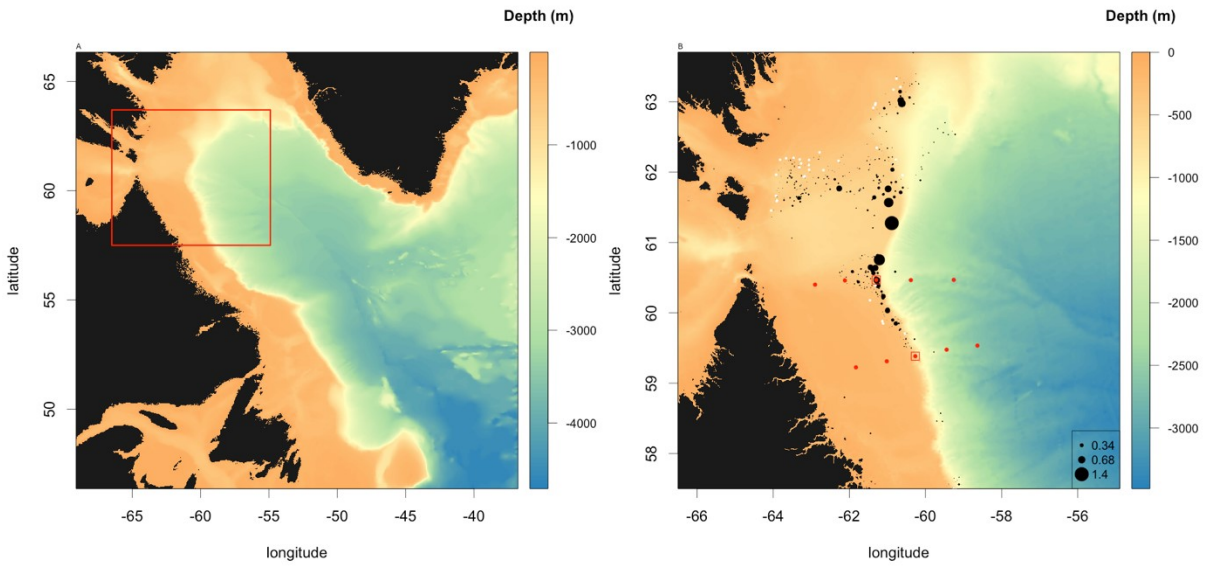

Figure 48: A) Location of the study area (red rectangle) and B) bathymetry of the study area. Black circles are proportional to sponge biomass (kg WW / m trawl) and white circles are trawls with no sponge catch

6.1.2 Hydrography

AMOC transports warm near-surface waters northward and colder deep waters southward, resulting in a large transport of heat. The Labrador Sea in the NW Atlantic is a relevant region for the AMOC, as deep water is formed through the cooling of warm, salty surface waters when it flows counter-clockwise around the west coast of Greenland (Figure 49).

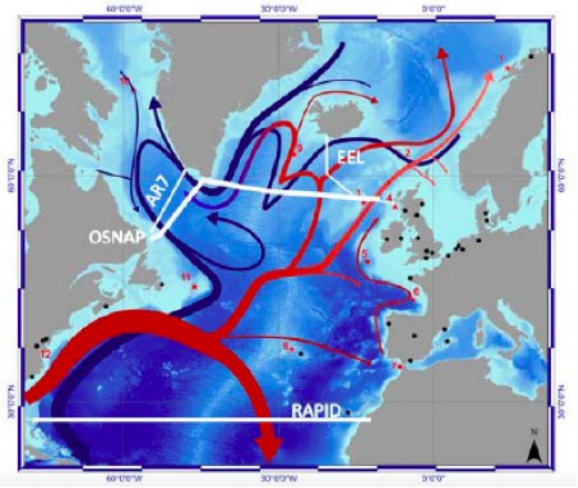

Figure 49: AMOC circulation in the Atlantic Ocean, with the formation of cold deep water in the Labrador Sea in the NW Atlantic.

While there are signatures of substantial water mass modification during deep water formation in the Labrador Sea, recent evidence from the OSNAP array suggests that the Labrador Sea contributes minimally to the overturning circulation and to the variation in overturning strength (Lozier *et al*. 2019). However, an analysis of the VIKING20 output in Deliverable 2.4 shows that changes in the Labrador Sea overturning circulation are correlated with differences in bottom and depth-integrated current velocities between a low AMOC (i.e. 1979) and strong AMOC state (i.e. 1993) (Figure 50).

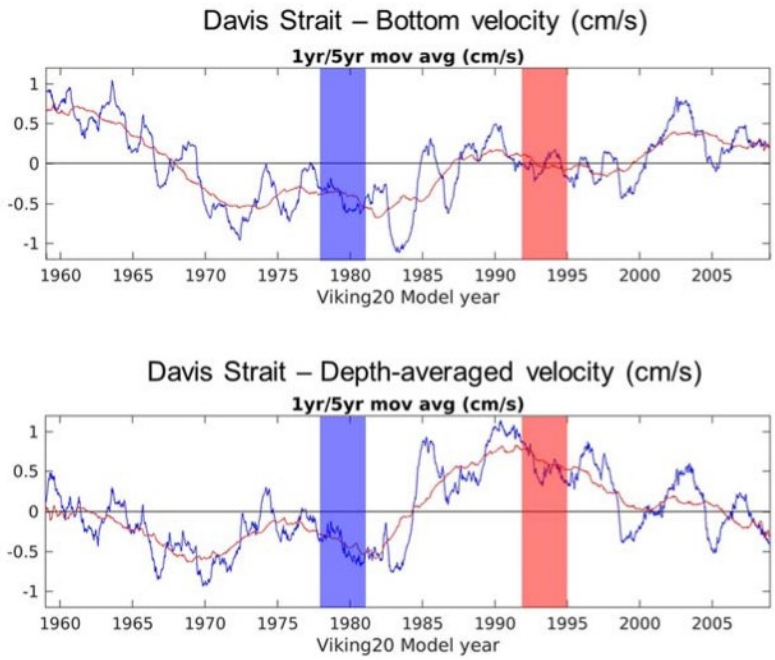

Figure 50: Bottom (top) and depth-averaged (bottom) current velocity anomalies from 1 (blue) and 5 (red) year running means (1958 – 2009) in the Davis Strait case study area. Blue bars indicate periods of weak AMOC and weak Subpolar Gyre index. Red bars indicate periods of strong AMOC and a strong Subpolar Gyre Index.

6.1.3 Sponge grounds

The Northern Davis Strait hosts extensive sponge grounds with up to 2 metric tons of sponge biomass being removed during a single research vessel trawl tow (Kenchington *et al*. 2010). Sponge grounds are internationally recognised as a vulnerable marine ecosystem (VME), prone to physical disturbance by fisheries (e.g. trawling), sediment resuspension and elevated bottom water temperatures (Guihen *et al*. 2012). The ecosystem functions associated with the Davis Strait sponge grounds remain largely unknown as well as the physical and biological conditions that sustain them (Knudby *et al*. 2013). Beazley *et al*. (2015) have recently demonstrated an enhanced biodiversity associated with similar sponge grounds in Flemish Pass to the south. Moreover, deep-water sponges have a high filtering capacity, with a single kg of sponge being capable of filtering 24,000 L d^{-1} (Vogel 1977), suggesting a key role in deep-sea ecosystem functioning (Cathalot *et al*. 2015; Kutti *et al*. 2013; Witte *et al*. 1997).

The occurrence and density of seafloor communities in the Arctic is often related to food availability (Grebmeier *et al*. 2006; Piepenburg *et al*. 1995) and consequently high secondary production at depth is expected in areas where there is an efficient transport of food to the sea floor. Our capacity to predict sponge distribution and functioning is presently dependent on statistical models based on physical and chemical predictors, such as temperature, salinity

and depth. Food is only crudely included as predictor through organic matter export from the mixed layer and/or through its covariation with water depth. Roberts *et al*. (2018) showed for sponges on an Arctic seamount that retention of nutrient-rich water above the seamount and oscillating currents (with diurnal tidal frequency) likely enhances food supply and prevented smothering of the sponges by sedimentation. Interestingly in this respect is that the location of the Spring bloom in Davis Strait does not coincide with the distribution of filter-feeding sponge biomass. While the dominant sponge biomass is found on the shelf ridge, the spring bloom occurs off the shelf to the (north) east. This spatial separation suggests that hydrodynamic transport may be important in coupling of deep-water sponges with surface productivity. Transport mechanisms may include the sinking of denser waters, vertical mixing caused by strong currents, or downwelling that is known to occur for slope areas (Soetaert *et al*. 2016).

We present biomass data below, as kg WW sponge m^{-1} trawled, from a data set uploaded by E. Kenchington to the public ICES database on Vulnerable Marine Ecosystems (http://ecosystemdata.ices.dk/).

6.2 Coupled model development

The coupling between hydrodynamics and food supply was investigated using the coupled model that is developed below.

6.2.1 Calculating the flow fields from VIKING20

The output of the global circulation model VIKING20 was used as hydrodynamic forcing for the transport model of surface-produced organic matter that is subject to biological degradation, in the Davis Strait case study area. We focus amongst others on the difference in organic matter availability between a known sponge-rich and a sponge-poor area in the study area, which were used for lander deployments (see Deliverable 2.3).

To decrease the model resolution and to facilitate the calculation of water and organic matter exchange, the flow fields of the curvilinear model domain of VIKING20 were re-gridded by Christian Mohn onto a rectangular grid. This re-gridding resulted in bathymetry of the whole model domain as shown in Figure 51, which has 231 boxes in the longitudinal direction and 123 boxes in the latitudinal direction and 36 in the vertical.

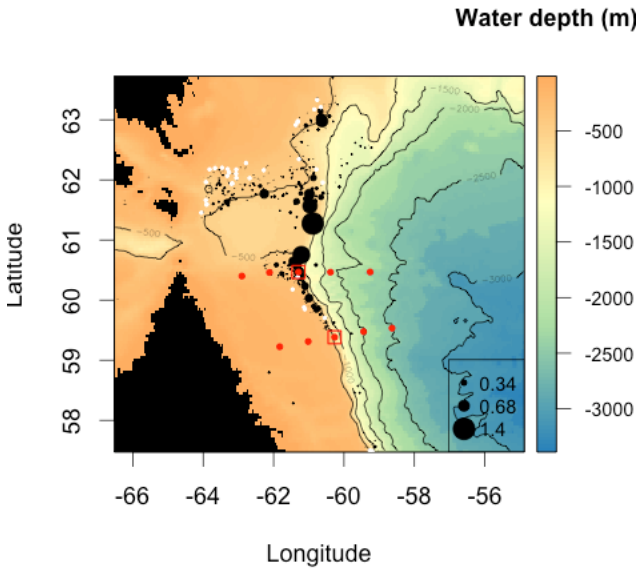

Figure 51: Model bathymetry of the ROMS model. Black circles are proportional to sponge biomass (kg WW / m trawl) and white circles are trawls with no sponge catch. The lander locations (white boxes) and CTD stations (green points) are indicated as well.

The re-gridded horizontal flow fields (*u* and *v* components) are used to calculate the vertical velocities based on a mass balance approach, in which imbalances in the horizontal input/output in each grid box are compensated by positive (upwelling) or negative (downwelling) *w* velocities. For this mass balance approach, the horizontal flows were first mapped onto the boundaries of each grid cell. In other words, the re-gridded VIKING20 output was translated onto a staggered grid by averaging the centralised fluxes onto the grid interfaces. From the current velocity and surface area of each grid cell, the volumetric exchanges between grid cells were calculated. Subsequently, the required compensating up- or downward volumetric exchange could be calculated.

6.2.2 OM suspended matter

The volumetric exchanges, stored at 5-day averages, were used offline to drive organic matter dynamics in the water column, including export of organic matter at the upper boundary, advective horizontal and vertical transport, constant decay and passive sinking. Organic matter in the model is expressed in carbon units (*C*). Following the conservation of momentum, the organic matter reaction model is given by:

$$\frac{\partial H_z C}{\partial t} = \frac{\partial (H_z u C)}{\partial x} + \frac{\partial (H_z v C)}{\partial y} + \frac{\partial (H_z w C)}{\partial z} - w_s \frac{\partial (H_z C)}{\partial z} - k H_z C$$

in which H_z is the grid-cell thickness, w_s is the sinking velocity, and k is the first-order decay rate. Organic matter input into the model domain is represented by the carbon export at the

base of the mixed layer depth (*F0*, mmol C m^{-2} d^{-1}). The specific values chosen for the suspended organic matter parameters in fact defines the type of organic matter we are considering. For example, a high w_s of >100 m d^{-1} is representative of fast sinking organic matter, such as zooplankton faecal pellets or marine snow. After experimenting with the model several times, we decided to run the coupled model with two sets of 'suspended organic matter'. To achieve this, the organic matter parameters were chosen such that each set represented a particular type of organic matter. The first set was representative of labile (i.e. high k) and comparatively fast sinking (i.e. high w_s) organic matter. As we detail below in section 6.4, Results and Discussion, the concentration of this labile type of organic matter in the bottom boundary layer proves (grossly) insufficient to meet the C-demands of the active suspension feeder *G. barretti*. In itself, this is an interesting finding, which will be discussed below. We however, also continued to identify an organic matter type, by varying the 'suspended organic matter' parameter settings that would result in a sufficiently high organic matter concentration in the bottom boundary layer to allow sponge growth. Here we define both 'suspended organic matter' parameter sets.

The first parameter set is representative of labile and comparatively fast sinking organic matter (i.e. fOM). Henson *et al*. (2015) provides a model analysis of the carbon export and export efficiency in the ocean. With a primary production of ~600 mg C m^{-2} d^{-1} and an export efficiency of 30%, characteristic for northern regions, the export of fOM was set to 175 mgC m^{-2} d^{-1} (equivalent to 14.6 mmol C m^{-2} d^{-1}). This value is similar to the sinking flux that (Tian *et al*. 2004) report for spring conditions based on a 1D-numerical modelling study on OM export in the Labrador Sea. Like for the Condor seamount model, the degradation rate of sinking organic matter is based on the formulation used in the MEDUSA model framework, which is defined as $k = 0.016 \times 1.066^T$ (Henson *et al*. 2015; Yool *et al*. 2011), in which T is temperature in ^oC. The average bottom temperature is $\pm 4^0$C (VIKING20 output, confirmed with the ATLAS lander deployments, see Deliverable 2.3), which gives a *k* of 0.02 d^{-1}. The sinking velocity of organic matter ranges vastly from negligible to hundreds of m d^{-1} (Alldredge & Silver 1988; Trull *et al*. 2008). Tian *et al*. (2000) adopted a sinking velocity of 100 m d^{-1} for fast sinking organic matter and assumed no sinking for other organic matter sources. We set the sinking rate (w_s) slightly lower to 40 m d^{-1} to represent a broader organic matter spectrum. This value is also more consistent to the parameterization of sinking particles in the MEDUSA model (Henson *et al*. 2015).

The second parameter set is representative of less labile and slow-sinking organic matter (i.e. *sOM*). Tian *et al*. (2000) concluded from their 1D-modelling study that DOC is mostly degraded in the surface mixed layer and that carbon transport towards deep waters takes place essentially via sinking of large particles. Here, we consider the dynamics of this slow-sinking and more refractory pool of organic matter. Riley *et al*. (2012) observed marine snow dynamics at the Porcupine Abyssal Plain with an instrument designed specifically to catch various pools of marine snow and they observed that the export flux at the bottom of the mixed layer depth (~50 m at the time of sampling) was dominated by slow-sinking (<10 m d^{-1}) marine snow. Moreover, depth profiles of DOC in the southern Labrador Sea show a sharp decrease in the surface ocean, but also a comparatively large pool of DOC (~60 µM) down to 3,000m water depth (Tian *et al*. 2004). Deep-sea sponges, and particularly *G. barretti* (Leys *et al*. 2018), is known for its capacity to utilize the DOM pool at these concentrations (S. Maier, unpub. data). The density of bacteria, another well-known resource for deep-sea sponges, decreases exponentially with water depth to concentrations of <0.25 µM, suggesting this is quantitively not an important food source. We decided to focus on impact of a difference in detritus characteristics, so for *sOM* the export flux (*F0*) was kept identical to that set for *fOM*, but the sinking velocity was decreased to 0.1 m d^{-1} and the degradation rate *k* was set to 0.002 d^{-1}.

6.2.3 Active suspension feeders

The model description for sponges is comparable to that of passive suspension feeders, as described in the sections for Rockall Bank and Condor Seamount, with the crucial difference that the uptake of organic matter is not dependent on the ambient bottom velocity, as active filter feeders create their own flow with active pumping behavior. Hence,

$$\frac{dASF}{dt} = AE_{ASF} \cdot NGE_{ASF} \cdot FR_{ASF} \cdot OM_{bbl} \cdot ASF \cdot \left(1 - \frac{ASF}{CC_{ASF}}\right) - m_{ASF} \cdot ASF$$

in which *ASF* is the sponge biomass (mmol C m^{-2}), AE_{ASF} is the assimilation efficiency (-), NGE_{ASF} is the net growth efficiency (-), FR_{ASF} is the biomass-specific filtration rate (m^3 mmol C^{-1} d^{-1}), OM_{bbl} is the suspended organic matter concentration in the benthic boundary layer (mmol C m^{-3}) and CC_{ASF} is the carrying capacity of the sponge ground (mmol C m^{-2}).

The sponge *G. barretti* is an active suspension feeder and the dominant component of the benthic community at Davis Strait (Knudby *et al*. 2013). For this species, a comparatively high

amount of data are available in the literature (Deliverable 2.1). The assimilation efficiency (AE_{ASF}) is set to 0.80, as assimilation efficiency of sponges is typically high (Leys *et al*. 2011). Few data exist on the net growth efficiency for (deep-water) sponges. Van Oevelen *et al*. (2018) found a low growth efficiency (6 - 11%) for the coral-associated sponge *Hymedesmia coriacea*, which is similar to Koopmans *et al*. (2010) who report a growth efficiency of 10% for *Haliclona oculata*, while Thomassen and Rissgard (1995) report a growth efficiency of ~30% for the shallow water sponge *Halichondria panicea*. In all, a net growth efficiency of 25% was selected from this range.

The filtration rate (FR_{ASF}) is based on the filtration rate of 347 L kg^{-1} WW d^{-1} found through *in situ* pumping rate measurements of *G. barretti* (Leys *et al*. 2018). These pumping rates are surprisingly similar to those found by (Kutti *et al*. 2013), who found a range of 260 to 600 L kg^{-1} WW d^{-1} through field and lab experiments, respectively. The filtration rate of 347 L kg^{-1} WW d^{-1} converts to $5.0x10^{-5}$ m^3 $mmolC^{-1}$ d^{-1} with the conversion factors of 1/6 kgDW/kgWW, 1/2 kgC/kgDW. The maintenance respiration rate for ASF (m_{ASF}) is set to be 25% (i.e. NGE) of the total respiration of 7.68 µmol O_2 g^{-1} WW d^{-1} as measured for *Geodia* sp. (Kutti *et al*. 2013; Leys *et al*. 2018), which translates to a maintenance respiration of $2.76x10^{-4}$ d^{-1}. Finally, the carrying capacity is set to 30,000 mmol C m^{-2}, which is the maximum biomass during in extensive trawling surveys in Davis Strait.

Based on the above model, it is comparatively easy to calculate the steady-state energy balance of *ASF* under a range of suspended organic matter concentration OM_{bbl}. After setting $\frac{dASF}{dt} = 0$ and re-arranging, we obtain the following relationship between the physiological parameters and the energy balance:

$$\frac{ASF}{CC_{ASF}} = 1 - \frac{m_{ASF}}{AE_{ASF} \cdot NGE_{ASF} \cdot FR_{ASF} \cdot OM_{bbl}}$$

in which $\frac{ASF}{CC_{ASF}}$ is the realised fraction of the carrying capacity. Note that when the acquisition of resources ($AE_{ASF} \cdot NGE_{ASF} \cdot FR_{ASF} \cdot OM_{bbl}$) is lower than the maintenance respiration m_{ASF}, the relation becomes negative and no sponge biomass can be sustained. The resulting relation, plotted as a function of the OM_{bbl}, is shown in Figure 52.

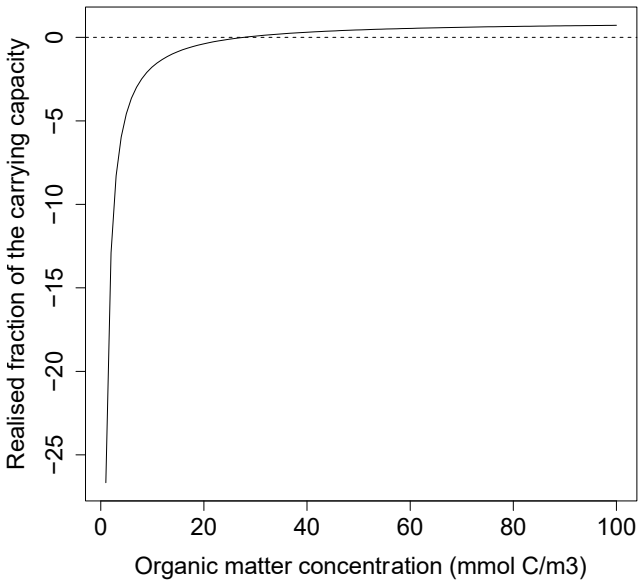

Figure 52: Realised fraction of the carrying capacity as a function of the suspended organic matter concentration in the benthic boundary layer.

The transition from negative to positive sponge growth (i.e. food acquisition = respiration) is found at an OM_{bbl} of 28 mmol C m^{-3}. This value means that positive sponge growth is only possible above these OM concentration thresholds. This relation and threshold value will be used in the Results and Discussion below.

6.2.4 Sediment organic matter

The sediment biogeochemistry is modelled simply a single sedimentary organic matter pool, which is fuelled by deposition from the water column and input of non-assimilated food from the passive and active suspension feeders and is degraded following first-order dynamics:

$$\frac{dOM_{sed}}{dt} = \omega \cdot OM_{sus} + (1 - AE_{PSF}) \cdot PSFing + (1 - AE_{ASF}) \cdot ASFing - k_{sed} \cdot OM_{sed}$$

The sedimentary degradation rate is set to 0.041 d-1 (equivalent to 15 y^{-1}), which characteristic for degradation of fresh organic matter (Westrich & Berner 1984).

6.3 Three-step solution to solve the coupled model

The coupled model was solved for the weak (1979) and strong AMOC (1993) state. Note that the organic matter input (*F0*) at the surface was set to a single flux, thus assuming no temporal or spatial variation. This was done in order to obtain a faster steady-state and to investigate the impact of location within the model domain and AMOC on food availability and sponge biomass. In step 1, the initial conditions for the suspended organic matter concentration were calculated. The suspended organic matter concentration was calculated from a simple

exponential decay function and then subjected to the hydrodynamic forcing of a full year. The median suspended organic matter concentration of the last 100 days of the annual simulation was stored as initial condition for the suspended organic matter. In step 2, the initial condition for the biomass of ASF and sediment organic matter throughout the model domain was calculated. For this, the suspended organic matter concentration (output of step 1) in the bottom layer was used to calculate the equilibrium biomass and sediment organic matter concentration. In step 3, we ran the coupled model by taking the initial suspended organic matter concentration (step 1), initial biomass of ASFs (step 2) and sediment organic matter concentration (step 2) and running the model for a full year to arrive at a (dynamic) equilibrium state of the organic matter concentration in the water column, biomass of ASFs and sediment organic matter.

6.4 Results and Discussion

6.4.1 Hydrography of the Davis Strait case study area

We first use the re-gridded VIKING20 model output to visualise the seasonal (winter: Jan-Mar, spring: Apr-Jun, summer: Jul-Sep, autumn: Oct-Dec) changes in temperature, salinity and in surface, bottom and vertical current velocities for both years, which will be based on the basin-wide hydrography. A more comprehensive comparison between the AMOC states is detailed below, where we will zoom in on two lander locations in, respectively, a high-sponge location in the north and a low-sponge location in the south.

The seasonal average surface temperature (Figure 53) and salinity (Figure 54) show a pronounced seasonal cycle. Temperate in the study area ranges from -2 to 9^{o}C, with relatively low temperatures on the shelf and higher temperatures off the shelf. In both years, winter and spring temperatures are evidently lower throughout the whole model domain, while in summer and autumn temperatures are comparatively higher. Water temperature on the shelf, especially closer to the coast, is higher in summer. Sea surface salinity shows a gradient of higher salinity water in the eastern domain and low salinity water in the western part of the model domain. In especially summer, intrusion of fresh (melt) water through the southern area of the Hudson Strait in the west of the model domain is evident.

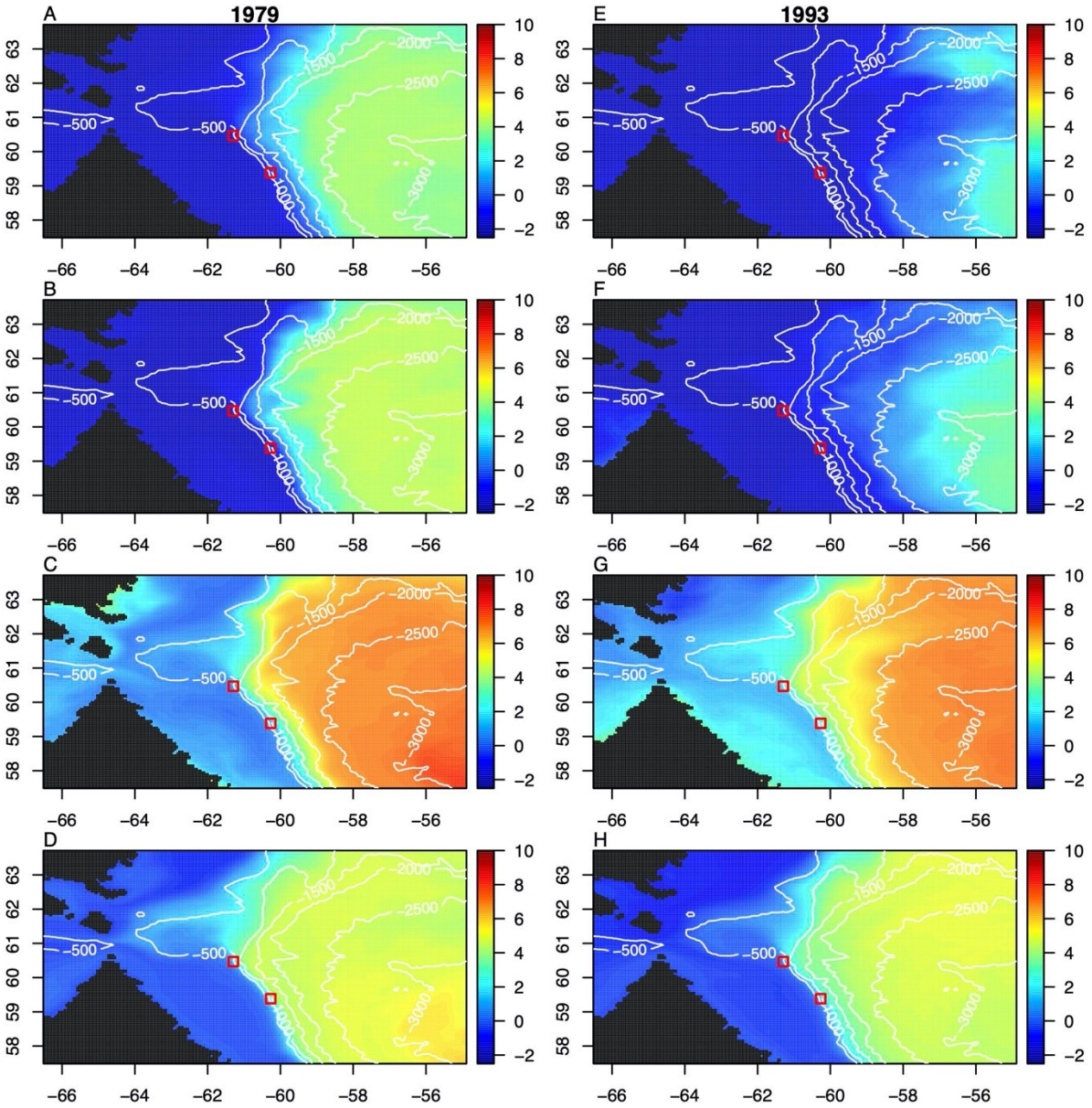

Figure 53: VIKING20 derived sea surface temperature (^{0}C) for the four seasons in 1979 (A-D) and 1993 (E-H). White lines indicate depth contours. Lander positions are indicated by red squares for reference.

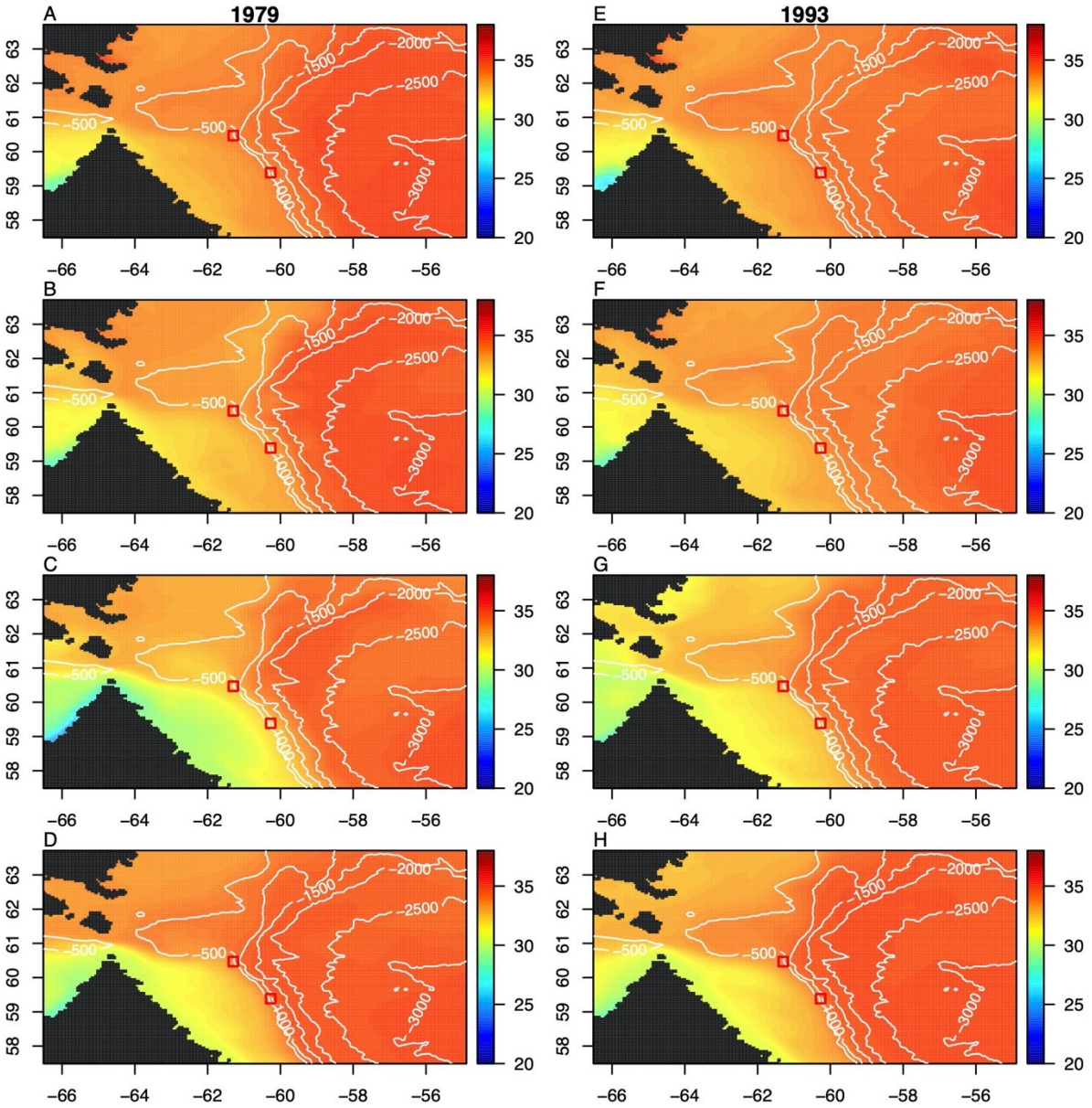

Figure 54: VIKING20 derived salinity for the four seasons in 1979 (A-D) and 1993 (E-H). White lines indicate depth contours. Lander positions are indicated by red squares for reference.

Seasonally averaged surface currents in both 1979 and 1993 show a counter clockwise circulation pattern, which is consistent with the known circulation pattern of the Labrador Sea. Strongest currents (1.08 m s^{-1}) follow the shelf break between the 500 - 1,000 m depth contours (Figure 55). On the shelf, the surface currents are smaller than along the shelf break but follow the flank of the seafloor depression in the northern part of the model domain. Current velocities are reduced inside this depression. In addition, outflow from the Hudson Strait is evident in the summer and autumn quiver plots.

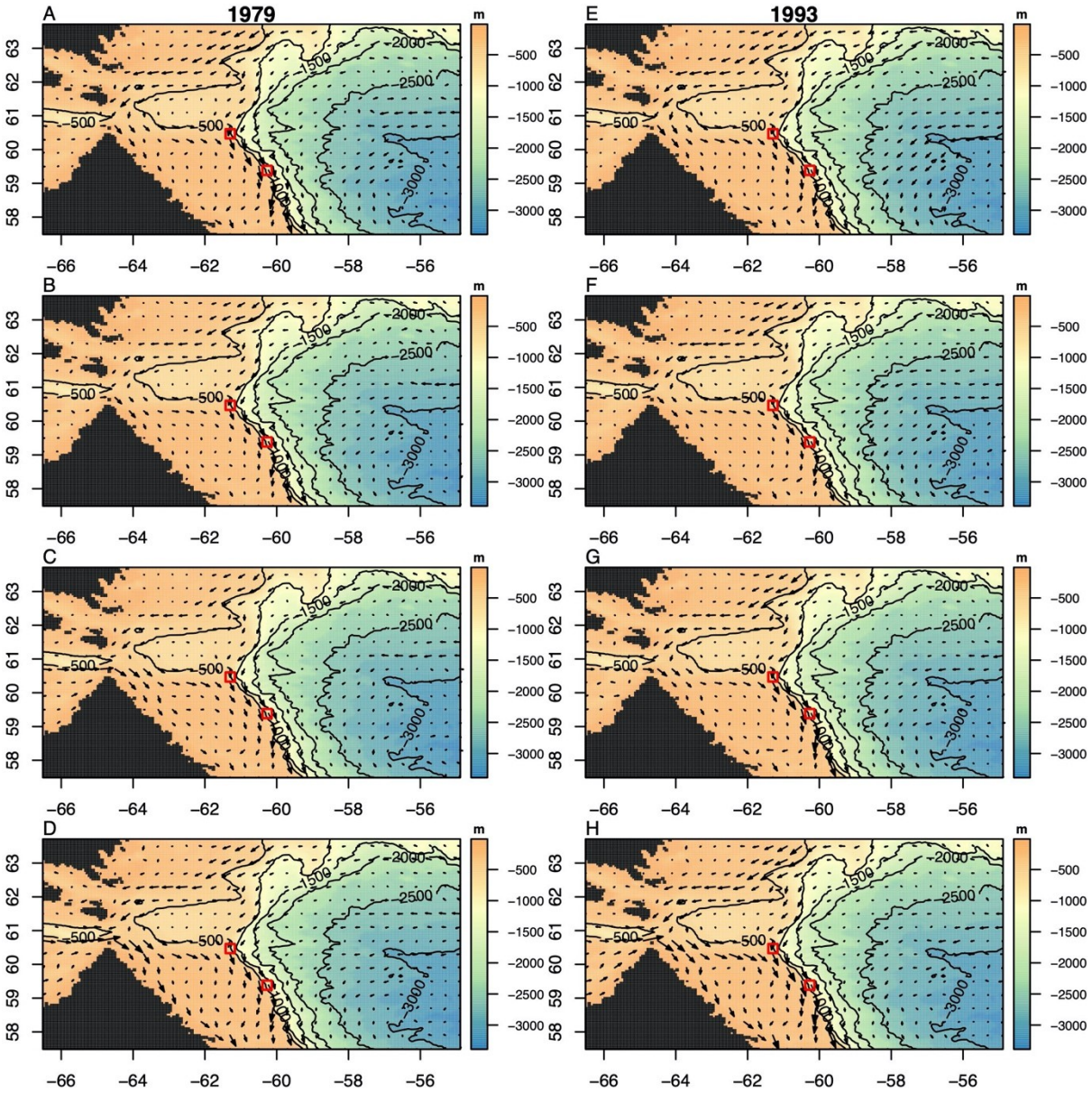

Figure 55: Quiver plots of the surface current velocity (m s^{-1}), based on the re-gridded VIKING20 output, for the four seasons in 1979 (A-D) and 1993 (E-H). Maximum arrow size corresponds to a current velocity of 1.1 m s^{-1}. Black lines indicate depth contours.

Vertical current velocities at 100 m water depth (i.e. below or lower in the mixed layer depth) in the model domain shows a broad range from -0.03 to 0.03 m s^{-1} across both years and the whole model domain (Figure 56), although most vertical velocities range from -0.01 to 0.01 m s^{-1} with a slight dominance of negative (i.e. downward) velocities (Figure 57). Upward velocities are concentrated in the deeper parts of the model domain in the southeast along the 2,500 and 3,000~m depth contours) and along the deeper shelf break along 1,500 m depth contour. Downward velocities are most prominent and strongest along the upper shelf break at the 500-m depth contour, roughly corresponding to the depth of the lander deployments.

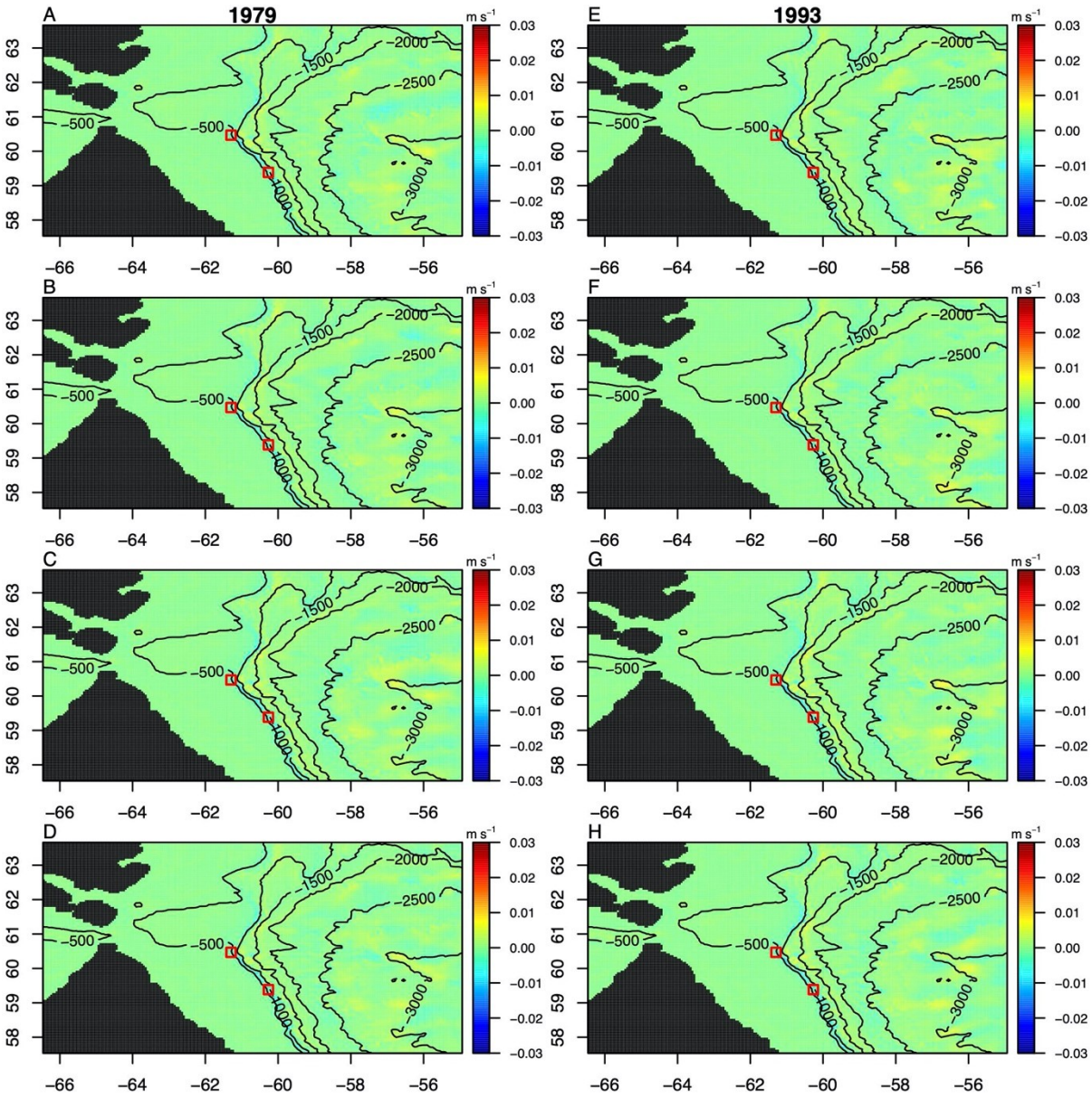

Figure 56: Vertical velocity (m s^{-1}) at 100 m water depth in the model domain of the four seasons in 1979 (A-D) and 1993 (E-H). Upward velocities are defined positive and downward velocities are negative. Black lines indicate depth contours. Lander positions are indicated by red squares for reference.

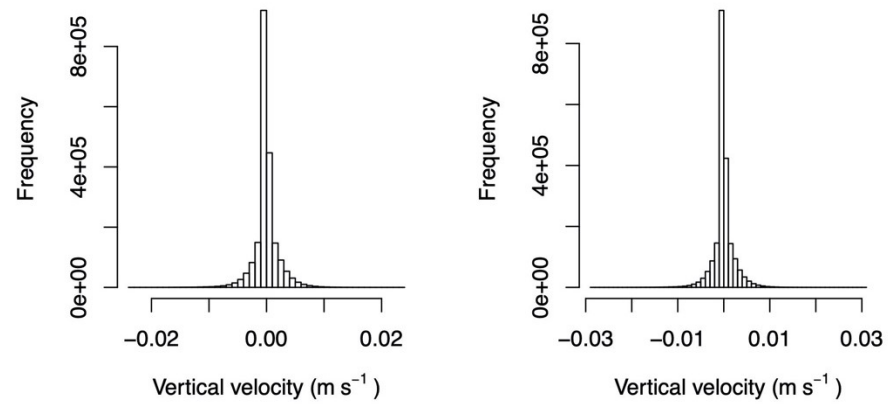

Figure 57: Boxplots of the vertical velocities at 100 m water depth in the model domain for 1979 (left) and 1993 (right). Upward velocities are defined positive and downward velocities are negative.

6.4.2 Hydrography of the lander locations in Davis Strait

After visualising and describing the region-wide hydrographic patterns, we now zoom in on the shelf break transects and respective lander locations to explore the hydrographic differences between the two AMOC states. The lander locations and CTD transects visited during the Amundsen 2018 cruise (see also Deliverable 2.3) that will be explored in this section are presented in Figure 58.

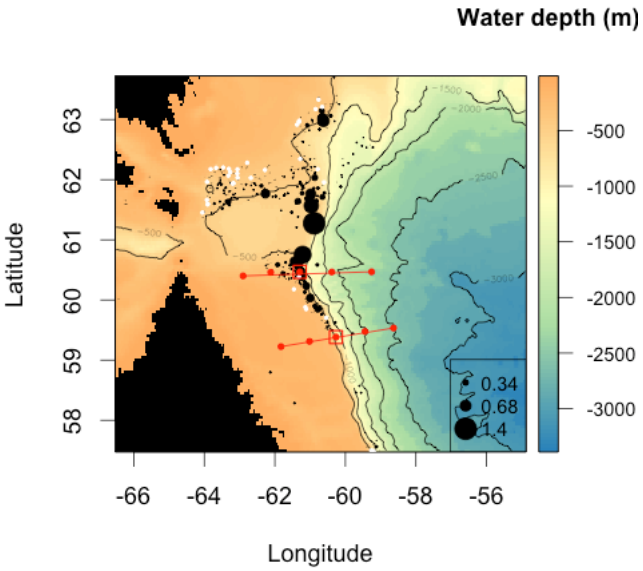

Figure 58: CTD transects (with centre stations being the lander locations) in the high sponge (northern transect) and low sponge (southern transect) transects. Sponge biomass (kg WW m^{-1} trawl) are indicated by black circles, while white circles indicate trawls with no sponge catch.

Figure 59 shows the temperature difference between the weak and strong AMOC years across the two transects. Evidently, surface waters were warmer in 1979 but temperature differences are minor at depth with a 0-1 °C higher temperature in 1979 as opposed to 1993.

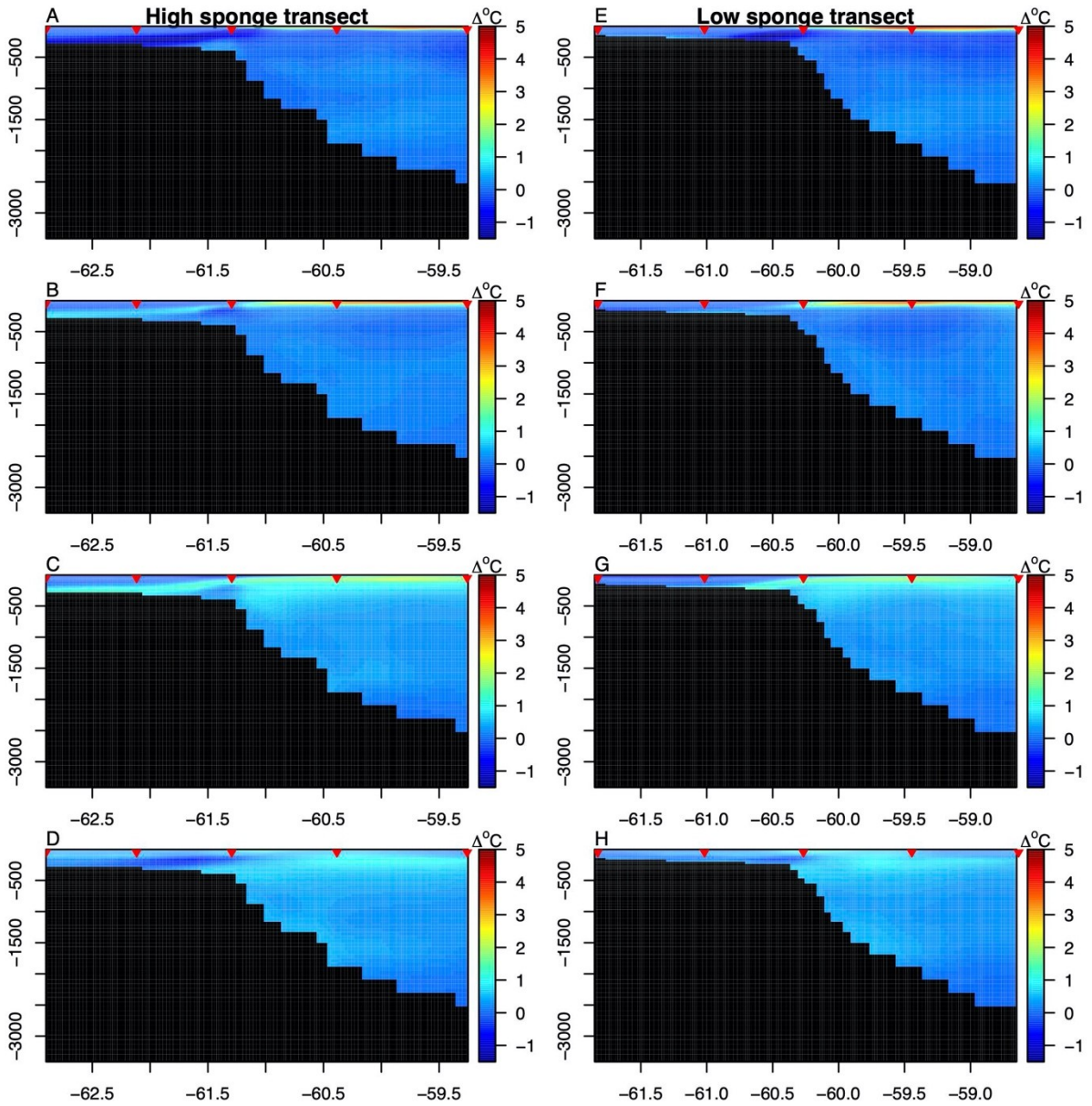

Figure 59: Temperature differences (i.e. 1979 minus 1993) of the four seasons along the High sponge (A-D) and Low sponge (E-H) transects. Red marks indicate the CTD stations.

The bottom velocities at the high sponge lander site are slightly higher than at the low sponge lander site (Figure 60), but differences between AMOC states are negligible. The vertical velocities (at 100 m water above the lander sites) are more negative (i.e. stronger downward transport) above the lander site at the high sponge lander site as opposed to the low sponge

lander site (Figure 61), but similar as with the bottom velocities, vertical velocities between AMOC states are negligible.

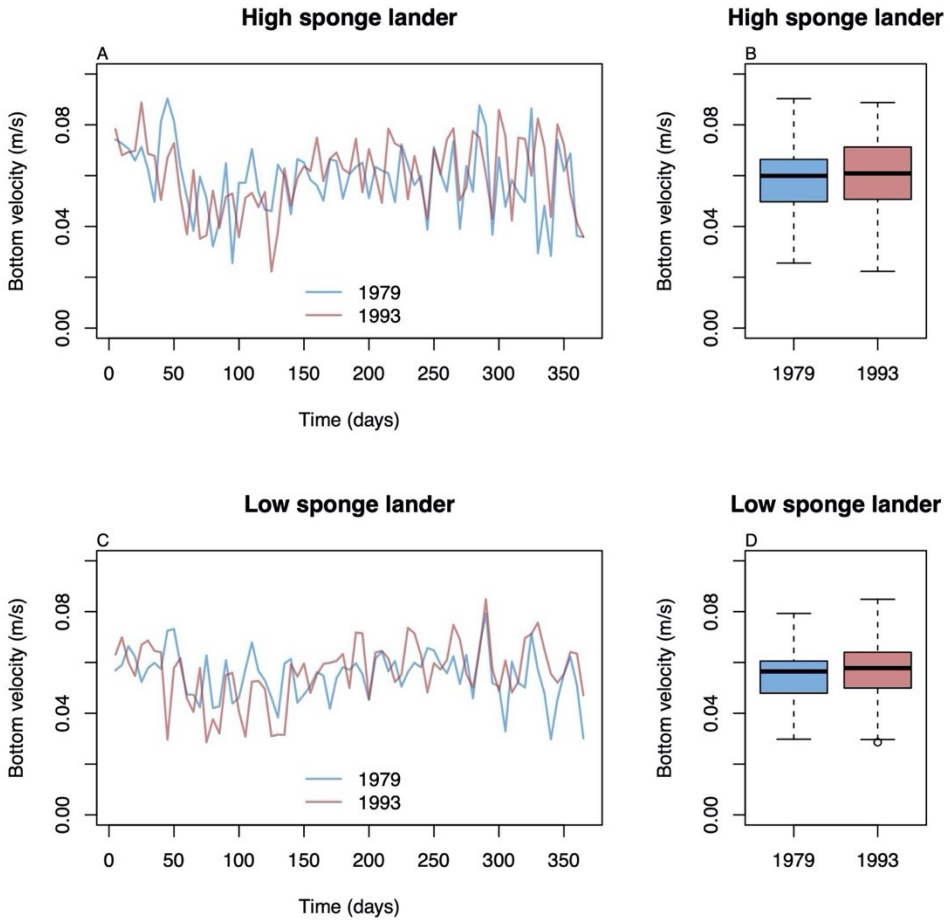

Figure 60: Bottom velocity throughout the year for the high sponge lander site (A, B) and low sponge lander site (C, D).

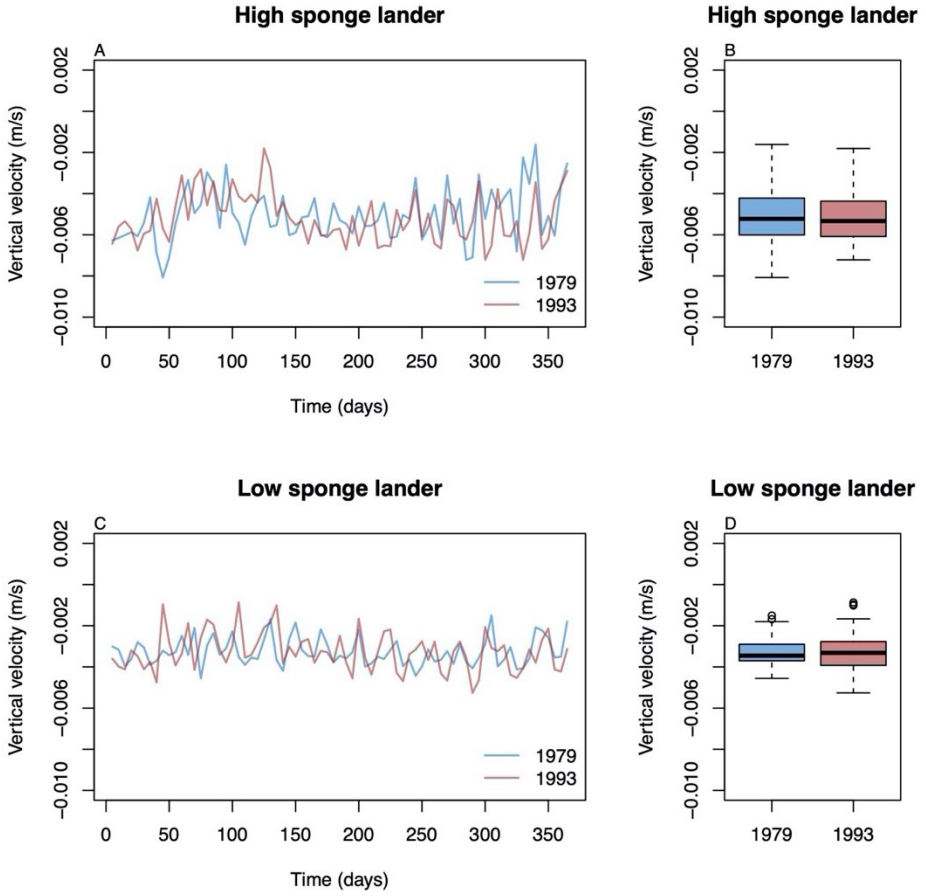

Figure 61: Vertical velocity (100m water depth) throughout the year for the high sponge lander site (A, B) and low sponge lander site (C, D).

Small differences in bottom velocity and vertical velocity were found between the lander locations, but differences for a location between AMOC states were not evident. The consequences of these differences for organic matter availability at the seafloor will be discussed next based on the coupled modelling results.

6.4.3 Coupled model results on suspended organic matter, coral biomass and respiration

Step 1 was first performed with the parameter set 'fOM', which represents suspended organic matter that is labile and fast-sinking. After Step 1, i.e. the median suspended organic matter initialization step, the labile organic matter concentration (*fOM*) in the bottom layer of the model in 1979 ranges from 0.05 to 0.35 mmol C m^{-3} (Figure 62). There is a clear positive correlation between bottom depth and the *fOM* concentrations, but the deep south-eastern part of the model domain seems to receive a higher contribution of *fOM* that can be expected from water depth alone.

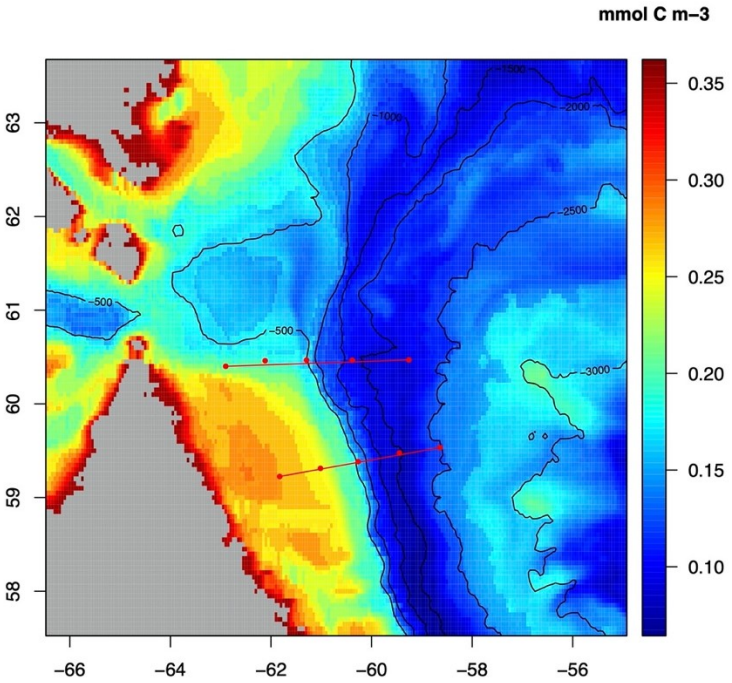

Figure 62: The median organic matter concentration (parameter settings 'fOM') in the bottom layer of 1979 for the whole model domain. The red lines indicate the High sponge transect (northern) and Low sponge transect (southern). The red marks indicate the respective CTD stations, with the central station representing the lander locations.

Figure 63 shows the suspended organic matter concentration at the 'High sponge' (left) and 'Low sponge' (right) transects. Also here is it evident that the suspended organic matter concentration broadly correlates with water depth, the continental slope has elevated *fOM* concentration. This enhanced OM availability can be explained by the negative vertical velocities that occur along the continental slope (Figure 56).

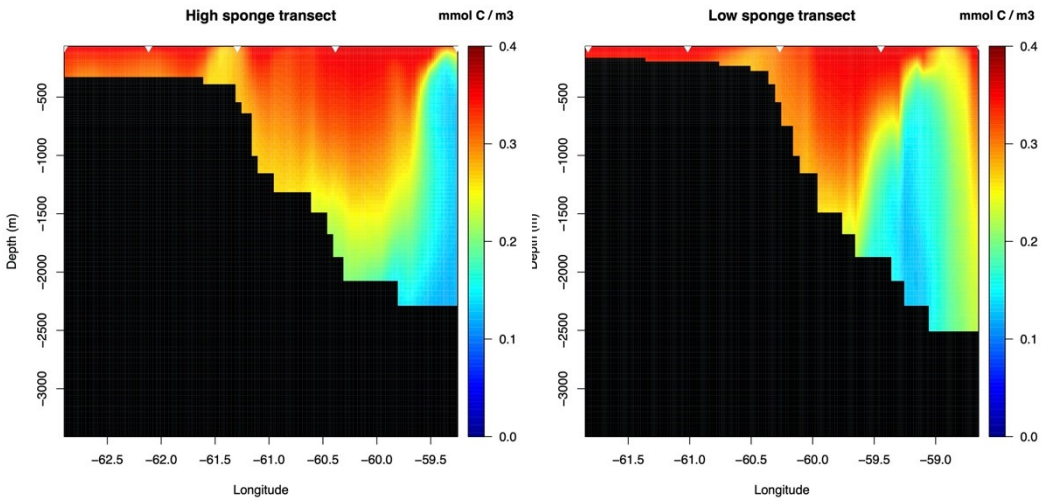

Figure 63: The organic matter concentration (parameter settings 'fOM') across the high (left) and low (right) sponge transects. The white marks indicate the CTD stations, with the central station representing the lander locations.

The most important finding is however that the *fOM* concentration in the bottom layer in the whole model domain is <0.4 mmol C m^{-3}. Above in the section 6.2.3: Active suspension feeders, we concluded that the minimum OM concentration to allow sponge sustenance is 28 mmol C m^{-3}. The predicted *fOM* concentration is hence grossly insufficient to allow positive sponge growth. Results for the organic matter distribution in 1993 are broadly comparable (data not shown), implying that growth of the active suspension feeder *G. barretti* is also not possible in 1993. Hence, for *fOM* it is not AMOC state or season that causes differences in sponge growth. Instead, the characteristics of the organic matter that we imposed render a too low OM concentration at the seafloor for active suspension feeders to grow. This is in agreement with results from feeding studies of sponges. Leys *et al*. (2018) found that the concentration of bacteria and particulate organic matter was insufficient to meet the metabolic demands of *G. barretti* and they attributed the difference to feeding on dissolved organic matter. Similarly, Kahn *et al*. (2015) measured *in situ* carbon and nitrogen fluxes of the glass sponge *Aphrocallistes vastus* in the north-eastern Pacific and calculated the energetics of feeding for all reefs in the Strait of Georgia, British Columbia. These sponge reefs extracted seven times more carbon than can be supported by a 1D-vertical flux of total carbon alone.

As the flux and concentration of *fOM* appears insufficient to sustain sponge growth, we experimented with the model whether more refractory organic matter (*sOM*) may reach a sufficiently high concentration in the bottom layer to allow sponge growth. The initial sOM

concentration (Step 1 output) in the bottom layer in shown in Figure 64 and the “High sponge” and “Low sponge” transects are shown in Figure 65.

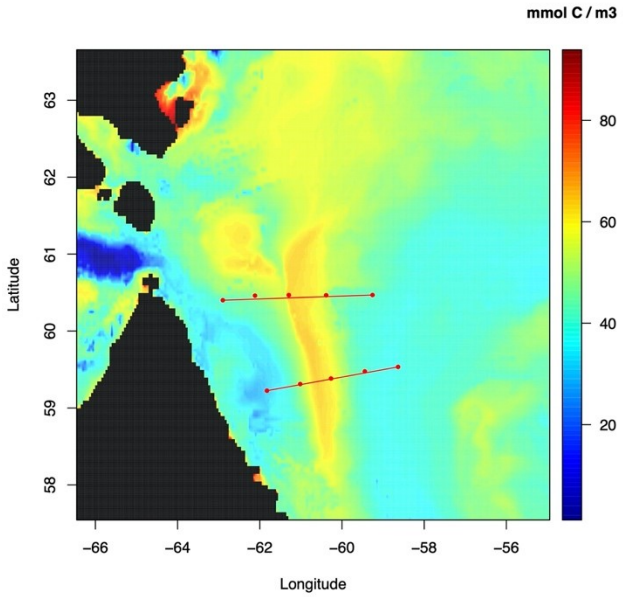

Figure 64: The median organic matter concentration (parameter settings 'sOM') in the bottom layer of 1979 for the whole model domain. The red lines indicate the High sponge transect (northern) and Low sponge transect (southern). The red marks indicate the respective CTD stations, with the central station representing the lander locations.

The differences in concentration of *sOM* versus *fOM* in the model domain are striking, with the concentration of *fOM* being limited to <0.35 mmol m^{-3}, *sOM* reaches a concentration of >60 mmol C m^{-3}. The concentration of *sOM* is above the sustenance threshold of 28 mmol C m^{-3} for ASF. This is an important finding of the modelling approach, as ASF apparently cannot maintain growth on typical labile and comparatively fast sinking organic matter as the ambient concentration is insufficient. Moreover, the distribution of *sOM* is also strikingly different from *fOM*. While the concentration of *fOM* is closely correlated with bottom depth and has highest concentrations along the coast, the concentration of *sOM* at the seafloor is much more closely linked to the shelf ridge and slope where the sponges are found. The *sOM* concentration is slightly higher at the seafloor and extends further down the shelf along the High sponge transect as opposed to the Low sponge transect. Note that we here show only the results of 1979 to preserve space but results of 1993 are broadly comparable.

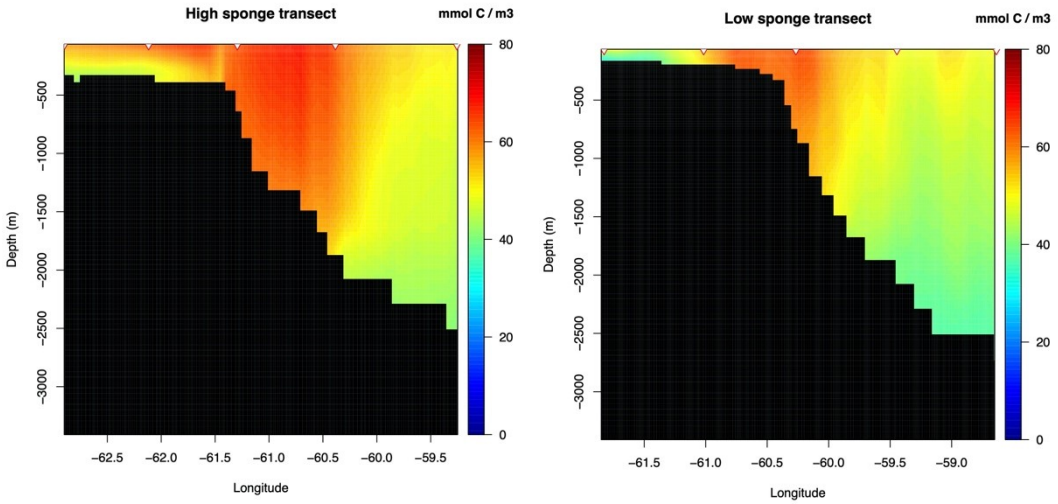

Figure 65: The median organic matter (sOM) concentration along the High sponge (left) and Low sponge (right) transect. The white marks indicate the CTD stations, with the central station representing the lander locations.

The initial *sOM* concentration (Figure 64 and Figure 65) was used to calculate the initial biomass of ASF and OMsed (Step 2) in the model domain, which are shown in Figure 66 (left) and Figure 66 (right), respectively. Again, only the results of 1979 are shown to preserve space, but results of 1993 are broadly comparable. The initial *sOM*, ASF and OMsed values are used in the final modelling step 3 of which results are shown below.

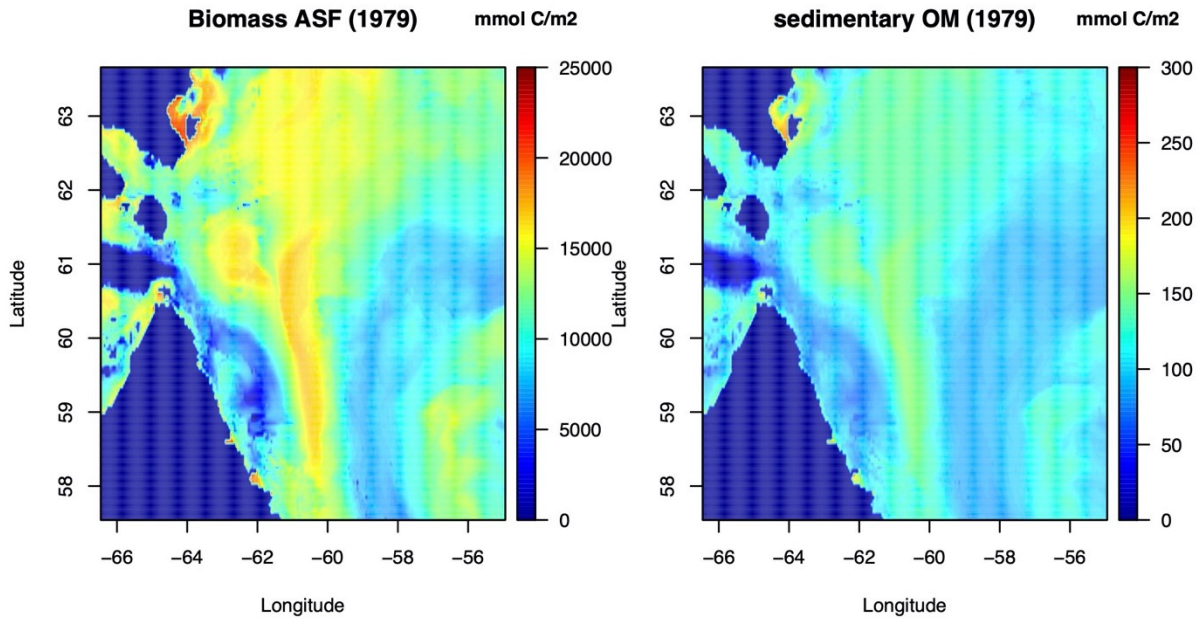

Figure 66: Initial biomass of ASF and sedimentary OM (output Step 2).

The final results of the coupled model for both 1979 (always left) and 1993 (always right) are shown below as median predicted suspended *sOM* concentration along the High (Figure 67) and Low (Figure 68) sponge transects, the *sOM* concentration in the bottom layer (Figure 69Figure 69), the biomass of ASF (Figure 70) and the predicted sediment community oxygen consumption (SCOC) (Figure 71), which represents degradation of OMsed and respiration by ASF.

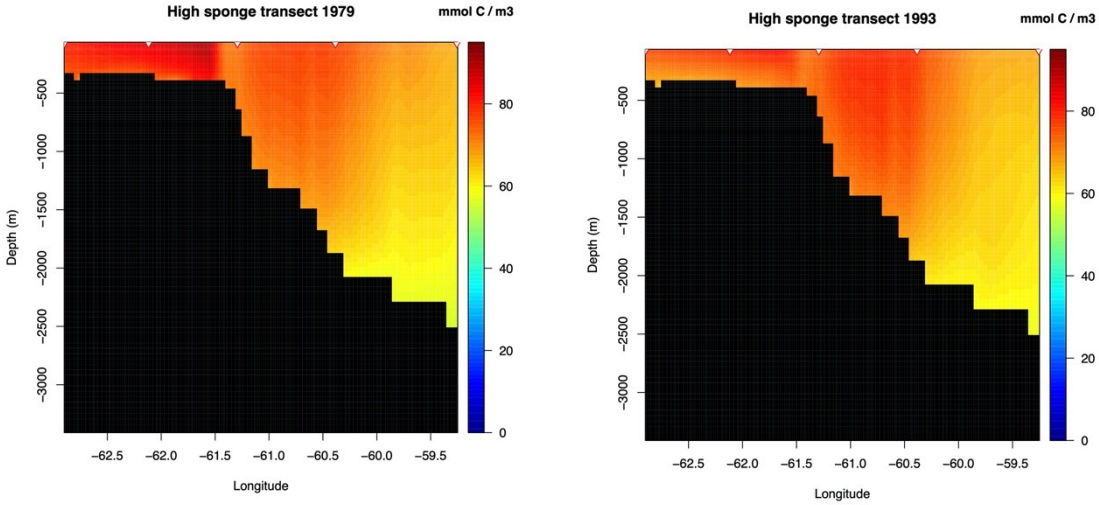

Figure 67: Output of suspended organic matter for 1979 (left) and 1993 (right) from the coupled model along the High sponge transect.

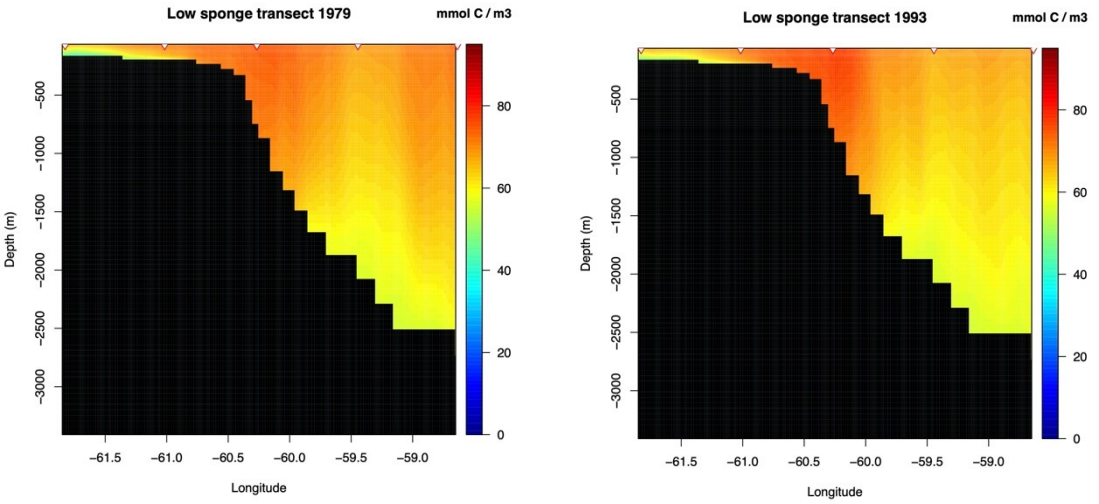

Figure 68: Output of suspended organic matter for 1979 (left) and 1993 (right) from the coupled model for the Low sponge transect.

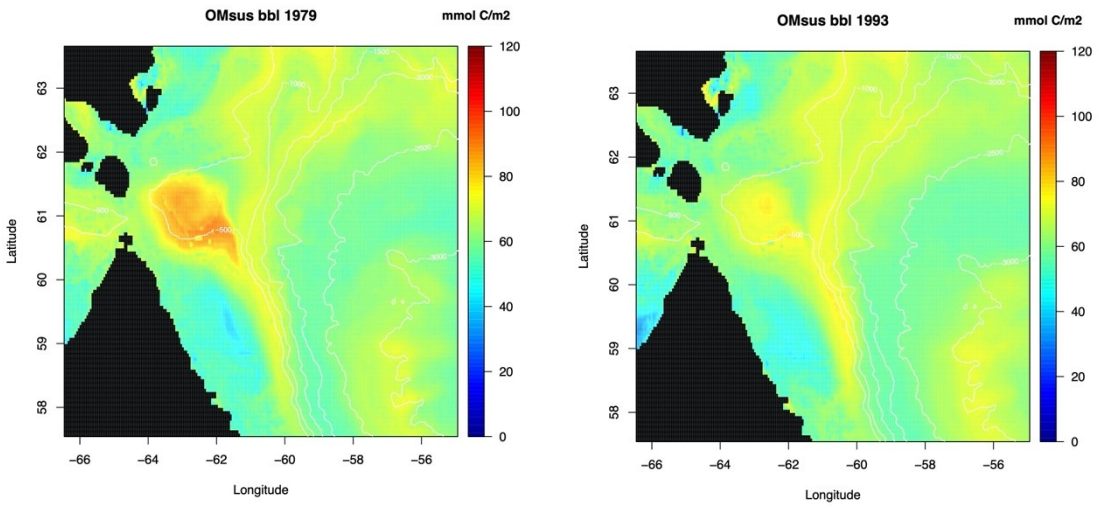

Figure 69: Output of the suspended organic matter concentration in the bottom layer for 1979 (left) and 1993 (right).

The High and Low sponge transects and OM in the bottom layer of the final coupled simulations (Step 3) are a bit different from the output of initial suspended OM concentration calculations (see above), with in particular a higher suspended OM concentration on the shelf. We think this is largely due to a slow accumulation of slow-degrading *sOM* in the depression in the centre left of the model domain (see also reduced current velocities in this depression in Figure 55 above), which is particularly prominent in the year 1979 and less so in 1993. This accumulation is possible because the model simulations were run under the assumption of a constant export flux throughout the whole year. This allowed us to focus on the differences in food availability and ASF biomass due to the hydrodynamics in the two AMOC states, but this assumption naturally strengthens this accumulation effect as there is no period with reduced *sOM* input and therefore we do not consider this a major artefact of the model, rather a consequence of the chosen approach.

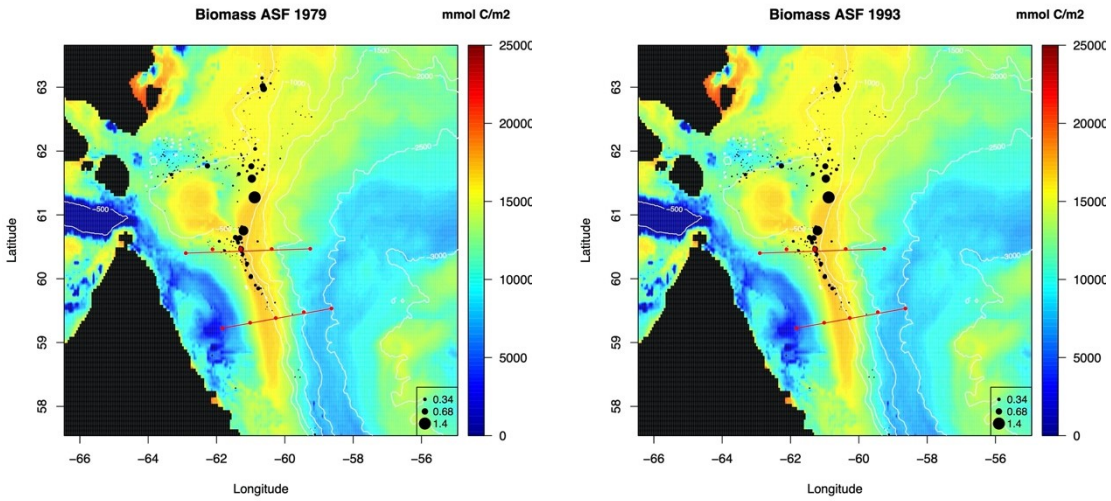

Figure 70: Coupled model predictions of the biomass of active suspension feeders (ASF) for 1979 (left) and 1993 (right). Superimposed are the published ICES sponge biomass data (see above) and the CTD transects, with central stations being the lander stations.

The most striking result is the ability of the coupled model to reproduce the biomass patterns of ASF at the Davis Strait case study. The biomass data are in kg WW/metre trawl, which are not easily converted into mmol C m^{-2}, yet the broad resemblance between the trawl data and model prediction is remarkable. The relatively rich sponge biomass region the north of the model domain (62-63N and -60 - -62E) corresponds well with the observations as well as the predicted lower sponge biomass in the region towards the Canadian coast (61.5-62.5N and -63E). The model further predicts reduced sponge biomass along the southern coast, and although no data are available for this region, our coupled model results are similar to those from the habitat suitability modelling efforts from Knudby *et al*. (2013) and Beazley *et al*. (2016). The predicted elevated biomass in the depression in the centre west of the model domain cannot be verified with observations, but as described above, these predictions may be an artefact of the (artificial) accumulation of suspended organic matter in this part of the model.

Most successful are the predictions of a zone of high sponge biomass along the shelf break. It is important to realise that these predictions are made without any pre-assumptions on sponge preference for depth or location, but are a mere result of the simulated suspended OM concentrations in the bottom layer from the hydrodynamic model coupled to a (comparatively simple) physiological model for the dominant active suspension feeder (the sponge *G. barretti*) in this region (Knudby *et al*. 2013). The model does however also predict elevated biomass further south than observations indicate. In fact, the Low sponge transect is predicted to have elevated ASF biomass, especially on the shelf. Measurements of the POC concentration in the water column that were made along the two transects within ATLAS (see Deliverable 2.3) in fact support the similarity in organic matter availability along the two transects. Additional field data from the landers, including fluorometry data and sediment trap data, will soon be evaluated to further compare food availability for the two transects. Yet, several explanations can be given for these conflicting results. One explanation for this is that the uptake by the extensive sponge grounds along the northern part of the shelf may deplete the bottom layer of suspended organic matter. This depletion may however not be accurately represented by the model simulations as the (VIKING20) model resolution increases towards greater depths such that organic matter depletion cannot be accurately included. Secondly, the southern region is known to be heavily trawled (E. Kenchington, pers com) and this may lower the observed sponge biomass below what can be sustained based

on food availability. Finally, the outflow of water from Hudson Strait (61°N) introduces relatively cold (i.e. sub-zero) and low salinity water onto the shelf, which may impose physiological constraints on the distribution of sponges that are not included in the coupled model.

We acknowledge here that the model-data agreement may also be partially the result of the assumed constant annual export flux to allow focussing on the differences in AMOC states. The positive agreement does call for additional (and lengthy) simulations to investigate the biomass development of ASF under temporal (i.e. seasonal) and spatial variable export fluxes. The model results clearly indicate that there is no difference in ASF biomass development between the two investigated AMOC states. This is congruent with the presented analysis of temperature, bottom velocity and vertical velocity data (see above), which already showed negligible differences between AMOC states.

At the same time, we show that the selected settings for suspended organic matter (i.e. *fOM* versus *sOM*) had a major effect on the ability to accurately predict the ASF biomass. Hence, it appears that (small) differences in hydrodynamics are not a major determinant of sponge biomass in this area. One has to bear in mind though, that the dominant hydrodynamic regime in the region, in particular the downward vertical velocity above the shelf break and the along-slope horizonal velocities, were hugely important to predict the spatial distribution of ASF biomass.

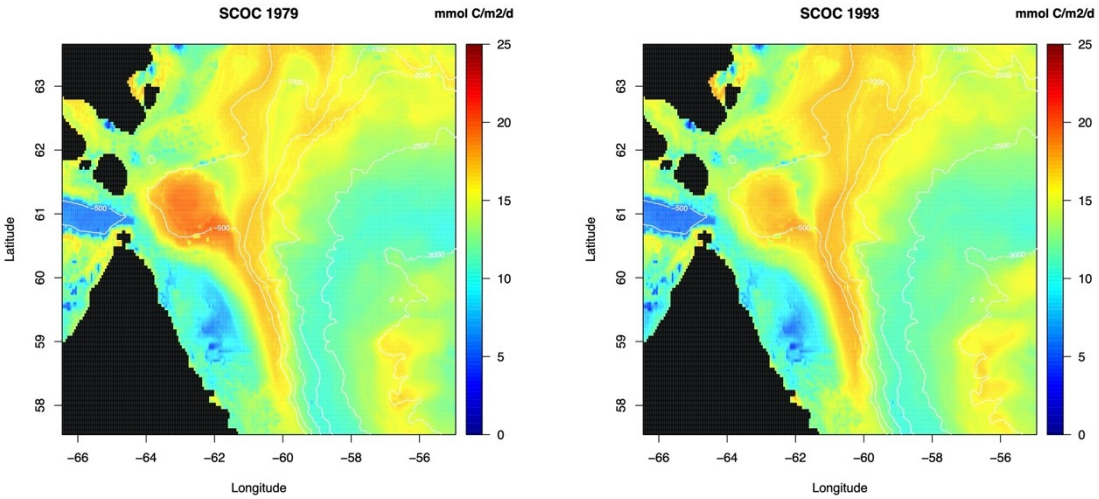

Figure 71: Predicted SCOC, i.e. sum of degradation of organic matter in the sediment and respiration by ASF, for 1979 (left) and 1993 (right).

Sediment respiration, expressed as sediment oxygen consumption using a 1:1 conversion of C units to O_2 (Glud 2008), follows largely the sponge distribution (Figure 71), which is sensible as sponges occur where the suspended organic matter concentration is highest and thereby the organic matter settling and the sponges themselves contribute to total respiration (Figure 72). A notable exception is the elevated respiration in the depression in the west centre of the model domain, where respiration is up to 20 mmol C m^{-2} d^{-1}. Few data on sediment respiration are available in the literature for this part of the ocean (Stratmann *et al*. In press). Link *et al*. (2013) performed benthic (i.e. without sponges) respiration measurements in the eastern North-West-Passage, the opening of Lancaster Sound and Baffin Bay, these sites are however substantially further north (>74°N) than the modelled region. They measured oxygen fluxes ranging from 2-8 mmol O2 m^{-2} d^{-1} for various sites, which is a factor of ±2 lower than modelled here. Grant *et al*. (1991) measured oxygen fluxes at a lower latitude (55°N) as the model region and at shallower (±120 m deep) coastal sites, which likely explains why the measured oxygen fluxes of 14-28 mmol O_2 m^{-2} d^{-1} are higher as compared to the model results. Sediment respiration is also lower than measured for the *G. baretti* sponge grounds on the Norwegian shelf (±50 mmol O_2 m^{-2} d^{-1}, (Cathalot *et al*. 2015)) and for *G. barretti* alone (15 mmol O_2 m^{-2} d^{-1}, Kutti *et al*. (2013)). Within ATLAS, we aim to get measurements from the study area from the oxygen sensors that were mounted on the two landers (see Deliverable 2.3) and from estimating sponge biovolume from video transects (obtained during the Amundsen cruises in 2018 and 2019) and subsequent conversion and upscaling to total respiration (ongoing work by J. Vad, Edinburgh University).

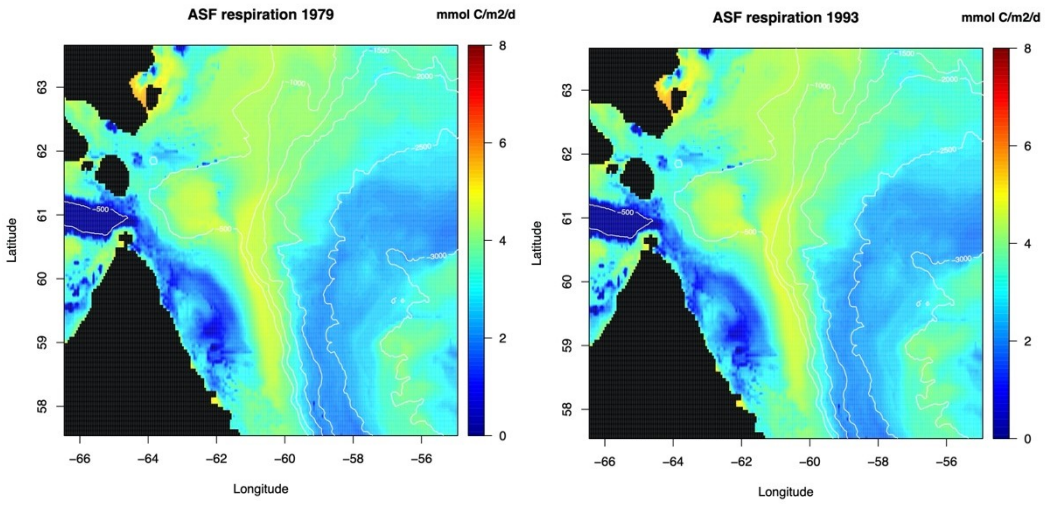

Figure 72: Respiration by the ASF in the model domain for 1979 (left) and 1993 (right)

Document Information

EU Project N°	678760	**Acronym**	ATLAS
Full Title	A trans-Atlantic assessment and deep-water ecosystem-based spatial management plan for Europe		
Project website	www.eu-atlas.org		

Deliverable	**N°**	2.5	**Title**	Integrative and coupled model based on hydrodynamics, biogeochemistry and physiology for the prediction of biomass and biogeochemical dynamics, projections under future oceanic conditions and marine spatial planning
Work Package	**N°**	2	**Title**	Functional Ecosystems

Date of delivery	**Contractual**		**Actual**	
Dissemination level	PU	PU Public, fully open, e.g. web		
		CO Confidential restricted under conditions set out in Model Grant Agreement		
		CI Classified, information as referred to in Commission Decision 2001/844/EC		

Authors (Partner)				
Responsible Authors	**Name**	Dick van Oevelen	**Email**	Dick.van.oevelen@nioz.nl
		Evert de Froe		Evert.de.Froe@nioz.nl

Version log			
Issue Date	**Revision N°**	**Author**	**Change**

7 References

Alldredge AL, Silver MW. 1988. Characteristics, dynamics and significance of marine snow. Progress in Oceanography 20:41-82.

Anderson TR, Hessen DO, Elser JJ, Urabe J. 2005. Metabolic stoichiometry and the fate of excess carbon and nutrients in consumers. American Naturalist 165:1-15.

Anthony KRN, 1999. Coral suspension feeding on fine particulate matter, Journal, pp. 85-106.

Anthony KRN, Connolly SR, Willis BL. 2002. Comparative analysis of energy allocation to tissue and skeletal growth in corals. Limnology and Oceanography 47:1417-1429.

Bashmachnikov I, Loureiro CM, Martins A. 2013. Topographically induced circulation patterns and mixing over Condor seamount. Deep Sea Research Part II: Topical Studies in Oceanography 98:38-51.

Beazley L, Kenchington E, Yashayaev I, Murillo FJ. 2015. Drivers of epibenthic megafaunal composition in the sponge grounds of the Sackville Spur, northwest Atlantic. Deep Sea Research Part I: Oceanographic Research Papers 98:102-114.

Beazley L, Murillo FJ, Kenchington E, Guijarro J, Lirette C, Siferd T, *et al*., 2016. Species Distribution Modelling of Corals and Sponges in the Eastern Arctic for Use in the Identification of Significant Benthic Areas. Canadian Technical Report of Fisheries and Aquatic Sciences 3175, Journal.

Böning CW, Behrens E, Biastoch A, Getzlaff K, Bamber JL. 2016. Emerging impact of Greenland meltwater on deepwater formation in the North Atlantic Ocean. Nature Geoscience 9:523.

Cathalot C, van Oevelen D, Cox T, Kutti T, Lavaleye M, duineveld G, *et al*. 2015. Cold-water coral reefs and adjacent sponge grounds: Hotspots of benthic respiration and organic carbon cycling in the deep sea. Frontiers in Marine Science 2:37.

Codiga DL, Eriksen CC. 1997. Observations of low-frequency circulation and amplified subinertial tidal currents at Cobb Seamount. Journal of Geophysical Research: Oceans 102:22993-23007.

Cyr F, van Haren H, Mienis F, Duineveld G, Bourgault D. 2016. On the influence of cold-water coral mound size on flow hydrodynamics, and vice versa. Geophysical Research Letters 43:775-783.

Davies AJ, Guinotte JM. 2011. Global habitat suitability for framework-forming cold-water corals. PLOS ONE 6:e18483.

de Froe E, Rovelli L, Glud RN, Maier SR, Duineveld G, Mienis F, *et al*. 2019. Benthic Oxygen and Nitrogen Exchange on a Cold-Water Coral Reef in the North-East Atlantic Ocean. Frontiers in Marine Science 6.

Doval MD, Álvarez-Salgado XA, Pérez FF. 2001. Organic matter distributions in the Eastern North Atlantic–Azores Front region. Journal of Marine Systems 30:33-49.

Duineveld GCA, Lavaleye MSS, Bergman MIN, De Stigter H, Mienis F. 2007. Trophic structure of a cold-water coral mound community (Rockall Bank, NE Atlantic) in relation to the near-bottom particle supply and current regime. Bulletin of Marine Science 81:449-467.

Giacomello E, Menezes GM, Bergstad OA. 2013. An integrated approach for studying seamounts: CONDOR observatory. Deep Sea Research Part II: Topical Studies in Oceanography 98:1-6.

Glud RN. 2008. Oxygen dynamics of marine sediments. Marine Biology Research 4:243-289.

Gori A, Grover R, Orejas C, Sikorski S, Ferrier-Pages C. 2014. Uptake of dissolved free amino acids by four cold-water coral species from the Mediterranean Sea. Deep-Sea Research Part II-Topical Studies in Oceanography 99:42-50.

Grant J, Emerson CW, Hargrave BT, Shortle JL. 1991. Benthic oxygen consumption on continental shelves off eastern Canada. Continental Shelf Research 11:1083-1097.

Grebmeier JM, Overland JE, Moore SE, Farley EV, Carmack EC, Cooper LW, *et al*. 2006. A major ecosystem shift in the northern Bering Sea. Science 311:1461-1464.

Guihen D, White M, Lundälv T. 2012. Temperature shocks and ecological implications at a cold-water coral reef. Marine Biodiversity Records 5:1-10.

Guinotte JM, Orr J, Cairns S, Freiwald A, Morgan L, George R. 2006. Will human-induced changes in seawater chemistry alter the distribution of deep-sea scleractinian corals? Frontiers in Ecology and the Environment 4:141-146.

Henson SA, Yool A, Sanders R. 2015. Variability in efficiency of particulate organic carbon export: A model study. Global Biogeochemical Cycles 29:33-45.

Hunter T, 1989. Suspension Feeding in Oscillating Flow: The Effect of Colony Morphology and Flow Regime on Plankton Capture by the Hydroid Obelia longissima, Journal, pp. 41-49.

Huskin I, Viesca L, Anadón R. 2004. Particle flux in the Subtropical Atlantic near the Azores: influence of mesozooplankton. Journal of Plankton Research 26:403-415.

Johnson C, Sherwin T, Smythe-Wright D, Shimmield T, Turrell W, 2010. Wyville Thomson Ridge Overflow Water: Spatial and temporal distribution in the Rockall Trough, Journal. Elsevier, pp. 1153-1162.

Kahn AS, Yahel G, Chu JWF, Tunnicliffe V, Leys SP. 2015. Benthic grazing and carbon sequestration by deep-water glass sponge reefs. Limnology and Oceanography 60:78-88.

Kenchington E, Lirette C, Cogswell A, Archambault D, Archambault P, Benoit H, *et al*., 2010. Delineating Coral and Sponge Concentrations in the Biogeographic Regions of the East Coast of Canada Using Spatial Analyses. Canadian Science Advisory Secretariat, Journal.

Kenyon NH, Akhmetzhanov AM, Wheeler AJ, van Weering TCE, de Haas H, Ivanov MK. 2003. Giant carbonate mud mounds in the southern Rockall Trough. Marine Geology 195:5-30.

Knudby A, Kenchington E, Murillo FJ. 2013. Modeling the Distribution of <italic>Geodia</italic> Sponges and Sponge Grounds in the Northwest Atlantic. PLOS ONE 8:e82306.

Koopmans M, Martens D, Wijffels RH. 2010. Growth Efficiency and Carbon Balance for the Sponge Haliclona oculata. Marine Biotechnology 12:340-349.

Kutti T, Bannister RJ, Fosså JH. 2013. Community structure and ecological function of deep-water sponge grounds in the Traenadypet MPA-Northern Norwegian continental shelf. Continental Shelf Research 69:21-30.

Larsson AI, Lundälv T, van Oevelen D. 2013. Skeletal growth, respiration rate and fatty acid composition in the cold-water coral Lophelia pertusa under varying food conditions. Marine Ecology Progress Series 483:169-184.

Leys SP, Kahn AS, Fang JKH, Kutti T, Bannister RJ. 2018. Phagocytosis of microbial symbionts balances the carbon and nitrogen budget for the deep-water boreal sponge Geodia barretti. Limnology and Oceanography 63:187-202.

Leys SP, Yahel G, Reidenbach MA, Tunnicliffe V, Shavit U, Reiswig HM. 2011. The sponge pump: the role of current induced flow in the design of the sponge body plan. Plos One 6.

Link H, Piepenburg D, Archambault P. 2013. Are Hotspots Always Hotspots? The Relationship between Diversity, Resource and Ecosystem Functions in the Arctic. Plos One 8:e74077.

Lozier MS, Li F, Bacon S, Bahr F, Bower AS, Cunningham SA, *et al*. 2019. A sea change in our view of overturning in the subpolar North Atlantic. Science 363:516-521.

Maier SR, Kutti T, Bannister RJ, van Breugel P, van Rijswijk P, van Oevelen D. 2019. Survival under conditions of variable food availability: Resource utilization and storage in the cold-water coral Lophelia pertusa. Limnology and Oceanography 64:1651-1671.

Marsay CM, Sanders RJ, Henson SA, Pabortsava K, Achterberg EP, Lampitt RS. 2015. Attenuation of sinking particulate organic carbon flux through the mesopelagic ocean. Proceedings of the National Academy of Sciences 112:1089-1094.

McDonnell AMP, Buesseler KO, 2010. Variability in the average sinking velocity of marine particles, Journal, pp. 2085-2096.

Mienis F, de Stigter HC, White M, Duineveld G, de Haas H, van Weering TCE. 2007. Hydrodynamic controls on cold-water coral growth and carbonate-mound development at the SW and SE Rockall Trough Margin, NE Atlantic Ocean. Deep-Sea Research Part I-Oceanographic Research Papers 54:1655-1674.

Mienis F, van der Land C, de Stigter HC, van de Vorstenbosch M, de Haas H, Richter T, *et al*. 2009. Sediment accumulation on a cold-water carbonate mound at the Southwest Rockall Trough margin. Marine Geology 265:40-50.

Mienis F, van Weering T, de Haas H, de Stigter H, Huvenne V, Wheeler A. 2006. Carbonate mound development at the SW Rockall Trough margin based on high resolution TOBI and seismic recording. Marine Geology 233:1-19.

Mohn C, Rengstorf A, White M, Duineveld G, Mienis F, Soetaert K, *et al*. 2014. Linking benthic hydrodynamics and cold-water coral occurrences: A high-resolution model study at three cold-water coral provinces in the NE Atlantic. Progress in Oceanography 122:92-104.

Orejas C, Gori A, Rad-Menéndez C, Last KS, Davies AJ, Beveridge CM, *et al*. 2016. The effect of flow speed and food size on the capture efficiency and feeding behaviour of the cold-water coral *Lophelia pertusa*. Journal of Experimental Marine Biology and Ecology 481:34-40.

Piepenburg D, Blackburn TH, Vondorrien CF, Gutt J, Hall POJ, Hulth S, *et al*. 1995. Partitioning of benthic community respiration in the Arctic (northwestern Barents Sea). Marine Ecology-Progress Series 118:199-213.

Purser A, Larsson AI, Thomsen L, van Oevelen D. 2010. The influence of flow velocity and food concentration on *Lophelia pertusa* (Scleractinia) zooplankton capture rates. Journal of Experimental Marine Biology and Ecology 395:55-62.

R Development Core Team, 2015. R: A language and environment for statistical computing, Journal. R Foundation for Statistical Computing, Vienna, Austria.

Rengstorf AM, Mohn C, Brown C, Wisz MS, Grehan AJ. 2014. Predicting the distribution of deep-sea vulnerable marine ecosystems using high-resolution data: Considerations and novel approaches. Deep Sea Research Part I: Oceanographic Research Papers 93:72-82.

Riley JS, Sanders R, Marsay C, Le Moigne FAC, Achterberg EP, Poulton AJ. 2012. The relative contribution of fast and slow sinking particles to ocean carbon export. Global Biogeochemical Cycles 26.

Roberts EM, Mienis F, Rapp HT, Hanz U, Meyer HK, Davies AJ. 2018. Oceanographic setting and short-timescale environmental variability at an Arctic seamount sponge ground. Deep Sea Research Part I: Oceanographic Research Papers 138:98-113.

Roberts JM, Wheeler A, Freiwald A, Cairns S, 2009. Cold-water corals. The biology and geology of deep-sea coral habitats. Cambridge University Press, Cambridge.

Santos M, Moita MT, Bashmachnikov I, Menezes GM, Carmo V, Loureiro CM, *et al*. 2013. Phytoplankton variability and oceanographic conditions at Condor seamount, Azores (NE Atlantic). Deep Sea Research Part II: Topical Studies in Oceanography 98:52-62.

Soetaert K, Mohn C, Rengstorf A, Grehan A, van Oevelen D. 2016. Ecosystem engineering creates a direct nutritional link between 600-m deep cold-water coral mounds and surface productivity. Scientific Reports 6:35057.

Soetaert K, Petzoldt T. 2010. Inverse modelling, sensitivity and Monte Carlo analysis in R using package FME. Journal of Statistical Software 33:1-28.

Stratmann T, Soetaert K, Wei C-L, Lin Y-S, Oevelen Dv. In press. The SCOC database, a large, open, and global database with sediment community oxygen consumption rates. Nature Scientific Data.

Tempera F, Giacomello E, Mitchell NC, Campos AS, Braga Henriques A, Bashmachnikov I, *et al*., 2012. 59 - Mapping Condor Seamount Seafloor Environment and Associated Biological Assemblages (Azores, NE Atlantic) in: Harris, P.T., Baker, E.K. (Eds.), Seafloor Geomorphology as Benthic Habitat. Elsevier, London, pp. 807-818.

Thomassen S, Riisgard HU. 1995. Growth and energetics of the sponge Halichondria panicea. Marine Ecology Progress Series 128:239-246.

Tian RC, Deibel D, Rivkin RB, Vézina AF. 2004. Biogenic carbon and nitrogen export in a deep-convection region: simulations in the Labrador Sea. Deep Sea Research Part I: Oceanographic Research Papers 51:413-437.

Tian RC, Vézina A, Legendre L, Ingram RG, Klein B, Packard T, *et al*. 2000. Effects of pelagic food-web interactions and nutrient remineralization on the biogeochemical cycling of carbon: a modeling approach. Deep Sea Research Part II: Topical Studies in Oceanography 47:637-662.

Tittensor DP, Baco AR, Hall-Spencer JM, Orr JC, Rogers AD. 2010. Seamounts as refugia from ocean acidification for cold-water stony corals. Marine Ecology-an Evolutionary Perspective 31:212-225.

Trull TW, Bray SG, Buesseler KO, Lamborg CH, Manganini S, Moy C, *et al*. 2008. In situ measurement of mesopelagic particle sinking rates and the control of carbon transfer to the ocean interior during the Vertical Flux in the Global Ocean (VERTIGO) voyages in the North Pacific. Deep Sea Research Part II: Topical Studies in Oceanography 55:1684-1695.

van Bleijswijk JDL, Whalen C, Duineveld GCA, Lavaleye MSS, Witte HJ, Mienis F. 2015. Microbial assemblages on a cold-water coral mound at the SE Rockall Bank (NE Atlantic): interactions with hydrography and topography. Biogeosciences 12:4483-4496.

van Oevelen D, Mueller CE, Lundälv T, Middelburg JJ. 2016. Food selectivity and processing by the cold-water coral *Lophelia pertusa*. Biogeosciences 13:5789-5798.

van Oevelen D, Mueller CE, Lundälv T, van Duyl FC, de Goeij JM, Middelburg JJ. 2018. Niche overlap between a cold-water coral and an associated sponge for isotopically-enriched particulate food sources. Plos One 13:e0194659.

Van Soest RWM, Lavaleye MSS. 2005. Diversity and abundance of sponges in bathyal coral reefs of Rockall Bank, NE Atlantic, from boxcore samples. Marine Biology Research 1:338-349.

van Weering TCE, de Haas H, de Stigter HC, Lykke-Andersen H, Kouvaev I. 2003. Structure and development of giant carbonate mounds at the SW and SE Rockall Trough margins, NE Atlantic Ocean. Marine Geology 198:67-81.

Vogel S. 1977. Current-induced flow through living sponges in nature. Proceedings of the National Academy of Sciences of the United States of America 74:2069-2071.

Westrich JT, Berner RA. 1984. The role of sedimentary organic matter in bacterial sulfate reduction: The *G* model tested. Limnology and Oceanography 29:236-249.

Wild C, Mayr C, Wehrmann L, Schöttner S, Naumann M, Hoffmann F, *et al*. 2008. Organic matter release by cold water corals and its implication for fauna-microbe interaction. Marine Ecology Progress Series 372:67-75.

Witte U, Brattegard T, Graf G, Springer B. 1997. Particle capture and deposition by deep-sea sponges from the Norwegian-Greenland Sea. Marine Ecology Progress Series 154:241-252.

Yesson C, Taylor ML, Tittensor DP, Davies AJ, Guinotte J, Baco A, *et al*. 2012. Global habitat suitability of cold-water octocorals. Journal of Biogeography 39:1278-1292.

Yool A, Popova EE, Anderson TR. 2011. Medusa-1.0: a new intermediate complexity plankton ecosystem model for the global domain. Geosci. Model Dev. 4:381-417.

Zamer WE. 1986. Physiological energetics of the intertidal sea anemone *Anthopleura elegantissima*. Marine Biology 92:299-314.